Frode Seland

Electrochemical Oxidation of Methanol and Formic Acid in Fuel Cell Processes

Doctoral thesis
for the degree of Philosophiae Doctor

Trondheim, 2005

Norwegian University of Science and Technology
Faculty of Natural Sciences and Technology
Department of Materials Science and Engineering

NTNU
Innovation and Creativity

IMT-Report 2005:78

NTNU
Norwegian University of Science and Technology
Doctoral thesis
for the degree of Philosophiae Doctor
Faculty of Natural Sciences and Technology
Department of Materials Science and Engineering

ISBN 82-471-7305-0 (printed ver.)
ISBN 82-471-7304-2 (electronic ver.)
ISSN 1503-8181

Doctoral theses at NTNU, 2005:204

Printed by NTNU-trykk

Acknowledgements

First of all I would like to thank my supervisors during my PhD work, Professor Reidar Tunold at NTNU and Professor David A. Harrington at UVic for inspiration, motivation and guidance throughout my PhD study. Special thanks to Professor Harrington who willingly took the responsibility of co-supervising my PhD work, and who gave me the opportunity to spend nine months in his laboratories during this thesis work. I also acknowledge Dr. Børre Børresen who was my academic advisor after Professor Tunold's retirement, and Professor Kemal Nisancioglu who has been my academic advisor since September 2005.

I wish to express my gratitude to all the people at the Electrochemistry group who have made my PhD journey a joyful one, especially Martha Bjerknes and Kjell Røkke for taking care of administrative and practical concerns, Magnus Thomassen for enduring four long years in the same office with me, Espen Sandnes for showing that there are more things to life than work and family, Sten-Egil Johnsen for all the fun on other planets, Randi Brateng for performing experiments of interest to me, Torsten Berning and Ole Edvard Kongstein for a great time in the EU projects, Gaute Svenningsen for performing the SEM scans in this thesis, and Rune Halseid for his genuine interest in science and for proofreading parts of my thesis. The people in Professor Harrington's group, especially Craig Jeffrey and Miguel Labayen, are acknowledged for fruitful discussions, experimental guidance and for making my time at UVic enjoyable.

Furthermore, I would like to thank all the people I have made friends with during my stay in Trondheim. It wouldn't have been the same without you.

This work was carried out at the Department of Materials Science and Engineering, Norwegian University of Science and Technology, and at the Chemistry Department, University of Victoria in the period December 2000 to October 2005. The Norwegian Research Council is gratefully acknowledged for the award of a scholarship within the program "Energi for framtiden". Financial support from an EU project in the 5th framework during my work with fuel cells is also acknowledged.

Finally I would like to thank my family for all the support and encouragement that they have given me during my PhD study. Special thanks to my wife Gry, for always being supportive and for motivating me to complete this work, and to my son Inge for just giving me his approval by calling me "pappa" every

morning before I left for work, hoping that I would come with him to the playground.

Summary

The main objectives of the thesis work were: (1), to study the oxidation of methanol and formic acid on platinum electrodes by employing conventional and advanced electrochemical methods, and (2), to develop membrane electrode assemblies based on polybenzimidazole membranes that can be used in fuel cells up to 200 °C.

D.c. voltammetry and a.c. voltammetry studies of methanol and formic acid on polycrystalline platinum in sulphuric acid electrolyte were performed to determine the mechanism and kinetics of the oxidation reactions.

A combined potential step and fast cyclic voltammetry experiment was employed to investigate the time dependence primarily of methanol oxidation on platinum. Charge measurements clearly demonstrated the existence of a parallel path at low potentials and short times without formation of adsorbed CO. Furthermore, experimental results showed that only the serial path, via adsorbed CO, exists during continuous cycling, with the first step being diffusion controlled dissociative adsorption of methanol directly from the bulk electrolyte. The saturation charge of adsorbed CO derived from methanol was found to be significantly lower than CO derived from formic acid or dissolved CO. This was attributed to the site requirements of the dehydrogenation steps, and possibly different compositions of linear, bridged or multiply bonded CO. The coverage of adsorbed CO from formic acid decreased significantly at potentials just outside of the hydrogen region (0.35 V vs. RHE), while it did not start to decrease significantly until about 0.6 V vs. RHE for methanol. Adsorbed CO from dissolved CO rapidly oxidized at potentials above about 0.75 V due to formation of platinum oxide.

Data from a.c. voltammograms from 0.5 Hz up to 30 kHz were assembled into electrochemical impedance spectra (EIS) and analyzed using equivalent circuits. The main advantages of collecting EIS spectra from a.c. voltammetry experiments are the ability to directly correlate the impedance spectra with features in the corresponding d.c. voltammograms, and the ability to investigate conditions with partially covered surfaces that are inaccessible in steady-state measurements.

A variety of spectral types were observed, and for methanol these showed only a single adsorption relaxation aside from the double-layer/charge-transfer relaxation, though some structure in the phase of the latter relaxation hints at

another process. The charge-transfer resistance showed Tafel behaviour for potentials in the rising part of the oxidation peak consistent with a one-electron process in the rate-determining step. The rate limiting step was proposed to be the electrochemical reaction between adsorbed CO and OH at the edge of islands of OH, with competition between OH and CO adsorption for the released reaction sites. Only a single adsorption relaxation in methanol oxidation was observed, implying that only one single coverage is required to describe the state of the surface and the kinetics. It was assumed that this single coverage is that of OH, and all the surface not covered with OH is covered with CO so that the coverage of CO is not an independent variable. Inductive behaviour and negative relaxation times in the methanol oxidation were attributed to nucleation and growth behaviour. Linear voltammetry reversal and sweep-hold experiments also indicated nucleation-growth-collision behaviour in distinct potential regions, both in the forward and reverse potential scan for methanol oxidation on platinum.

In both methanol oxidation and formic acid oxidation, a negative differential resistance (NDR) was observed in the potential regions that possess a negative d.c. polarization slope, and was attributed to the formation of surface oxide which inhibited the oxidation of methanol or formic acid.

EIS spectra for formic acid clearly showed the presence of an additional low frequency relaxation at potentials where we expect adsorbed dissociated water or platinum oxide to be present, implying that more than one single coverage is required to describe the state of the surface and the kinetics. Two potential regions with hidden negative differential resistance (HNDR) behaviour were identified in the positive-going sweep, one prior to platinum oxide formation, assumed to involve adsorbed dissociated water, and one just negative of the main oxidation peak, assumed to involve platinum oxide. Oscillatory behaviour was found in the formic acid oxidation on platinum by adding a large external resistance to the working electrode circuit, which means that there is no longer true potentiostatic control at the interface. By revealing the system time constants, impedance measurements can be used to assist in explaining the origin of the oscillations. In the case of formic acid, these measurements showed that the oscillations do not arise from the chemical mechanism alone, but that the potential plays an essential role.

Preparation and optimization of gas-diffusion electrodes for high temperature polymer electrolyte fuel cells based on phosphoric acid doped polybenzimidazole (PBI) membranes was performed. This fuel cell allows for operating temperatures up to 200 °C with increased tolerance towards catalytic

poisons, typical carbon monoxide. In this work we employed pure hydrogen and oxygen as the fuel cell feeds, and determined the optimum morphology of the support layer, and subsequently optimized the catalytic layer with respect to platinum content in the Pt/C catalyst and PBI loading. A smooth and compact support layer with small crevices and large islands was found to be beneficial with our spraying technique in respect to adhesion to the carbon backing and to the catalyst layer. We found that a high platinum content catalyst gave a significantly thinner catalyst layer (decreased porosity) on both anode and cathode with superior performance. The PBI loading was found to be crucial for the performance of the electrodes, and a relatively high loading gave the best performing electrodes.

Table of Contents

Nomenclature

Roman letters

A_j	Elementary matrix for reaction step *j*	mol m^{-2} s^{-1}
a	Number of parameters added	1
B	Fitting parameter (inverse inductance)	H^{-1} m^{-2}
C	Capacitance	F m^{-2}
E	Potential	V
F	Faraday's constant	C mol^{-1}
F	F-test value	1
f	frequency	s^{-1}
J_j	Jacobian matrix for reaction step *j*	mol m^{-2} s^{-1}
j	Current density	A m^{-2}
K	Island growth rate	m s^{-1}
k_i	Rate constant with respect to *i*	mol m^{-1} s^{-1}
L	Inductance	H m^2
m	Surface Pt atoms occupied by one CO species	1
N	Number of frequencies	1
N_{eps}	Number of electrons per site (surface)	1
n	Number electrons involved in the rate limiting step	1
n	Number of parameters in the new circuit	1
n	Surface Pt atoms occupied by one OH or O species	1
p	Total island perimeter	m
Q	Capacitive element (CPE)	S m^{-2} s^{α}
q	Charge density	C m^{-2}
R	Universal gas constant	J mol^{-1} K^{-1}
R	Resistance	Ω m^2
r_i	Net reaction rate with respect to *i*	mol m^{-2} s^{-1}
s	Laplace transform parameter	s^{-1}
T	Temperature	K

t	time	S
v_A	Reaction rate of step A	mol m^{-2} s^{-1}
Y	Admittance	S m^{-2}
Z	Impedance	Ω m^2

Greek letters

α	CPE exponent with value between 0 and 1	1
α	Transfer coefficient	1
χ^2	Chi squared	1
ϕ	Inner electric potential (Galvani potential)	V
Γ_m	Surface concentration of a monolayer	mol m^{-2}
η	Over potential	V
ν	Sweep rate	V s^{-1}
θ_i	Surface coverage of species i	1
τ	time constant	s
ω	Angular frequency	rad s^{-1}

Acronyms

a.c.	Alternating current
ads	Adsorbed
CPE	Constant phase element
d.c.	Direct current
DMAc	Dimethylacetamide
DMFC	Direct methanol fuel cell
DEMS	Differential electrochemical mass spectrometry
EIS	Electrochemical impedance spectroscopy
EMIRS	Electrochemically modulated infrared reflectance spectroscopy
EQCM	Electrochemical quartz crystal microbalance
FFT	Fast Fourier transform

FTIR	Fourier transform infra-red
HNDR	Hidden negative differential resistance
IR	Infra-Red
IR	Ohmic potential loss
LH	Langmuir-Hinshelwood
LIA	Lock-in amplifier
MEA	Membrane electrode assembly
NDR	Negative differential resistance
NGC	Nucleation-growth-collision
NHE	Normal hydrogen electrode
n/a	Not available
OCV	Open circuit voltage
PBI	Polybenzimidazole
PEM	Proton exchange / Polymer electrolyte membrane
PTFE	Polytetrafluorethylene
RDE	Rotating disk electrode
rds	Rate determining step
RHE	Reversible hydrogen electrode
rms	Root mean square
SEM	Scanning electron microscopy
STM	Scanning tunnelling microscopy
UPD	Under-potential deposition

Chapter 1

Introduction

1.1 Background

Energy systems of the future will involve direct use of solar energy, production and storage of energy carriers like hydrogen, and utilization of advanced systems of energy conversion in a much more environmental friendly way, as compared to the extended usage of fossil fuels today. Hydrogen is forecast by many to be the ultimate energy carrier in the future. This is mainly because it is renewable and virtually non-polluting compared to other energy carriers like gasoline and diesel. Hydrogen is from an environmental viewpoint the ideal energy carrier. It can be transformed into heat and mechanical energy by combustion, and to electrical energy in fuel cells with pure water as the only product. The CO_2 balance for the entire energy process is in this case dependent on the fuel or the type of primary energy used to produce hydrogen. Hydrogen can be produced from a variety of renewable energy sources, including electrolytic hydrogen produced from wind or photovoltaic sources, and biomass-derived hydrogen by gasification. However, the low volumetric energy density of hydrogen makes on-board storage difficult, and the lack of a gaseous fuel infrastructure complicates the process of introducing hydrogen as a fuel. Thus, making use of liquid hydrogen carriers instead of pure hydrogen could present solutions to these difficulties.

Present production of hydrogen carriers uses fossil fuels and natural gas in particular, although hydrogen carriers can be produced from biomass (biofuels), which can be produced and consumed without altering the CO_2 balance [1,2]. Renewable biofuels include a whole range of biotechnology-derived fuels, including liquid hydrogen carriers like methanol, ethanol, formic acid and ammonia. Liquid hydrogen carriers can be introduced and stored much more easily than hydrogen gas, and can even to some extent utilize the existing infrastructure. In the short term, methanol is emerging as the fuel of choice for fuel cell vehicle applications. However, the main drawback with any hydrogen carrier is the cost, both economical and energetic, of synthesizing it from either fossil fuels or renewable energy sources and then subsequently splitting or reforming it to hydrogen.

The biofuels, like hydrogen, are also capable of delivering power directly in a polymer electrolyte membrane fuel cell without the need for reforming. The use of methanol directly in fuel cells was first seriously investigated in the 1960ies after the invention of the proton conducting membrane. This direct methanol fuel cell (DMFC) clearly simplifies hardware and response characteristics and has enormous potential for mobile applications. However, the direct methanol fuel cell has gained most attention recently for use in portable electronics as a substitute for batteries with a long charging time. Although fuel cells must be markedly improved before they can widely replace internal combustion engines in motor vehicles, their significantly improved emissions characteristics and high efficiency make them very desirable.

1.2 Motivation for the Thesis

Organic compounds, such as methanol and formic acid, have the simplest structure of all the possible organic fuels and so should also have the most straightforward reaction mechanisms. However, low exchange current densities on most electrodes make them far less active than hydrogen, and a precious metal catalyst like platinum is needed to obtain reasonable reaction rates. Unfortunately, the platinum catalyst is easily poisoned by intermediates from the oxidation of the organic fuels, thus significantly limiting the performance. This limitation has slowed down the development of direct organic fuel cells.

Numerous publications exist in the literature with the intention of establishing the reaction mechanism and kinetics of the oxidation of simple organic molecules on platinum electrodes. Although much progress has been made, there are still some important remaining issues in the kinetics and mechanism of these reactions. There is a general consensus that adsorbed carbon monoxide is produced in the oxidation process and that it acts as a catalyst poison. The oxidation of formic acid is known to exhibit a dual path mechanism [3-6], where the direct oxidation to carbon dioxide occurs without formation of poisoning species. The indirect path happens through formation of adsorbed CO, which blocks the direct path and limits the performance of the catalyst. Strong evidence has been put forth that the oxidation of methanol can happen through different pathways: a serial pathway where this poisoning species is an intermediate in the oxidation, and parallel pathways where methanol is oxidized via short-lived intermediates to a stable oxidation product. The parallel pathway has been the subject of several studies [7-13], and the stable oxidation products are in general found to be carbon dioxide, formic acid and formaldehyde.

The question about whether oxidation of adsorbed CO occurs via a nucleation-growth-collision (NGC) (reaction on the edges of OH islands) or a Langmuir-Hinshelwood (LH) (reaction occurring randomly on the surface) mechanism is a current issue in methanol oxidation kinetics [14]. An interesting aspect of both formic acid and methanol oxidation is that they exhibit both potential and current oscillations in certain potential regions due to the formation of an oxygen containing species at the catalyst surface along with the poison [15-18]. Mechanistic and kinetic considerations are important in order to be able to determine aspects that can lead to catalysts with enhanced activity and selectivity towards methanol and formic acid oxidation.

The poisoning effect of partially oxidized fragments like CO from methanol or formic acid oxidation on noble metal electrodes is significantly reduced if the operating temperature is increased above 100 °C (e.g. [19]). Recently, several alternative types of polymer electrolyte membranes for fuel cells have emerged, which do not require the same water balance as Nafion®, and have significantly lower permeability towards reactants. Functionalized polybenzimidazole derivatives have been identified as promising in this regard; they use phosphoric acid both as an electrolyte within the three-dimensional electrode structure and within the polymer itself [20,21]. Sufficient conductivity can be obtained at temperatures above about 150 °C giving rise to reasonable power densities. Furthermore, as the temperature can be increased up to 200 °C, the reaction kinetics are substantially increased and any eventual poisoning effect of the catalyst is minimized, making these new fuel cells very attractive.

1.3 Problem Statement

The main objectives of the thesis work were: (1), to study the oxidation of methanol and formic acid on platinum electrodes by employing conventional and advanced electrochemical methods, and (2), to develop membrane electrode assemblies based on polybenzimidazole membranes that can be used in fuel cells up to 200 °C.

The methanol oxidation and formic acid oxidation on noble metals are well studied due to their promise as fuel cell feeds. Although much work has been done, there still exist issues that are controversial: the nature of the parallel path, the role of nucleation-growth-collision behaviour and the oscillatory behaviour. It must be stressed that if a catalyst exists that promotes the parallel pathway without forming any poisoning or blocking species it would lead to a breakthrough not only in the development of direct organic fuel cells, but most

likely also in hydrogen - oxygen fuel cells where the hydrogen contains carbonaceous fragments from the reformer reactions.

Most previous PEM fuel cell work has been focused on the use of a Nafion® membrane, which has several limitations such as poor water management, low temperature, high permeability of reactants and low tolerance towards CO. Preparation and optimization of gas diffusion electrodes for high-temperature polymer fuel cells based on phosphoric acid doped polybenzimidazole membranes may boost renewed interest into developing direct organic fuel cells.

1.4 Methodology

Single-cell testing of fuel cells was employed to optimize the electrodes used in high temperature PEM fuel cells based on phosphoric acid doped PBI membranes. Several parameters had to be controlled in order to get reproducible and reliable results, such as gas flow, temperature and the manufacturing process of the MEAs. Thus in this work, fuel cell measurements have been used to optimize the catalytic layer properties, and also the necessity of a dense support layer was investigated.

Investigations of fundamental electrode kinetics are difficult on nanostructured electrocatalysts because the complex geometric structure of these particles makes it difficult to control the reactant, current and potential distribution at the active surface. For that reason, the oxidation of methanol and formic acid were performed on smooth polycrystalline platinum electrodes in aqueous acid electrolyte.

The impedance method potentially can detect subtle changes in mechanism, and so its application in different potential regions around the voltammogram is expected to give new insight into the rate-limiting processes, and the basis for the oscillations. This thesis therefore makes extensive use of impedance, and supplements these results with other electrochemical methods. We employed the a.c. voltammetry technique, where a sinusoidal potential wave with a very small amplitude was superimposed onto a d.c. potential ramp, to collect the a.c. impedance data "on the fly", one frequency per potential cycle. This way we were able to collect dynamic impedance spectra for all potentials, in both positive- and negative-going potential scans. This allowed for investigation of conditions with partially covered surfaces that are inaccessible in steady-state measurements. Using a.c. impedance in the ordinary way, by waiting for steady

state to be established, is not useful when studying processes that are susceptible to oscillate or are dependent on island sizes and growth.

1.5 Outline of Thesis

This thesis is organized as a collection of individual chapters and includes four scientific papers intended for publication in peer reviewed journals. Chapter one is the introduction to the thesis, which gives the motivation for the project as well as project statement and methodology. Chapters two, three, four and five are the scientific papers. This format unavoidably leads to some repetition of background information, especially in the experimental sections. The conclusions are given in chapter six in abbreviated point form together with proposals for future work

Chapter two, *Methanol Oxidation Kinetics on Polycrystalline Platinum*, is intended for publication in Journal of Electroanalytical Chemistry, eventually after revising, and deals with the kinetics and mechanism of methanol oxidation on platinum by application of a combined potential step-cycle sequence, and fast cyclic voltammetry.

Chapter three and four, *Impedance Study of Methanol Oxidation on Platinum Electrodes* and *Impedance Study of Formic Acid Oxidation on Platinum Electrodes* make extensive use of the a.c. voltammetry technique (dynamic impedance) and supplement it with conventional electrochemical methods in order to investigate aspects of the methanol oxidation (chapter three) and formic acid oxidation (chapter four) on polycrystalline platinum electrodes. Chapter three is accepted for publication in Electrochimica Acta, and chapter four will be submitted to the Journal of Electroanalytical Chemistry after revising.

After fundamental investigation of the kinetics and mechanism of potential fuel cell feeds, chapter five, *Improving the Performance of High-Temperature PEM Fuel Cells based on PBI Electrolyte*, includes an initial study of a high-temperature polymer electrolyte fuel cell based on the phosphoric acid doped polybenzimidazole membrane. This work was done as part of the EU project in the 5^{th} framework program: "Advanced Methanol Fuel Cells for Vehicle Propulsion (AMFC)". The project was based on internal reforming of methanol and the use of polybenzimidazole as the polymer electrolyte membrane. The primary focus was on developing high-quality electrodes for hydrogen–oxygen fuel cells based on platinum catalysts. This chapter is submitted to Journal of Power Sources.

References

[1] J. Twidell, T. Weir, *Renewable Energy Resources*, E & FN SPON, London, 1998

[2] N. Kosaric, J. Velikonja, *FEMS Microbiology Reviews* **16** (1995) 111

[3] A. Capon, R. Parsons, *J. Electroanal. Chem.*, **45** (1973) 205

[4] T.D. Jarvi, E.M. Stuve, in: *Electrocatalysis*, J. Lipkowski, P.N. Ross (Eds.), Wiley-VCH, New York, 1998, pp. 75-154

[5] S.-G. Sun, in: *Electrocatalysis*, J. Lipkowski, P.N. Ross (Eds.), Wiley-VCH, New York, 1998, pp. 243-291

[6] J.M. Feliu, E. Herrero, in: *Handbook of Fuel Cells - Fundamentals, Technology and Applications*, W. Vielstich, H.A. Gasteiger, A. Lamm (Eds.), *Vol 2 Electrocatalysis*, John Wiley & Sons, Chichester, 2003, pp. 625-634

[7] X.H. Xia, T. Iwasita, F. Ge, W. Vielstich, *Electrochim. Acta*, **41** (1996) 711

[8] Sriramulu, S., Jarvi, T. D., Stuve, E. M., *Electrochim. Acta*, **44** (1998) 1127

[9] Sriramulu, S., Jarvi, T. D., Stuve, E. M., *J. Electroanal. Chem.*, **467** (1999) 132

[10] E.A. Batista, H. Hoster, T. Iwasita, *J. Electroanal. Chem.*, **554-555** (2003) 265

[11] G.A. Planes, J.L. Rodriguez, E. Pastor, C. Barbero, *Langmuir*, **19** (2003) 8137

[12] E.A. Batista, G.R.P. Malpass, A.J. Motheo, T. Iwasita, *J. Electroanal. Chem.*, **571** (2004) 273

[13] D. Cao, G.Q. Lu, A. Wieckowski, S.A. Wasileski, M. Neurock, *J. Phys. Chem. B*, **109** (2005) 11622

[14] J. Jiang, A. Kucernak, *J. Electroanal. Chem.*, **533** (2002) 153

[15] F. Raspel, R.J. Nichols, D.M. Kolb, *J. Electroanal. Chem.*, **286** (1990) 279

[16] M. Krausa, W. Vielstich, *J. Electroanal. Chem.*, **399** (1995) 7

[17] P. Strasser, M. Lübke, F. Raspel, M. Eiswirth, G. Ertl, *J. Chem. Phys.*, **107** (1997) 979

[18] J. Lee, C. Eickes, M. Eisworth, G. Ertl, *Electrochim. Acta*, **47** (2002) 2297

[19] Q. Li, R. He, J.-A. Gao, J.O. Jensen, N.J. Bjerrum, *J. Electrochem. Soc.*, **150** (2003) A1599

[20] J.S. Wainright, J.-T. Wang, D. Weng, R.F. Savinell, M. Litt, *J. Electrochem. Soc.*, **142** (1995) L121

[21] Y.-L. Ma, J.S. Wainright, M.H. Litt, R.F. Savinell, *J. Electrochem. Soc.*, **151** (2004) A8

Chapter 2

Methanol Oxidation Kinetics on Polycrystalline Platinum

Frode Seland [a], David A. Harrington [b] and Reidar Tunold [a]

[a] *Electrochemistry Group, Department of Materials Science and Engineering, Norwegian University of Science and Technology, NO-7491, Trondheim, Norway.*

[b] *Department of Chemistry, University of Victoria, Victoria, British Columbia, V8W 3V6, Canada.*

Abstract

The existence of parallel pathways in methanol oxidation at Pt electrodes is investigated by fast cyclic voltammetry and a combined chronoamperometry and cyclic voltammetry pulse-sweep technique. Charge calculations showed only formation of adsorbed CO and consequent stripping during continuous cycling, thus demonstrating the existence of a series path only. The first step in the methanol oxidation is diffusion controlled dissociative adsorption of methanol directly from bulk electrolyte. However, experimental evidence was found for the existence of a parallel pathway through short-lived intermediates, occurring independently of surface CO production, at short reaction times and low potentials in the first voltammetry sweep on polycrystalline platinum in sulphuric acid.

Keywords: Methanol, Platinum, CO, Cyclic Voltammetry, Parallel Path

2.1 Introduction

In recent years a great amount of experimental material has been accumulated dealing with chemisorption and electrochemical decomposition of various organic compounds on platinum group metals. The electrocatalytic oxidation of small organic molecules like methanol and formic acid at Pt electrodes has received considerable attention due to their promise as fuels in fuel cells. By far the most attention has been given to the methanol system, either as pure fundamental studies or studies related to the direct methanol fuel cell. Several reviews are available, e.g. [1-10]. Formic acid is another potential fuel for fuel cells, and has received considerable attention over the years and been reviewed several times, e.g. [3,4,9-11].

Methanol oxidation is suggested to proceed via several possible intermediates and pathways. Water is required for the overall conversion of methanol to carbon dioxide, which can be written as:

$$CH_3OH + H_2O \rightarrow CO_2 + 6H^+ + 6e^- \quad (1)$$

In the early seventies Bagotzky et al. [12] proposed a general mechanistic scheme including all possible intermediates from methanol to CO_2. Up to eight intermediates were suggested, of which CO, formic acid and formaldehyde are the most interesting ones. In addition, Lopes et al. [13] found indications of a methoxy species in electrochemical systems that could further complicate the mechanistic scheme of methanol oxidation on platinum.

Undoubtedly, the oxidation of methanol on platinum surfaces starts with dehydrogenation of the methanol molecule as shown by differential electrochemical mass spectrometry (DEMS) [14]. The first dehydrogenation step, reaction (2), was shown to be the rate determining step on the Pt(111) and Pt(110) surfaces through measurements of the kinetic isotope effect and the Tafel slope of the reaction [15,16]. The rate determining step on the Pt(100) surface was shown to be the second dehydrogenation reaction, equation (3). The effect of surface structure on the electrocatalytic properties towards methanol oxidation has been demonstrated several times, e.g. [16-19]. For simplicity, we assume that one adsorbed molecule binds to only one surface platinum atom in the following simplified reaction scheme. According to Munk et al. [20], the complete stripping of all three methyl hydrogen atoms at lower potentials must occur on the flat terrace areas of the electrode surface, due to the fact that at least four adjacent adsorption sites are needed. Furthermore, successive dehydrogenation eventually leads to formation of adsorbed carbon monoxide:

$$Pt-CH_3OH + Pt(site) \rightarrow Pt-CH_2OH + Pt-H \quad (2)$$

$$Pt-CH_2OH + Pt(site) \rightarrow Pt-CHOH + Pt-H \quad (3)$$

$$Pt-CHOH + Pt(site) \rightarrow Pt-COH + Pt-H \quad (4)$$

$$Pt-COH + Pt(site) \rightarrow Pt-CO + Pt-H \quad (5)$$

The dehydrogenation reactions lead to formation of adsorbed hydrogen atoms, which in turn will be followed by a one-electron transfer reaction to form a proton and an electron:

$$Pt-H \rightarrow Pt(site) + H^+ + e^- \quad (6)$$

The aim of the pioneering in-situ infrared spectroscopy studies in the early 1980s was to identify the product of dissociative adsorption of small organic molecules. It is now well known that the dissociative adsorption of many small organic molecules leads to large coverages of CO which can be linear, bridged or multiply bonded to the surface. A comprehensive review of the oxidation of small organic molecules as studied by in-situ infrared spectroscopy is given by Shi-Gang Sun [21]. Although many intermediates are detected by various methods, the exact structure of the adsorbed intermediates is unknown except for the adsorbed carbon monoxide molecule [6].

The tendency of both formic acid and methanol reactions to self-poisoning makes clear that catalyst properties must be changed to avert the poisoning condition. Equation (1) demonstrates the necessity of an oxygen donating source at the surface to complete the oxidation of methanol to CO_2. Since Pt oxide does not form below 0.75 V it has been suggested that the oxygen donor is dissociated water (equation (7)), or some form of activated water or oxide. Shimazu and Kita, [22], used an electrochemical quartz crystal microbalance, EQCM, to detect mass changes in a cyclic voltammogram on a platinum electrode. Quantitative analysis of the mass change revealed that the mass increase in the hydrogen and double-layer region, i.e. at lower potentials, during a positive-going potential scan was due to water adsorption on the platinum surface. Iwasita and Xia [23] found by Fourier transform infrared (FTIR) reflection-absorption spectroscopy at Pt(111) in perchloric acid that formation of adsorbed hydroxyl ions from water dissociation commence at about 0.5 V. Conway and co-workers [24,25] found that the oxidation of platinum surface is initiated by a process of reversible electrosorption of hydroxyl species commencing at about 0.75 V vs. RHE. However, Van der Geest et al. [26] argued against the formation of adsorbed OH species in the initial stages of Pt oxide and suggested it to be oxygen rather than OH. This was also recently suggested in an EQCM study [27]. Li et al. [28] assumed that the platinum

surface oxides of higher oxidation states, e.g. $Pt(OH)_3$ and PtO_2, were formed for potentials above 1.24 V vs. RHE. Assuming that the only carbon-containing species at the surface is adsorbed CO, reaction then occurs between CO_{ads} and an adsorbed oxygen-containing species, which depends strongly on potential. For simplicity, equation (8) is assumed to apply at potentials below oxide formation (0.75 V) while equation (9) represents the stripping of CO_{ads} with platinum oxide present.

$$Pt(site) + H_2O \rightarrow Pt - OH + H^+ + e^- \quad (7)$$

$$Pt - OH + Pt - CO \rightarrow 2Pt(site) + CO_2 + H^+ + e^- \quad (8)$$

$$PtO + Pt - CO \rightarrow 2Pt(site) + CO_2 \quad (9)$$

Although considerable effort has been made to elucidate the exact mechanism of methanol oxidation at platinum and platinum-based electrodes, an exact description of the reaction mechanism still remains unclear. Specifically, the main issue, which remains controversial, is whether the adsorbed CO formed during methanol electrooxidation is a necessary intermediate in a serial pathway mechanism, as described by equation (10) and (11) or (12), or an unwanted poison in a parallel reaction mechanism that leads to a stable oxidation product (CO_2, formic acid and formaldehyde) through short-lived intermediates, equations (13)-(15). However, both formic acid and formaldehyde oxidation may subsequently lead to CO_{ads} formation.

$$Pt - CH_3OH \rightarrow Pt - CO + 4H^+ + 4e^- \quad (10)$$

$$Pt - CO + H_2O \rightarrow Pt(site) + CO_2 + 2H^+ + 2e^- \quad (11)$$

$$Pt - CO + Pt - OH \rightarrow 2Pt(site) + CO_2 + 2H^+ + 2e^- \quad (12)$$

$$CH_3OH + H_2O \rightarrow CO_2 + 6H^+ + 6e^- \quad (13)$$

$$CH_3OH + H_2O \rightarrow HCOOH + 4H^+ + 4e^- \quad (14)$$

$$CH_3OH \rightarrow HCHO + 2H^+ + 2e^- \quad (15)$$

Existence of a parallel path in the oxidation of methanol has been the subject of many studies, e.g., [14,29-38]. Stuve and co-workers have extensively studied the possibility of a dual pathway in the oxidation of methanol. Their major concern is that if the serial mechanism is found to be operative, a technically feasible (low-temperature) direct methanol fuel cell will be hard to attain, and further study in this area would be of no practical use. Researchers argue whether this is true or not. On the contrary, a finding in favour of the parallel

mechanism will boost research interest in this field in order to control the selectivity of the reaction.

Early studies by Parsons and VanderNoot [3] assumed that the formation of the poison species CO_{ads} is an unwanted parallel reaction. Later studies performed on single crystal surfaces [29,31,32,35] indicated that methanol oxidation can also proceed via a parallel path under certain reaction conditions. They observed an excessive charge (more oxidative charge than that needed for the formation of CO_{ads}) at potentials where adsorbed CO is not oxidised on Pt(111), Pt(110) and Pt(100) surfaces. The authors simply attributed these extra charges to the formation of CO_2. Chronoamperometric measurements on a platinum electrode by Wieckowski and co-workers strongly indicated the possibility of a parallel pathway in the electrooxidation of methanol [36]. However, differential electrochemical mass spectrometry (DEMS) studies by Vielstich and Xia [14] on a platinum electrode demonstrated that the formation of CO_2 can only be detected at potentials at which adsorbed CO is also oxidized. The authors assumed that the formation of CO_2 practically proceeds via the intermediate CO_{ads} only. In this study, the possible formation of other products or long-lived intermediates was not accounted for, and some suggested reaction models are based on many assumptions. DEMS work by Baltruschat and co-workers [37] showed the validity of a parallel path mechanism on platinum in sulphuric acid by determining the current efficiencies of CO_2 during methanol oxidation. CO_2 is formed via CO_{ads} oxidation in a serial reaction, while dissolved intermediates, i.e. formaldehyde and formic acid, are also formed in a parallel reaction. They also found that high methanol concentrations favour the reaction path via dissolved intermediates and that the current efficiency of CO_2 formation increases on very rough and porous platinum electrodes.

In this study we report a quantitative evaluation of methanol oxidation on platinum in sulphuric acid by focusing on a comparison of the fast and slow timescale kinetics of methanol oxidation. We use conventional voltammetry for the fast and slow time scales, and also a fast pulse-sweep sequence similar to a potential sequence first employed by Lamy and co-workers in perchloric acid on polycrystalline platinum [39] and later on Pt(100) single crystal [40]. More recent work by Wieckowski and co-workers employed a similar potential-step potential-sweep sequence on Pt electrodes in sulphuric acid with methanol and deuterated methanol [15,16,36] for the faster time scale. In this method a pulse sequence cleans the surface of pre-adsorbed intermediates, the potential is held at a selected value for a predetermined time, and then the effects of adsorption during the hold period are determined by looking at the peaks in a fast positive-going “analysis” sweep.

2.2 Experimental

Polycrystalline platinum wire (Johnson-Matthey 99.998%) was sealed in glass and used as the working electrode in a glass cell of conventional design, with a hydrogen reference electrode in the same solution (RHE) and a platinum mesh as the counter electrode. Potentials in this work are all quoted against RHE. The potential program of Figure 1 was generated by using a Princeton Applied Research Model 175 waveform generator to generate the pulse sequence and a separate PAR 175 waveform generator to generate the subsequent sweeps. A wave generator, model 166 from Wavetek, was used to control the time of hold on the adsorption potential. The potential was applied to the cell via a custom-built fast potentiostat, and the measured current and potential waveforms were then digitized (Picotech ADC212) for subsequent analysis. No IR compensation was used. The results are essentially the same regardless of cell design. Due to the fast voltammetry, the lower reversal potential was adjusted so that all hydrogen adsorption peaks could be seen. All reported current and charge densities are calculated from the true surface area, determined by integrating the hydrogen adsorption peaks in a cyclic voltammogram with a sweep rate of 100 mV s^{-1}, and by assuming a charge density for a flat platinum surface of 220 μC cm^{-2}.

The platinum electrode was cycled at 100 mV s^{-1} for more than one hour in sulphuric acid prior to all methanol experiments, and for a further 2 hours after methanol was added before experiments were conducted. During the fast cyclic voltammetry and potential step-sweep experiments the current densities slowly increased when methanol was present in the electrolyte, indicating some boost in the electrode activity over the time period of many hours to complete a whole set of these combined experiments. The current densities were therefore normalized to a reference curve to correct for this enhanced activity, taken to be one of the experiments without methanol. This correction was never more than 5%.

Sulphuric acid (traceselect; > 95%) was supplied by Fluka Chemica. Methanol (electronic use grade, residue free) and formic acid (p.a.) were supplied by Acros organics. Methanol-d_4 (99.8 Atom% D) was supplied by Chiron AS. CO (industrial grade) and Ar (99.999%) were provided by Aga. The glass cell and electrodes were cleaned before each experiment in hot chromic acid for at least three hours and rinsed thoroughly with high-purity water (> 18 MΩ cm). Unless otherwise specified, all experiments were carried out in 0.6 M CH_3OH and 0.5 M H_2SO_4. All experiments were performed at room temperature, 23 °C.

Combined potential step and potential sweep experiment:

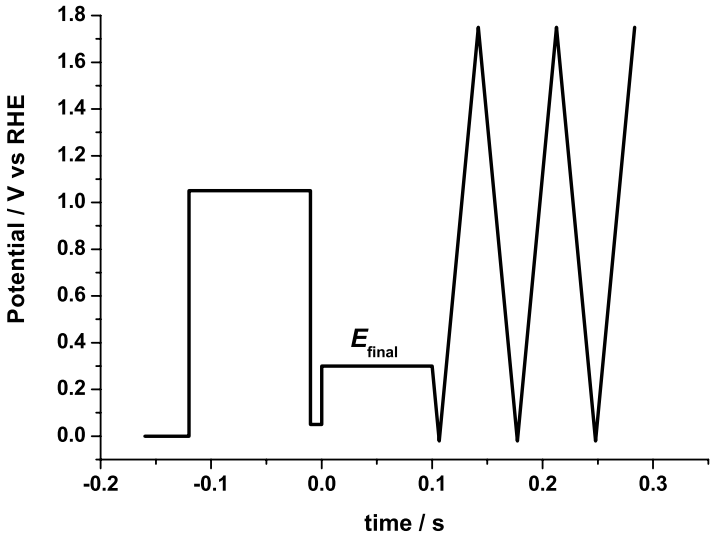

Figure 1 Potential program used in the combined step-sweep experiments, showing the oxidizing pulse at 1.05V, oxide removal at 0.05 V, preparation potential hold at E_{final}, and then analysis sweeps between -0.02 V and 1.75 V.

The combined potential step-sweep experiments utilized a similar pulse-sweep sequence as shown in Figure 1. The first pulse ("oxidizing pulse") at 1.050 V is to oxidize any pre-existing adsorbed intermediates. The 10 ms hold at 0.050 V (starting potential) then reduces platinum oxide made in the previous step. The next pulse to E_{final} is referred to as the preparation step and allows for adsorption of decomposition species. The preparation step is varied both in time and potential. The subsequent voltammetric sweeps probe the adsorption that occurred at E_{final}, and may occur with the initial segment sweeping either up or down. In this work we preferred a negative initial scan direction in order to use decreases in hydrogen adsorption/desorption charges for the first potential sweep as a diagnostic for more strongly adsorbed species. The reversal potentials in the cyclic voltammetry were the onset of hydrogen evolution (-0.02 V) and oxygen evolution (1.75 V); these potentials at the fast sweep rates (50 V s^{-1}) differ from those at slow scan rates due to the kinetics of these reactions and also to IR drop.

2.3 Results and Discussion

2.3.1 Cyclic voltammetry

Slow voltammetry

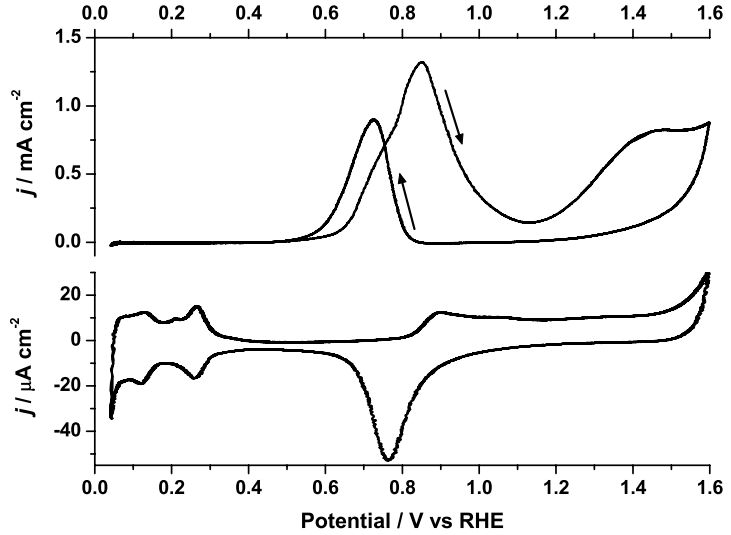

Figure 2 Cyclic voltammograms showing the oxidation of methanol on platinum; 10 mV s^{-1} sweep rate with H_2SO_4 and 0.6 M CH_3OH (top) and H_2SO_4 alone (bottom).

The characteristic potential regions for methanol oxidation on platinum in relationship to the behaviour in H_2SO_4 alone are discussed in reference to the curves in Figure 2, which shows voltammograms of platinum in sulphuric acid with 0.6 M methanol and without methanol at a sweep rate of 10 mV s^{-1}. The hydrogen region (0 - 0.3 V) shows the hydrogen underpotential deposition (UPD) peaks in base electrolyte and these are suppressed in the presence of methanol due to formation of adsorbed CO on the hydrogen sites. The current for methanol oxidation commences at around 0.5 V where the blank shows only charging of the double-layer. The oxygen source in this potential region is assumed to be adsorbed or dissociated water. At low concentrations and slow sweep rates, the main methanol oxidation peak occurs at 0.7 V and is followed by a second peak at 0.85 V where platinum oxide formation occurs. The oxide that starts to form at potentials above ca. 0.75 V is assumed to provide the oxygen source for methanol oxidation that occurs here. At higher methanol

concentrations, this second peak predominates and the first peak appears now only as a shoulder as can be seen from Figure 2. The decrease in oxidation current at potentials above 0.85 V corresponds to the presence of a more extensive surface oxide film that inhibits the methanol oxidation substantially. When reversing the potential at 1.6 V and performing a negative-going sweep, the current remains anodic for a little while but decreases. When the oxide is reduced, Pt sites on the electrode are again available for methanol oxidation and the current increases. The resulting oxidation peak is shifted slightly to more negative potentials than on the positive-going oxidation peak. At more negative potentials, the current decreases due to an increased coverage of adsorbed CO, which is recognized as the catalyst poison in methanol oxidation on platinum. However, if there are no alternative paths to form CO_2, then CO is more like a strongly bound intermediate rather than a poison.

Fast voltammetry and dependence on sweep rate

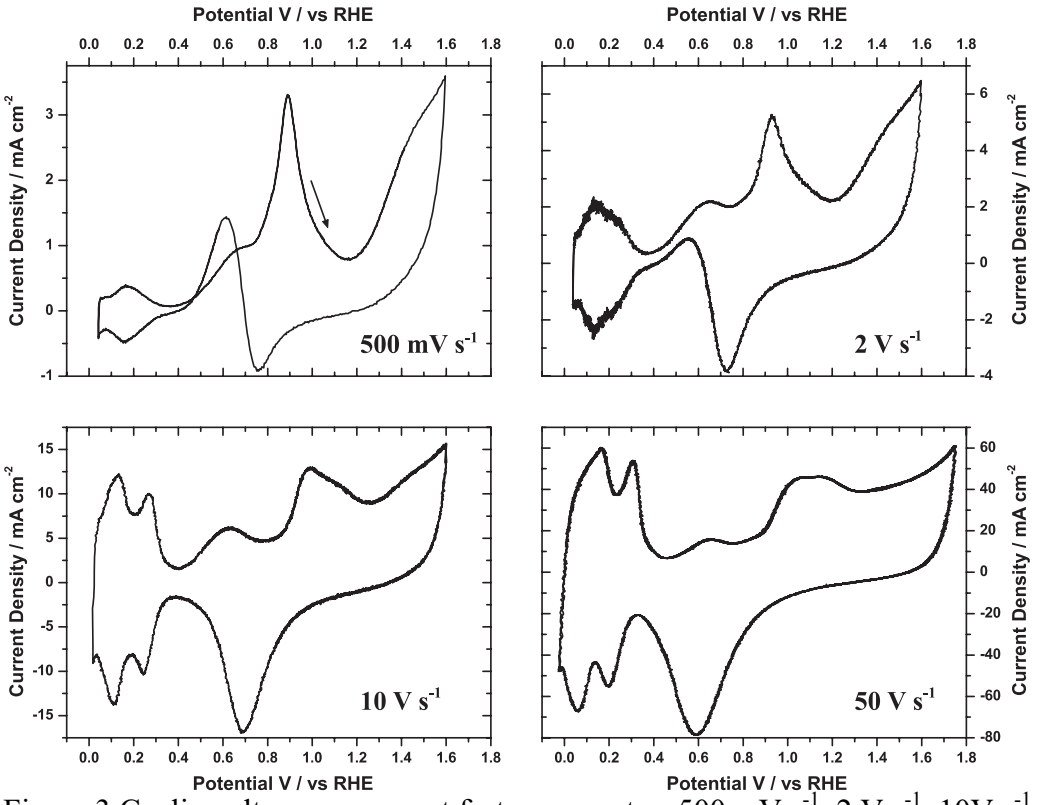

Figure 3 Cyclic voltammograms at fast sweep rates, 500 mV s^{-1}, 2 V s^{-1}, 10V s^{-1} and 50 V s^{-1}.

Selected voltammograms for increasing sweep rates are given in Figure 3 for 0.5, 2, 10 and 50 V s^{-1}. Relevant potential regions to discuss are the hydrogen region, double-layer region and the oxide region. Clearly, the characteristic oxidation peaks related to methanol oxidation that occur in the lower sweep rate voltammograms, are gradually changing and seem to be less pronounced as the sweep rate is increased. The shoulder feature in the positive-going sweep observed in Figure 2 seems to be separated from the main oxidation peak, appearing as a small peak in the double-layer region at high sweep rates. The methanol oxidation in the positive-going sweep does not cease to exist, but the dependence on the sweep rate is not as strong as for the hydrogen adsorption/desorption and platinum oxide formation/reduction, leading the latter to dominate the voltammograms at high sweep rates. It is well known that pure surface reactions are directly proportional to sweep rate since the same charge must be involved. Figure 4 demonstrates a linear dependency of the current density of the peak (shoulder at lower sweep rates) in the double-layer region plotted against the square root of sweep rate. Diffusion control during methanol oxidation in the double-layer region is evident by this square root dependence. Wieckowski et al. [41] suggested, based on the sweep rate relationship of this peak, that methanol molecules diffuse on the surface to some active sites, and that surface diffusion is rate limiting. Furthermore, Lu et al. [36] comment that the highest current in their study during steady state measurements by chronoamperometry is three orders of magnitude less than calculated from the Cottrell equation (they are also in 0.6 M methanol) suggesting no diffusion limitation. However, in fast cyclic voltammograms we are far from steady state so diffusion may be a viable mechanism.

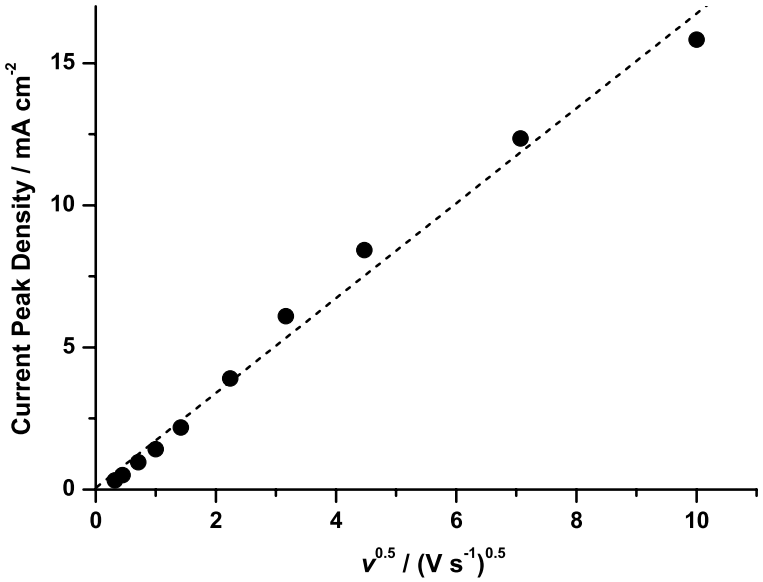

Figure 4 Current density at the methanol oxidation peak in the double-layer region in the positive-going scan plotted versus the square root of sweep rate from 100 mV s^{-1} to 100 V s^{-1}. For sweep rates lower than 1 V s^{-1}, the peak current was taken to be the current corresponding to the minimum slope in a *j-E* plot at the shoulder. The dashed line represents the linear regression line.

On the other hand, the oxidation peak in the negative-going sweep is eventually disappearing completely. This is mainly related to the irreversibility of the platinum oxide formation/reduction combined with the blocking effect of platinum oxide, which eventually shuts down any methanol oxidation in the double-layer region during the negative-going scan. The potential region at which the platinum oxide is being reduced is extended to include even lower potentials as the sweep rate is increased and eventually there is no time left for methanol oxidation to happen. We will show later that the kinetic delay for methanol oxidation is higher at lower potentials. The disappearance of the methanol oxidation peak in the negative-going scan at elevated sweep rates has previously been shown by Pletcher and Solis [42], who performed potential sweeps with 0.1 M methanol in sulphuric acid at a sweep rate of 1.5 V s^{-1}. They concluded that the time at 1.5 V s^{-1} after oxide reduction was not enough to obtain the anodic peak easily seen at slow scan rates.

Relevant potential regions and integration limits

Now we want to look closer on the main effects of having methanol in the electrolyte at fast sweep rates. Relevant voltammograms at 50 V s^{-1}, with and without methanol in sulphuric acid, are given in Figure 5. First of all we notice that there are no significant differences between the two curves in the negative-going scan. In the positive-going scan, three potential regions are of essential interest in this study, and are represented by the shaded regions in Figure 5. They represent the charges related to what we refer to as the hydrogen desorption (I), methanol oxidation (II) and CO stripping (III). An important and difficult task in this context is to decide upon the right potential regions for estimating the charges related to the different processes. In this work we assume the following integration limits: from 0 V up to 0.41 V (*hydrogen region*, I), from 0.45 up to 0.95 V (*methanol oxidation*, II) and thirdly from 0.98 V up to 1.4 V (*CO stripping*, III). We assume that all the CO_{ads} formed in the methanol oxidation peak (II) is oxidized in the latter potential region (III).

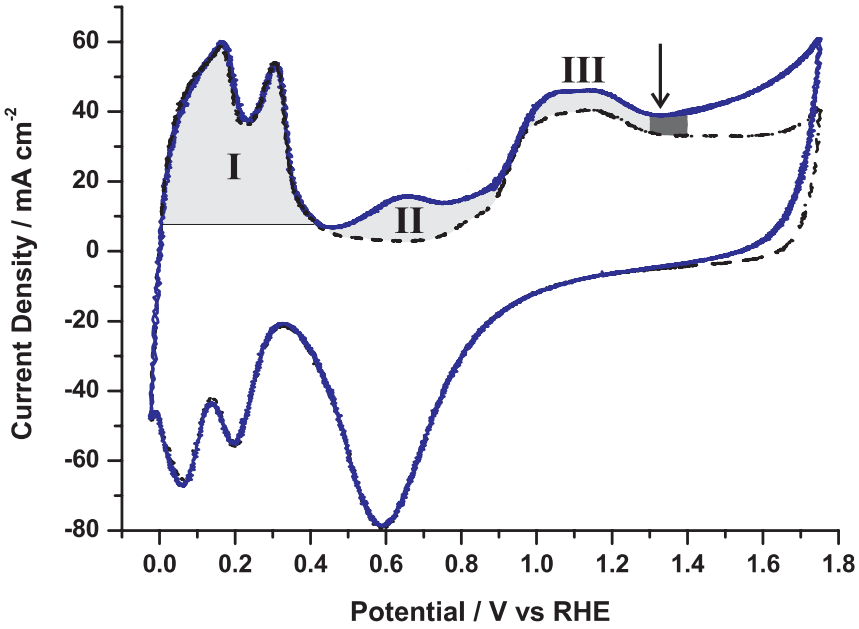

Figure 5 Voltammograms recorded at a sweep rate of 50 V s^{-1} with methanol (solid line), and in sulphuric acid alone (dashed line). The shaded areas represent the charge regions measured: hydrogen desorption (I), methanol oxidation in the double-layer region (II) and CO stripping (III). The arrow points at the minimum at 1.32 V, while the dark shaded area points out the uncertain determination of the upper potential integration limit of region III.

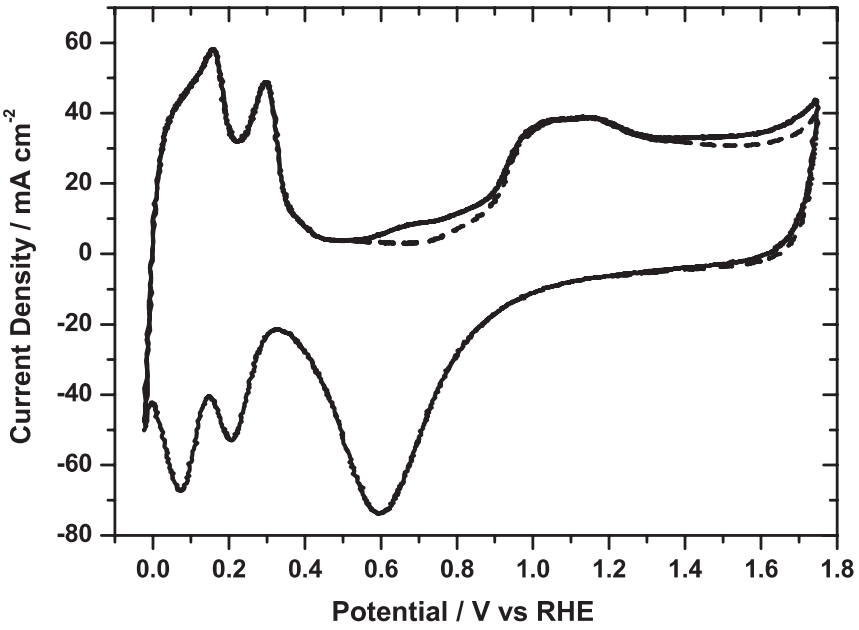

Figure 6 Continuous cycles (second cycles) for a polycrystalline platinum electrode with (solid line) and without (dashed line) deuterated methanol present in sulphuric acid electrolyte at 50 V s^{-1}. Notice the small oxidation current in the double-layer region and no corresponding stripping peak.

The integration limits for the CO stripping region (III) were the hardest to establish. A closer look at the upper end of the CO stripping and at higher potentials shows that the plateau current with methanol present lies above the recorded current in blank electrolyte. The additional current at high potentials is most likely methanol oxidation happening due to a preferential change in the oxide structure (this effect is visualized in a similar voltammogram for deuterated methanol, Figure 6). There is an overlap between this additional methanol oxidation current and the remaining part of CO stripping current complicating the determination of the upper potential integration limit. This will be of most significance during measurements with small currents involved in the CO stripping peak, like continuous cycling, involving small CO_{ads} coverage. As can be seen from Figure 7 and Figure 9, the current response from methanol in the electrolyte, at potentials above about 1.4 V is found to be independent of hold times and adsorption potential (also independent of cycle number); evidence for negligible CO stripping at higher potentials. In fact, in the combined potential step and potential sweep experiments 1.4 V was preferred, since it gave a satisfactory trade-off between short times and low coverage versus long times and high coverage.

This separation of events in the voltammogram is a vague proposition, but very useful as charge arguments can be used to indicate a parallel pathway in the methanol oxidation at very fast sweep rates.

Continuous cycling and indication of poisoning path only

Now we try to show that the process in the methanol oxidation peak, during continuous cycling, is related to the formation of adsorbed CO alone based on charge arguments in this peak and the following CO stripping peak. This is in agreement with Vielstich and Xia [14]. The starting point is Figure 5, which shows continuous cycles with and without methanol present, together with reactions (10) and (11).

Methanol oxidation to form adsorbed CO, reaction (10), involves four electrons, while the stripping of CO to form CO_2, reaction (11), involves two electrons. Therefore, if these are the only reactions occurring in the separated potential regions (II and III), the charge density in region II is expected to be twice the charge density in region III. In fact, the measured charge density related to the methanol oxidation peak (region II) was found to be approximately twice the charge as in the following CO stripping peak after subtraction off the underlying blank currents and carefully selecting the integration limits. This is in agreement with what we expected, and we conclude that the current observed in the methanol oxidation peak in the double-layer region (region II) during continuous cycling is only due to the dissociative adsorption of methanol, where the dehydrogenation steps and subsequent oxidation of hydrogen gives the current observed. The adsorbed CO strips off once platinum oxide is formed in the potential region III, completing the oxidation of methanol. Papoutsis et al. [39] estimated the charge density of the CO stripping peak in a similar experiment with methanol in perchloric acid, but no attempts were made to correlate this charge to the charge in the peak in the double-layer region.

Combining this results with the indications of diffusion control (Figure 4) and the fact that no decrease in hydrogen charge was observed, we conclude that only the serial path, via adsorbed CO, exists during continuous cycling, with the first step being diffusion controlled dissociative adsorption of methanol directly from the bulk electrolyte.

Alternatively, formation of formic acid from methanol, reaction (14), will give the same charge as formation of CO_{ads} (reaction (10)). Formic acid is a soluble

product that can diffuse away from the electrode and thus escape further oxidation. If this happens, the CO stripping peak will diminish. Interestingly, even though we don't observe this for methanol, it is exactly the behaviour we observe when deuterated methanol is employed (Figure 6), in agreement with Lu et al. [36]. Formic acid and CO_2 formation have been shown by IR spectroscopy to commence at potentials around 0.45 V [43].

Measured charges and corrections

One of the most challenging assignments is to correctly adjust for the double-layer charging effects. The simplest way to surmount this difficulty is just to consider the double-layer charge to be identical to the background response, i.e. without any organic influence as we did for the continuous cycling in the previous section. A more rigorous treatment has been discussed earlier by Lamy et al. [39,40] and Orts et al. [44]. In this work we modify their double-layer corrections to be based on the coverage of CO from the preparation step as determined from the decrease in hydrogen desorption charge in the first potential cycle. The IR drop itself was not compensated for.

First of all, the double-layer charging current in the hydrogen region was assumed to be equal to the experimental current density at 0.41 V and constant through the hydrogen region. This is a coarse approach and probably does not perfectly correct for double-layer charging. The potential range from 0 and up to 0.41 V was simply justified by looking at the voltammogram and judging where the hydrogen desorption region ended. The potential region is broader than found for lower sweep rates (Figure 2), due to irreversibility in the UPD process and perhaps also due to the uncompensated solution resistance. In fact, the observed charge density was slightly higher than the 220 μC cm^{-2} that is considered as an appropriate approximation of a monolayer of hydrogen on polycrystalline platinum electrodes. The decrease in the hydrogen desorption charge was measured as the hydrogen charge without methanol present minus the charge under the curve with methanol present. A complete coverage (θ_{CO} = 1) was assumed to exist at long times at potentials around 0.5 V, and the corresponding decrease in hydrogen charge was used as the maximum suppression value. Similarly, no decrease in hydrogen charge was assumed to be equal to zero coverage. In addition, the following were assumed: i) for maximum coverage of CO (θ_{CO} = 1), no extra CO_{ads} is formed during the initial potential sweep prior to CO stripping, ii) when no CO_{ads} is formed during the preparation step, the CO formed during the first potential cycle equals the amount of CO formed in the following cycle, and iii) the background current

from platinum oxide formation in sulphuric acid is constant and independent of θ_{CO} and cycle number. The latter can be deduced from the fact that the oxide reduction peak is the same in both cases showing that the state of the oxidized surface is the same by the positive end of the sweep, despite the higher plateau charge in the methanol experiment than in the blank. This is related to a feature of the oxide kinetics, that the oxide charge is largely determined by potential rather than time or pre-treatment. For example, in sweep-hold-sweep experiments, the oxide plays "catch-up" and arrives at the same charge as in an interrupted sweep [45]. The practical implication of this is that it is a legitimate procedure to subtract off the oxide charge of the blank in order to deduce the charge for CO oxidation. Finally, the correction of CO stripping charge was then done by assuming that the CO stripping is linearly dependent on the coverage found from the suppression of hydrogen desorption charge.

$$q_{\text{CO-stripping}} = q_{\text{tot}} - \left[\left(q_{\text{Second cycle}} - q_{\text{Background}}\right)\cdot\left(1-\theta_{\text{CO}}\right) + q_{\text{Background}}\right] \qquad (16)$$

where q_{tot} represents the area under the curve with methanol present from 0.98 V to 1.4 V, $q_{\text{Second cycle}}$ represents the area under the curve in the same potential region, from 0.98 V to 1.4 V, for the second or subsequent cycles, and $q_{\text{Background}}$ represents the charge without methanol present from 0.98 V to 1.4 V.

This procedure of eliminating any contribution of CO formed during the initial scan is by no means conclusive, but it represents a solution closer to the real values than just subtraction of the corresponding charge from a solution without methanol. One typical complication is the possible dislocation of oxide formation due to adsorbed CO altering the true integration limits. This effect was found to be of minor importance here and therefore disregarded.

A similar procedure was employed when determining the charge related to the dehydrogenation reactions during methanol oxidation (region II). Here the correction for the effect of CO adsorption on the double-layer charge in the potential region 0.45 V to 0.95 V is the critical factor. This is found by defining a minimum double-layer charge, $q_{\text{dl}\,(\theta_{\text{CO}}=1)}$, at complete saturation of CO_{ads}.

$$q_{\text{Methanol Peak}} = q'_{\text{tot}} - \left[\left(q'_{\text{Background}} - q_{\text{dl}\,(\theta_{CO}=1)}\right)\cdot\left(1-\theta_{\text{CO}}\right) + q_{\text{dl}\,(\theta_{CO}=1)}\right] \qquad (17)$$

where q'_{tot} represents the area under the curve with methanol present from 0.45 V to 0.95 V, $q'_{\text{Background}}$ represents the charge from 0.45 V to 0.95 V without methanol present. The critical uncertainty is of course the proposed linear effect of CO_{ads} on the double-layer charge. Consequently, during continuous cycling, where all CO is formed in the methanol oxidation peak, the charge related to region II is simply the total measured charge (with methanol) minus the charge

obtained without methanol present, as indicated in Figure 5. Although this may be close to the actual charge for continuous cycling, correcting for the double-layer charge is always difficult.

In a similar work, Wieckowski and co-workers [36] assume that there is a general rising current all the way along in the methanol voltammogram right up to the potential where platinum oxide forms, and so the peak in methanol oxidation is on top of this. This assumption was based on the general rising current obtained in the double-layer region when fast cyclic voltammetry was performed in sulphuric acid with deuterated methanol (see also Figure 6). No CO stripping charge was detected as the potential was swept into the oxide region. However, this assumption ignores the underlying process leading to this general rise in current, which seems unlikely to stem from an increased double-layer charge alone. It seems more logical to subtract off the blank, and assume that new processes are the difference. While this works well for low coverages, subtracting off the charge in the methanol-free solution in the double-layer region leads to negative charges at long adsorption times (high coverages). Obviously, methanol just being in the double-layer changes the capacitance, so such a subtraction is not correct. By modifying the double-layer charge correction, equation (17), we avoid this problem, but still it is just another way of approximating the real values.

2.3.2 Combined chronoamperometry with fast cyclic voltammetry

The experimental procedure is described in the experimental section of this chapter. Wieckowski and co-workers used a similar procedure with three oxidizing and reducing pulses before the preparation pulse on polycrystalline platinum [36]. However, we found that provided that the oxidizing potential was above 0.9 V, there was no difference in the first and subsequent cycles in the CO oxidation region, i.e., the peak for CO stripping at 0.98-1.4 V was minimized. In agreement with Franaszczuk et al. [15], we found that a 10 ms delay at the reducing potential was sufficient to reduce the oxide formed in the oxidizing step, and at the same time short enough not to let any noticeable amount of methanol chemisorb. (In their last publication on this subject, Wieckowski and co-workers [36] also applied a small pre-step (10 ms at 0.25 V) before the final step in order to reduce the charging current of the double-layer. We found that changing the starting potential from 0.05 V to 0.25 V had no effect on the voltammetric response in the combined potential step-sweep experiments).

As general findings, we observed that the oxide plateau (above about 1.4 V) is the same independently of hold time, preparation potential, upper reversal potential and cycle number. In addition, the reduction of the oxide (reduction peak at 0.6 V in the negative-going scan) is identical for all experiments (except when the upper reversal potential was changed), including the blank current response without methanol, in agreement with the findings for continuous cycling.

Varying the preparation potential

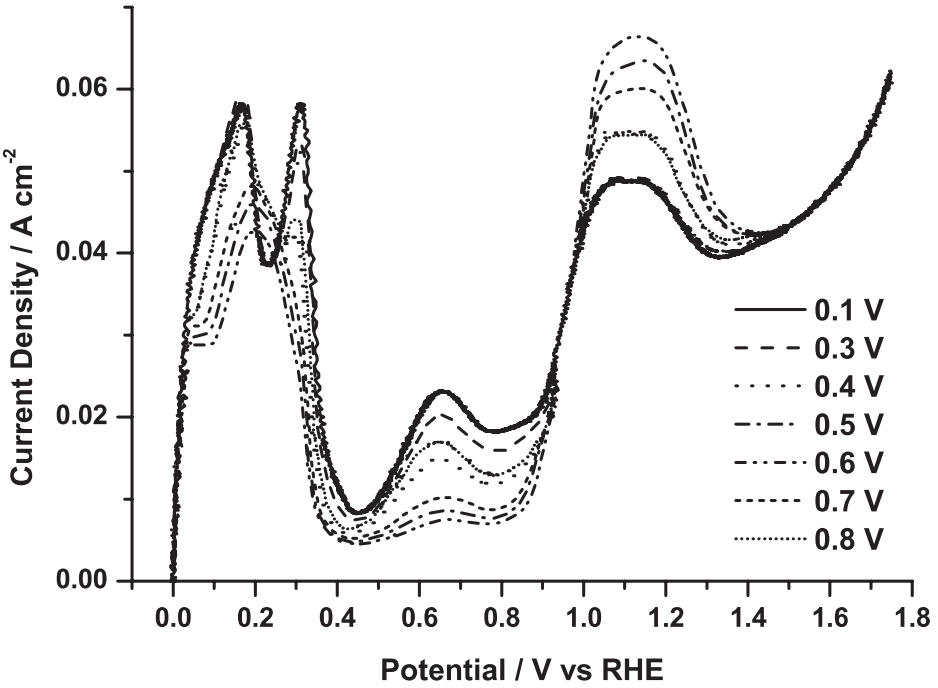

Figure 7 First cycle after negative initial sweep direction in sulphuric acid with 0.6 M CH_3OH after a preparation time of 100 ms with varying preparation potentials.

Figure 7 shows the positive-going sweep after an initial negative-going segment at a hold time of 100 ms at various preparation potentials. Here, 0.6 V shows the highest CO stripping charge and correspondingly the lowest hydrogen and methanol oxidation charge. Without doubt, the rate of CO_{ads} formation is increasing from 0.1 V up to 0.6 V. However, the decreased CO stripping charge at potentials higher than 0.6 V is most likely due to lower saturation coverage

rather than a slower formation of adsorbed CO. Similar measurements were done for a number of adsorption times.

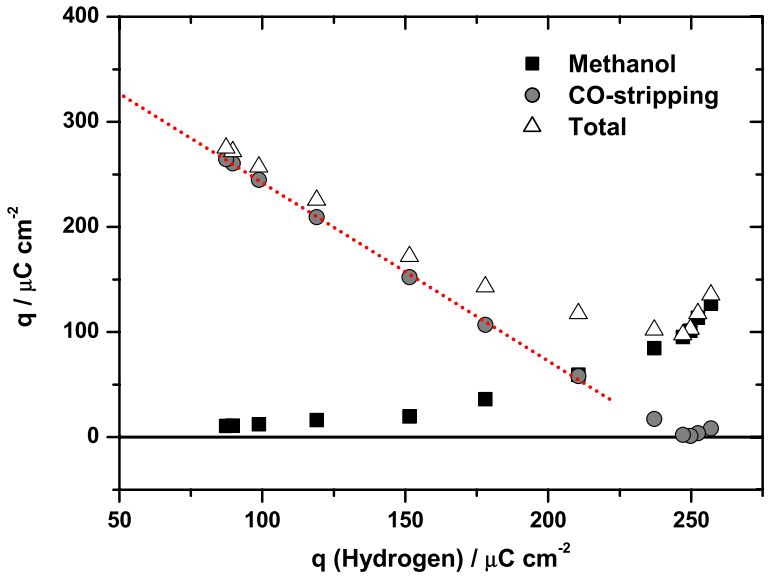

Figure 8 Methanol (squares, black), CO stripping (circles, grey) and total carbon-oxidation charges (triangles, open) plotted versus the hydrogen desorption charge. Preparation time fixed at 1 s at potentials from 50 mV up to 0.6 V. The dotted line represents a linear regression line.

Straight lines are formed when methanol and CO-stripping charges are plotted versus the hydrogen charge (Figure 8), clearly indicating that the charges are dependent on each other. This is not surprising as they compete for the same sites on the surface. For low potentials and short times, a small CO stripping charge is observed while the hydrogen charge is large. As the preparation potential or time of hold is increased, the hydrogen adsorption/desorption peaks and the methanol peak in the double-layer region are being suppressed while an excess current above the blank in the CO stripping region is observed. This is expected as an increased amount of adsorbed species formed during the preparation potential leads to some blocking of the hydrogen adsorption-desorption reaction and also some blocking of the methanol oxidation. The CO stripping peak will be higher if there is an increased amount of adsorbed species formed in the preparation step. Finally, a further increase in the preparation potential leads to a lowered CO stripping peak due to the establishment of an equilibrium between CO adsorption and CO stripping at these potentials during the preparation step, through the reaction between adsorbed CO and some form of surface bonded water (e.g. dissociated water) or platinum oxide leading to carbon dioxide production.

Varying the preparation time, kinetic delay

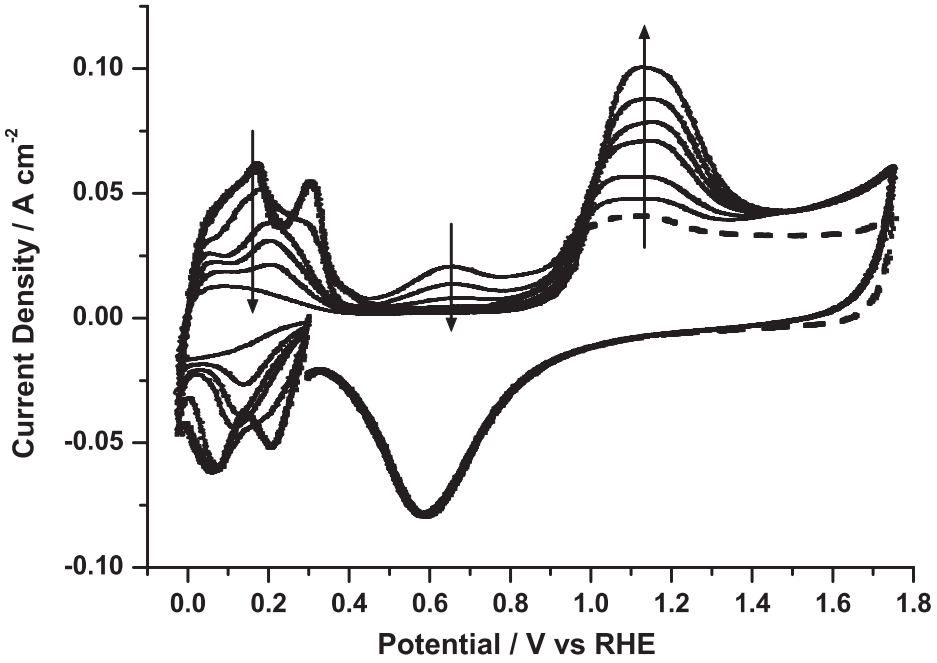

Figure 9 First cycles with selected hold times 20 ms, 1 s, 5 s, 10 s, 20 s and 100 s at a preparation potential of 0.300 V. The dashed line shows the current from an identical experiment in sulphuric acid alone with a preparation time of 100 ms. The arrows indicate the trend observed by increasing the hold time.

A typical experimental result when changing the hold time at a constant preparation potential is given in Figure 9 for a preparation potential of 0.3 V. Increasing the hold time gives a similar visual effect as increasing the potential from about 0.1 V up to 0.6 V with a constant preparation time (Figure 7). The hydrogen adsorption/desorption and methanol peaks decrease while the CO stripping charge increases. The corresponding charges from Figure 9 can be extracted and plotted versus a logarithmic time scale to indicate the rate of formation of adsorbed species at this preparation potential. Of particular interest is the CO stripping charge, and Figure 10 plots the CO stripping charges versus a logarithmic time scale for preparation potentials 0.3, 0.4, 0.5 and 0.6 V. Increasing the hold time gives rise to an increased CO stripping charge and the charge increases with time until the saturation coverage of adsorbed species at that potential is reached.

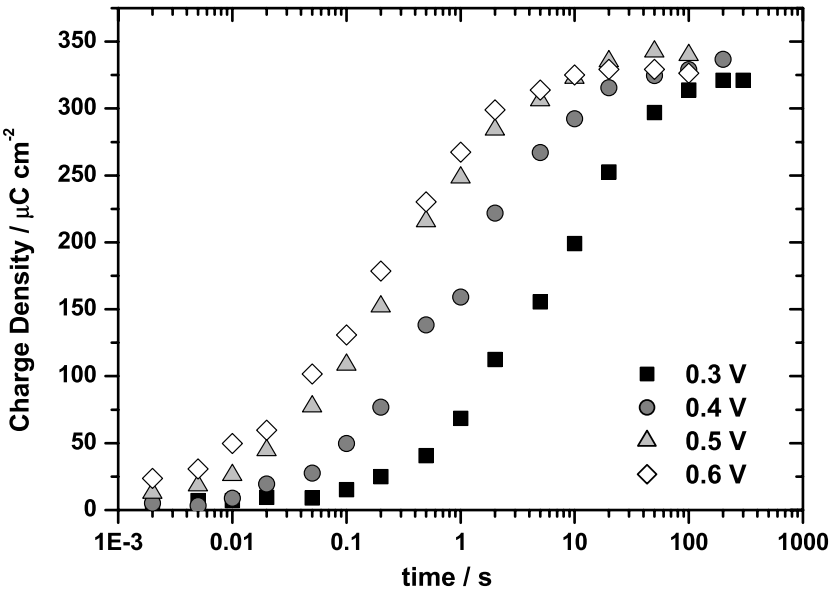

Figure 10 Charge of CO stripping peak (first cycles) versus holding time for different preparation potentials: 0.30 (squares, black), 0.40 (circles, grey), 0.50 (triangles, light grey) and 0.60 (diamonds, open) V.

A "kinetic delay" below 50 ms was found earlier by Wieckowski and co-workers at a final potential of 0.37 V [36] and they correlated this to the sluggishness in the CO uptake from methanol decomposition on platinum at the beginning of the reaction. Hence, this is the minimum time the electrode must be held at the preparation potential in order to form adsorbed CO from the dissociative adsorption of methanol. Figure 10 demonstrates the potential dependence of the kinetic delay. At 0.3 V a minimum time of about 0.1 second is needed to get formation of adsorbed CO. This fact is useful in our discussions about a parallel pathway in the methanol oxidation. Nevertheless, the saturation charge (coverage) is more or less equal for potentials between 0.3 and 0.6 V.

Saturation charge of CO

As pointed out earlier by Beden, Bewick and Lamy [46] it is interesting that large amounts of adsorbed CO on platinum electrodes have been found, and confirmed by EMIRS (electrochemically modulated infrared reflectance spectroscopy), as resulting from the decomposition of several organic compounds like methanol [47], formaldehyde [48] and formic acid [46]. Adsorbed CO is also detected from the reduction of CO_2 [49], and by bubbling CO(g) [50] in the electrolyte. Even though all these systems produce large

amounts of adsorbed CO, the voltammograms clearly indicate different mechanisms, which also vary with surface structure (e.g. [51]), concentration and transport characteristics.

Gilman introduced the stripping of CO by cyclic voltammetry as a method of determining the CO coverage as early as 1962 [52]. The method consists of determining the charge required to remove a monolayer of adsorbed CO from the surface during the positive-going scan. Figure 11 shows charge density data of the saturation coverage at several potentials for methanol, formic acid and CO, by employing a sufficiently long hold time to make sure that saturation coverage is reached, and subsequently measuring the CO stripping charge by the means of a fast potential sweep (Figure 1). The maximum charge obtained in CO and formic acid is roughly the same at low potentials, while the saturation charge from methanol-containing electrolyte either suggests that the adsorbed CO binds differently to the surface or that saturation is reached at a lower coverage. Recall that the adsorption of CO from the different systems happens on a freshly reduced platinum electrode, and thus can not directly be compared to the behaviour in slow d.c. voltammograms (in fact it should be more closely related to the fast negative-going sweep where oxidation happens on a freshly reduced platinum surface).

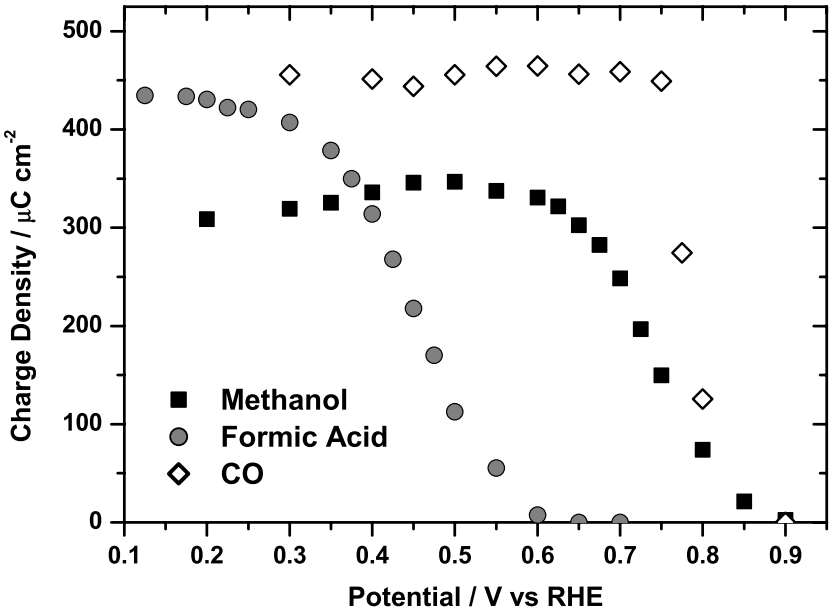

Figure 11 Saturation charges measured at various potentials in methanol (squares, black), formic acid (circles, grey) and by dissolved CO (diamonds, open).

Now we need to establish the different types of adsorbed CO that one may obtain at platinum since they will possess a different number of electrons per surface site (usually referred to as N_{eps}). CO_{ads} may form a linear, bridge or threefold bond to the surface leading to 2, 1 and 2/3 electrons per site respectively. Intuitively, Figure 11 suggests that the adsorbed CO formed from formic acid or dissolved CO is a complete monolayer of linear bonded CO (2 electrons per surface site) with a stripping charge of about 440 μC cm^{-2} (the hydrogen adsorption/desorption charge is assumed to be 220 μC cm^{-2}, equal to 1 monolayer of hydrogen). The adsorbed CO from the methanol system has a maximum saturation charge density of about 350 μC cm^{-2} at potentials around 0.5 V, and seems to consist of a mixture of linearly bonded CO together with bridge and threefold bonded CO. Assuming only linear bonded CO, a saturation charge of 350 μC cm^{-2} implies a coverage of 0.8 monolayer (4/5 CO/Pt).

Recent studies combining stripping voltammetry and FTIR spectroscopy on Pt(111) [53] suggested a maximum coverage of adsorbed CO from dissolved CO in CO-free solutions of 0.68 and a larger coverage of about 0.75 when CO was present in the solution. However, other voltammetric studies by Gasteiger et al. [54] have shown that the saturation coverage of CO from dissolved CO on polycrystalline platinum is in fact closer to 0.9 monolayer (400 μC cm^{-2}, recorded with a sweep rate of 50 mV s^{-1}). Without being too conclusive, the measurement of the saturation charge densities suggests that the adsorbed CO from the different systems has qualitatively different properties that play an important role in designing catalysts for the different systems.

Interestingly enough, the saturation charges start to decrease at significantly different potentials for the three systems shown in Figure 11. For CO adsorption from dissolved CO, the saturation charge is not decreased until platinum oxide is formed at potentials about 0.75 V, thus indicating that a compact CO layer is not readily being oxidized by adsorbed water. However, it has been shown [55] that when CO is chemisorbed on a polycrystalline platinum electrode while employing an adsorption potential below about 0.2 V, bulk CO can be oxidized at a lower potential than that of the onset of platinum oxide formation in a so-called pre-wave.

Furthermore, Figure 11 shows that the saturation charge of CO_{ads} from methanol is significantly lower than the maximum charge observed for dissolved CO and also from formic acid. This is in line with Hamnett [56], where a significantly reduced coverage was observed in the case of CO_{ads} from methanol through a thorough comparison of the spectroscopic features between CO_{ads} from methanol and from dissolved CO. He also concluded that the

formation of CO islands occurs to a lower extent for CO from methanol. A possible explanation for the low saturation charge of CO stemming from methanol is due to the requirements for a neighbouring free catalyst site for each dehydrogenation step (reactions (2)-(5)), which is further complicated as the coverage of CO_{ads} increases. Sun et al. [57] found that the dissociative adsorption of formic acid leads to a higher coverage of poisoning species as compared to dissociative adsorption of methanol, in other words, a higher selectivity toward CO_{ads} formation is obtained from formic acid than from methanol.

Figure 10 demonstrates that the rate of formation of adsorbed CO from methanol increases with preparation potential at least up to about 0.6 V, in agreement with Lu et al. [36]. Adsorbed CO is assumed to react with some kind of surface bonded oxygen-containing species, e.g. some form of surface bound water or dissociated water, at potentials higher than about 0.5 V, leading to the final oxidation product, CO_2. Iwasita and Xia [23] found that formation of adsorbed hydroxyl ions from water dissociation commences at about 0.5 V on Pt(111) in perchloric acid. Moreover, this reaction is enhanced as the potential is increased, thus leading to a lower saturation coverage of CO at higher potentials. Above 0.6 V, the saturation charge density from the methanol system is significantly lowered. In a similar study of formic acid decomposition on polycrystalline platinum, Lu et al. [58] found that the rate of CO_{ads} formation in this case decreased with preparation potential, which is in agreement with our observations at potentials higher than about 0.3 V. In fact, Sun et al. [59] found a maximum in poisoning rate on Pt(100) at a potential of 0.28 V at a low formic acid concentration in perchloric acid. The saturation charge of poisoning species, CO_{ads}, from formic acid decomposition significantly decreases at potentials higher than 0.35 V, i.e. where no underpotential deposited hydrogen is present. This suggests that a significant contribution to the poisoning stems from reaction between adsorbed organic species and underpotential deposited hydrogen.

It is striking how qualitatively dissimilar properties that the adsorbed CO possesses depending on its parent molecule and its decomposition paths. Understanding these properties is essential in designing CO-tolerant catalysts, which most likely differ in the optimum composition for various organic fuels, such as formic acid and methanol.

Rate of decomposition of methanol at lower potentials

Evaluation of the rate of formation of blocking species at lower potentials was investigated by applying a fast potential scan of 50 V s^{-1} between the hydrogen onset, and a potential where methanol oxidation occur with only negligible oxidation of CO (here: 0.5 V). Looking at the charge difference in the hydrogen region between the first initial cycles (Figure 12) gives an indication of how fast the surface is deactivated (or poisoned) by methanol decomposition products or intermediates (CO_{ads}). Each cycle has a specific time-duration where the methanol decomposition can happen. The hydrogen charge decreases slowly with cycle number indicating that some species from the methanol decomposition is gradually being adsorbed at the surface, blocking the surface for hydrogen adsorption. With continuous cycling, the blocking of the active platinum surface sites is slowly increasing, and the hydrogen charge is less than 10% of original value (1st cycle) after three hours of cycling. The charge is steadily decreased and approaching that recorded when CO is bubbled through the electrolyte (except that this deactivation happens much faster). It is worth pointing out that the maximum coverage of adsorbed CO from methanol seems to reach a higher value when employing such a voltammetric procedure compared to just adsorbing CO from a methanol-containing electrolyte by holding at a constant potential (Figure 11). This could be due to adsorption of other species, or more precisely, a different relative distribution of linear, bridge or triply bonded CO, compared to when holding the potential.

Although the first initial CO_{ads} formation from methanol doesn't require more than a fraction of a second, depending on potential (Figure 10), full coverage takes several hours to get by employing fast cyclic voltammetry with a low upper reversal potential as seen in Figure 12. Based on this we can say that complete adsorption of CO from a methanol-containing electrolyte is a relatively slow process on platinum at room temperature. In addition, by slightly increasing the upper reversal potential to potentials where the saturation charge-density starts to decrease (about 0.6 V), we found only a steady accumulation of CO from methanol to a complete coverage, which suggests that no noticeable formation of CO_2 happens in the fast potential sweep experiment thus supporting the finding of only a serial pathway during continuous cycling.

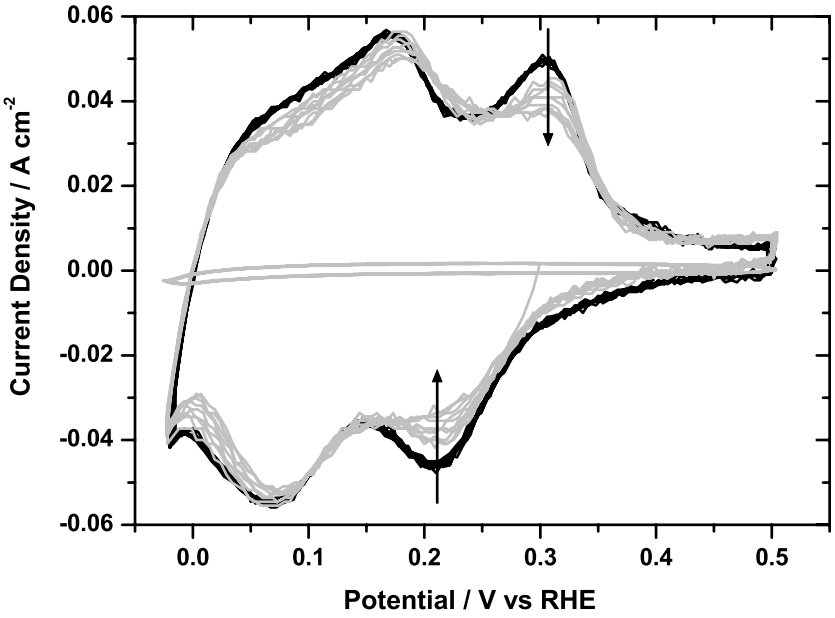

Figure 12 Fast voltammogram in the lower potential region with an upper reversal potential of 0.5 V. The black line represents an experiment performed in blank electrolyte for the first 5 cycles. The grey lines represent the methanol experiment; the ones with high hydrogen charge are the first few cycles, and the one with basically no hydrogen charge left is recorded after 3 hours of cycling.

Impurities

It could be argued that the decrease in hydrogen charge is a consequence of impurities in the electrolyte and faults in the cleaning procedure. If that were true we would expect the same trend in blank electrolyte as well, as long as the impurities are not entirely due to the methanol decomposition alone. In Figure 12 the current trace in supporting electrolyte represents in fact the first 5 cycles at 50 V s^{-1}, and any deterioration is negligible. We also continued cycling between 0.5 and -0.02 V in blank solution for another 20 minutes without any noticeable decrease in hydrogen charge. We take this as evidence that there is indeed a decline in hydrogen charge for increasing cycle numbers when methanol is added to the electrolyte, showing that methanol dissociates to form a complete adsorbed layer of CO over an extended time period.

2.3.3 Parallel pathway

A parallel path for the oxidation of methanol directly to CO_2 involves only short-lived intermediates, and includes several possible multi electron-transfer reaction steps, e.g. equations (13)-(15). The simple prediction of a dominating serial pathway mechanism through adsorbed CO during continuous cycling was made by correlating the charge in the methanol oxidation peak with the following CO stripping charge. No depression of the hydrogen region during consecutive cycling suggests a catalyst surface free of blocking species.

Now we want to show experimental evidence of a parallel path mechanism by employing our combined potential step-sweep experiment with low preparation potentials and short adsorption times (which is where we observe a kinetic delay). It is clear that any excess current in the methanol oxidation peak during the first cycle that cannot be accounted for in the following CO stripping, with no change in the hydrogen charge, must stem from reactions other than methanol dissociation leading to adsorbed CO. These could be the production of soluble species like formic acid, formaldehyde and CO_2 on the CO free surface, diffusing into the bulk electrolyte.

The kinetic delay illustrated in Figure 10 means that a hold time of, for example, 100 ms at 0.3 V prior to the fast cyclic voltammetry leads to no alteration of the hydrogen adsorption/desorption peaks relative to what is observed in a similar blank experiment (sulphuric acid only), and no increase in the CO stripping peak. Clearly, lower potentials have an even higher kinetic delay. Interestingly enough, we would expect the methanol oxidation peak to be unaffected as well, but this is not the case. As can be seen from Figure 7 and Figure 9, the methanol charge is noticeably higher for short hold times and low adsorption potentials. Figure 13 shows the first two cycles with a hold time of 20 ms and a preparation potential of 0.1 V. Although an insignificantly higher CO stripping charge may be observed during the first cycle, the excess charge in the methanol oxidation peak is far more than could possibly stem from the series pathway alone (the extra charge in the methanol oxidation, as compared to the second cycle, is found to be 30 $\mu C\ cm^{-2}$ while the extra CO stripping charge is only 7.8 $\mu C\ cm^{-2}$ in the same potential region). This excess charge in the methanol oxidation peak is not a unique finding for a 20 ms preparation step at 0.1 V, but is also found for various hold times at low potentials.

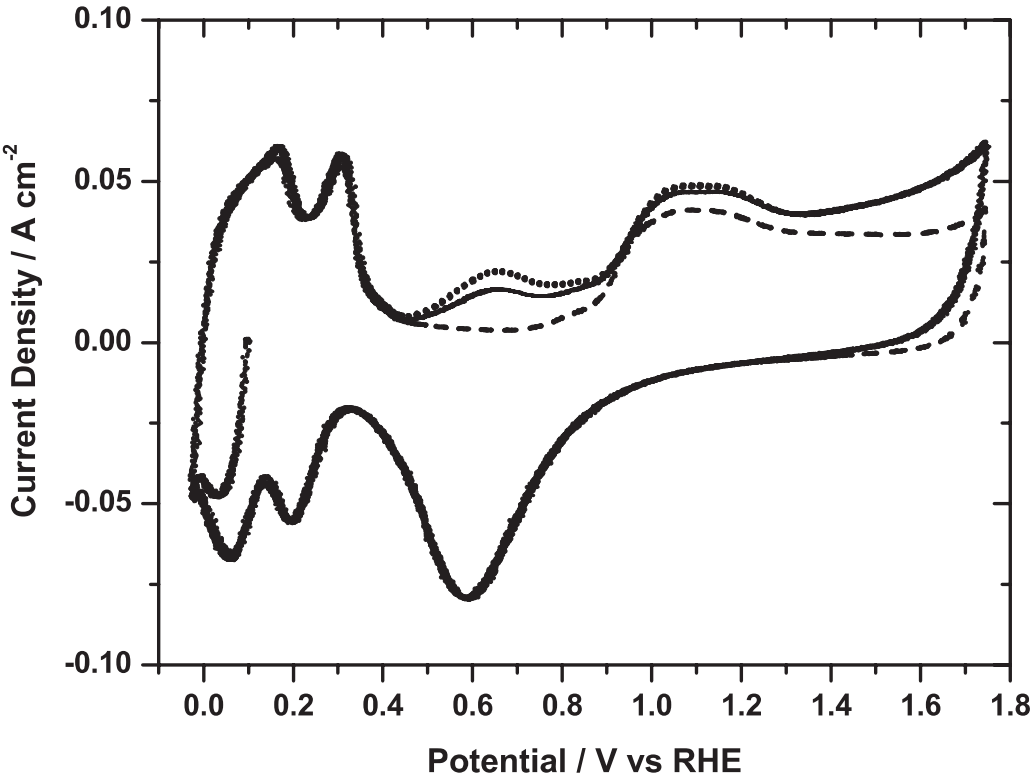

Figure 13 20 ms hold time at 0.1 V. The dashed line represents the first cycle without methanol present. The solid line represents the second cycle with methanol while the dotted line represents the first cycle with methanol present.

This proves that there exists a parallel pathway in methanol oxidation for low potentials and short times, under conditions where a kinetic delay of CO adsorption is observed. However, reaction leading to adsorbed CO will occur simultaneously and predominate as the preparation time or preparation potential increases.

2.4 Conclusions

Continuous cycling and potential sweep dependence of the first oxidation peak in the positive-going scan suggests the formation of CO_{ads} directly from methanol in solution as the main or perhaps only reaction in the potential region prior to platinum oxide formation.

We employed a combined chronoamperometry and fast potential sweep technique and quantitatively analyzed data, changing both the adsorption time and potential. The rate of formation of CO from methanol increased with potential at least until about 0.6 V. A potential-dependent kinetic delay was observed, which demonstrated the sluggishness of CO uptake from methanol at low potentials.

The saturation charge density of adsorbed CO from methanol, formic acid and dissolved CO, was measured as a function of preparation potential by measuring the CO-stripping charge in a fast potential sweep immediately after the adsorption step. The maximum saturation charge was found to be similar for formic acid and dissolved CO at potentials in the hydrogen upd region and corresponded to about 1 monolayer of linear bonded CO. The saturation charge of CO_{ads} derived from methanol is significantly lower than from formic acid or from dissolved CO, suggesting either a lower saturation coverage due to site requirements, or a mixture of linear, bridge and multiply-bonded CO leading to a lower number of electrons per surface site. The saturation charge was found to decrease at 0.35 V for formic acid, 0.6 V for methanol and 0.75 V for dissolved CO clearly demonstrating the significance of the parent molecule.

Indications of a parallel path at short times and low potentials were found by comparing the current in the methanol oxidation peak with the resulting CO stripping peak. Excess current was found that could not be entirely accounted for by the formation and subsequent oxidation of adsorbed CO. In this study we found that the parallel path is only active at short times and low potentials.

2.5 Acknowledgements

We thank the Norwegian University of Science and Technology, the University of Victoria and Science and Engineering Research Canada for financial support. F.S. thanks the Norwegian Research Council for the award of a scholarship.

References

[1] N.A. Hampson, M.J. Willars, B.D. McNicol, *J. Power Sources*, **4** (1979) 191

[2] B.D. McNicol, *J. Electroanal. Chem.*, **118** (1981) 71

[3] R. Parsons, T.J. VanderNoot, *J. Electroanal. Chem.*, **257** (1988) 9

[4] T.D. Jarvi, E.M. Stuve, in: *Electrocatalysis*, J. Lipkowski, P.N. Ross (Eds.), Wiley-VCH, New York, 1998, pp. 75-154

[5] S. Wasmus, A. Küver, *J. Electroanal. Chem.*, **461** (1999) 14

[6] J. Kua, W.A. Goddard, *J. Am. Chem. Soc.*, **121** (1999) 10928

[7] T. Iwasita, *Electrochim. Acta*, **47** (2002) 3663

[8] N.M. Markovic, P.N. Ross Jr., *Surf. Sci. Reports*, **45** (2002) 117

[9] W. Vielstich, in: *Encyclopedia of Electrochemistry*, A.J. Bard, M. Stratmann (Eds.), *Vol 2*, Wiley-VCH Verlag GmbH & Co, Weinheim, 2003, pp. 466-511

[10] a) E. Leiva, C. Sánchez, in: *Handbook of Fuel Cells - Fundamentals, Technology and Applications*, W. Vielstich, H.A. Gasteiger, A. Lamm (Eds.), *Vol 2 Electrocatalysis*, John Wiley & Sons, Chichester, 2003, pp. 47-61. b) C. Sánchez, E. Leiva, in: *Handbook of Fuel Cells - Fundamentals, Technology and Applications*, W. Vielstich, H.A. Gasteiger, A. Lamm (Eds.), *Vol 2 Electrocatalysis*, John Wiley & Sons, Chichester, 2003, pp. 93-131

[11] A. Capon, R. Parsons, *J. Electroanal. Chem.*, **44** (1973) 1

[12] Bagotzky, V. S., Vassiliev, YU. B., Khazova, O. A., *J. Electroanal. Chem.*, Vol. **81** (1977) 229

[13] M.I.S. Lopes, B. Beden, F. Hahn, J.M. Leger, C. Lamy, *J. Electroanal. Chem.*, **282** (1990) 287

[14] W. Vielstich, X.H. Xia, *J. Phys. Chem.*, **99** (1995) 10421

[15] K. Franaszczuk, E. Herrero, P. Zelenay, A. Wieckowski, J. Wang, R.I. Masel, *J. Phys. Chem.*, **96** (1992) 8509

[16] E. Herrero, K. Franaszczuk, A. Wieckowski, *J. Phys. Chem.*, **98** (1994) 5074

[17] C. Lamy, J.M. Leger, J. Clavilier, R. Parsons, *J. Electroanal. Chem.*, **150** (1983) 71

[18] J. Shin, C. Korzeniewski, *J. Phys. Chem.*, **99** (1995) 3419

[19] X.H. Xia, T. Iwasita, F. Ge, W. Vielstich, *Electrochim. Acta*, **41** (1996) 711

[20] J. Munk, P.A. Christensen, A. Hamnett, E. Skou, *J. Electroanal. Chem.*, **401** (1996) 215

[21] S.-G. Sun, in: *Electrocatalysis*, J. Lipkowski, P.N. Ross (Eds.), Wiley-VCH, New York, 1998, pp. 243-291

[22] Shimazu, K., Kita, H., *J. Electroanal. Chem.*, **341** (1992) 361

[23] T. Iwasita, X. Xia, *J. Electroanal. Chem.*, **411** (1996) 95

[24] Conway, B. E., Gottesfeld, S., *J. Chem. Soc. Faraday Trans. I*, **69** (1973) 1090

[25] Tilak, B. V., Conway, B. E., *J. Electroanal. Chem.*, **48** (1973) 1

[26] M.E. Van der Geest, M.J. Dangerfield, D.A. Harrington, *J. Electroanal. Chem.*, **420** (1997) 89

[27] G. Jerkiewicz, G. Vatankhah, J. Lessard, M.P. Soriaga, Y.-S. Park, *Electrochim. Acta*, **49** (2004) 1451

[28] Li, N.-H., Sun, S.-G., Chen, S.-P., *J. Electroanal. Chem.*, **430** (1997) 57

[29] Herrero, E., Chrzanowski, W., Wieckowski, A., *J. Phys. Chem.*, **99** (1995) 10423

[30] A.V. Tripkovic, K.D. Popovic, J.D. Momcilovic, D.M. Drazic, *J. Electroanal. Chem.*, **418** (1996) 9

[31] Jarvi, T. D., Sriramulu, S., Stuve, E. M., *J. Phys. Chem. B*, **101** (1997) 3649

[32] Sriramulu, S., Jarvi, T. D., Stuve, E. M., *Electrochim. Acta*, **44** (1998) 1127

[33] A.V. Tripkovic, K.D. Popovic, J.D. Momcilovic, D.M. Drazic, *J. Electroanal. Chem.*, **448** (1998) 173

[34] A.V. Tripkovic, K.D. Popovic, J.D. Momcilovic, D.M. Drazic, *Electrochim. Acta*, **44** (1998) 1135

[35] Sriramulu, S., Jarvi, T. D., Stuve, E. M., *J. Electroanal. Chem.*, **467** (1999) 132

[36] G.-Q. Lu, W. Chrzanowski, A. Wieckowski, *J. Phys. Chem. B*, **104** (2000) 5566

[37] Wang, H., Wingender, C., Baltruschat, H., Lopez, M., Reetz, M. T., *J. Electroanal. Chem.*, **509** (2001) 163

[38] D. Cao, G.Q. Lu, A. Wieckowski, S.A. Wasileski, M. Neurock, *J. Phys. Chem. B*, **109** (2005) 11622

[39] A. Papoutsis, J.M. Leger, C. Lamy, *J. Electroanal. Chem.*, **234** (1987) 315

[40] A. Papoutsis, J.M. Leger, C. Lamy, *J. Electroanal. Chem.*, **359** (1993) 141

[41] A. Wieckowski, W. Chrzanowksi, E. Herrero, in: *New Materials for Fuel Cell Systems*, O. Savadogo, P.R. Roberge, T.N. Veziroglu (Eds.), Editions de l`Ecole Polytechnique de Montréal, Montreal, 1995, pp. 326-336

[42] D. Pletcher, V. Solis, *Electrochim. Acta*, **27** (1982) 775

[43] Iwasita, T., Xia, X. H., Liess, H. D., Vielstich, W., *J. Phys. Chem. B*, **101** (1997) 7542

[44] J.M. Orts, A. Fernandezvega, J.M. Feliu, A. Aldaz, J. Clavilier, *J. Electroanal. Chem.*, **327** (1992) 261

[45] D.V. Heyd, D.A. Harrington, *J. Electroanal. Chem.*, **335** (1992) 19

[46] B. Beden, A. Bewick, C. Lamy, *J. Electroanal. Chem.*, **148** (1983) 147

[47] B. Beden, C. Lamy, A. Bewick, K. Kunimatsu, *J. Electroanal. Chem.*, **121** (1981) 343

[48] T. Solomun, *Surf. Sci.*, **176** (1986) 593

[49] B. Beden, A. Bewick, M. Razaq, J. Weber, *J. Electroanal. Chem.*, **139** (1982) 203

[50] B. Beden, A. Bewick, K. Kunimatsu, C. Lamy, *J. Electroanal. Chem.*, **142** (1982) 345

[51] J. Clavilier, R. Parsons, R. Durand, C. Lamy, J.M. Leger, *J. Electroanal. Chem.*, **124** (1981) 321

[52] S. Gilman, *J. Phys. Chem.*, **66** (1962) 2657

[53] A. López-Cudero, A. Cuesta, C. Gutiérrez, *J. Electroanal. Chem.*, **579** (2005) 1

[54] H.A. Gasteiger, N. Markovic, P.N. Ross, E.J. Cairns, *J. Phys. Chem.*, **98** (1994) 617

[55] H. Kita, K. Shimazu, K. Kunimatsu, *J. Electroanal. Chem.*, **241** (1988) 163

[56] A. Hamnett, in: *Interfacial Electrochemistry. Theory, Experimental and Applications*, A. Wieckowski (Ed.), Marcel Dekker Inc., New York, 1999, pp. 843

[57] S.G. Sun, J. Clavilier, *J. Electroanal. Chem.*, **236** (1987) 95

[58] G.-Q. Lu, A. Crown, A. Wieckowski, *J. Phys. Chem. B*, **103** (1999) 9700

[59] S.-G. Sun, Y. Lin, N.-H. Li, H.-Q. Mu, *J. Electroanal. Chem.*, **379** (1994) 273

Chapter 3

Impedance Study of Methanol Oxidation on Platinum Electrodes

Frode Seland[a,b] Reidar Tunold[a] and David A. Harrington[b,*]

[a] *Electrochemistry Group, Department of Materials Science and Engineering, Norwegian University of Science and Technology, NO-7491 Trondheim, Norway.*

[b] *Department of Chemistry, University of Victoria, Victoria, British Columbia, V8W 3V6, Canada.*

Abstract

Methanol oxidation on Pt electrodes is studied by a.c. voltammetry. Data from voltammograms at frequencies from 0.5 Hz - 20 kHz are assembled into electrochemical impedance spectra and analyzed using equivalent circuits. Inductive behaviour and negative relaxation times are attributed to nucleation and growth behaviour. The rate-determining step is proposed to be the reaction of adsorbed CO and OH at the edge of islands of OH, with competition between OH and CO adsorption for the released reaction sites.

Key words: Impedance, Methanol Oxidation, Platinum, A.c. Voltammetry, Nucleation and growth

* Corresponding author. Tel.: +1-250-7217166; Fax: +1-250-7217147
Email addresses: frodesel@material.ntnu.no (Frode Seland), Reidar.Tunold@material.ntnu.no (Reidar Tunold), dharr@uvic.ca (David A. Harrington).

3.1 Introduction

The mechanism of methanol oxidation on Pt electrodes has been widely studied, particularly in comparison with more active catalysts such as Pt-Ru, and brief recent reviews are available, e.g., [1-5]. Much progress has been made recently, especially in identifying the adsorbed intermediates present on the surface by in-situ spectroscopies such as FTIR. There is now general agreement that the principal carbonaceous species on the surface is adsorbed CO. The kinetics of the process have also been studied by a variety of electrode kinetic experiments, but some issues remain unresolved. There have been suggestions that a parallel pathway, not involving adsorbed CO as an intermediate can occur [6-19]. The question about whether oxidation of adsorbed CO occurs via a nucleation-growth-collision (NGC) or a Langmuir-Hinshelwood (LH) mechanism is a current issue, e.g., [20], that also impacts on methanol oxidation kinetics.

Electrochemical impedance spectroscopy (EIS) is a powerful method for studying reaction mechanisms, but there are only a few EIS studies on methanol oxidation. Some of these are on real fuel cells [21-24] using commercial catalysts and/or two-electrode systems; these papers are not focused on mechanistic issues. Lee et al. [25] used EIS to show that a Hopf bifurcation exists for this system and can be correlated with the presence of galvanostatic oscillations, but the spectra were not interpreted mechanistically. Yu et al. [26], working on a platinized electrode in alkaline solution, proposed an equivalent circuit and measured the charge-transfer resistance as a function of temperature, and Azevedo et al. [27] compared the charge-transfer resistance of Pt and Pt/Ru catalysts; neither groups interpreted the detailed shapes of the more complicated spectra in mechanistic terms. The best works, from a mechanistic point of view, are those of Melnick et al. [28], Hsing et al. [29] and Otomo et al. [30], who systematically measured impedance spectra at different steady-state potentials, and interpreted the data in terms of single-adsorbate or two-adsorbate models. Melnick et al. also studied the slow time dependence of the impedance [31].

We here apply an EIS analysis of impedance data for methanol oxidation on polycrystalline Pt collected during slow-scan a.c. voltammetry. The use of cycling means that the slow time effect that occurs in steady state impedance measurements is to a large extent avoided. We are also able to correlate directly the impedance features with the d.c. voltammetry. Furthermore, this methodology enables the impedance to be obtained "on the fly" so that nonsteady-state conditions such as partially-covered surfaces can be studied. Collection of a.c. data in the conventional way, after waiting for the system to

settle at constant potential, is unsuitable for processes in which an irreversible adsorption process leads ultimately to a full-coverage state. This method has been shown theoretically to give valid results provided that the frequency is not too low [32], and we have used it previously to study the growth of the oxide film on Pt [33].

An equivalent circuit and mechanistic analysis is applied here to the data to show that impedance features can be well correlated to the voltammetry features. In the kinetic model, the surface is always fully covered by CO and an oxygen-containing adsorbate, whose coverage uniquely specifies the surface condition, allowing a single-adsorbed species model to be used. Dissociated water and Pt oxide are assumed to be the oxygen donors in distinct potential regions. The signs of the circuit elements can be related to the signs of the kinetic parameters. Regions of NGC behaviour are identified and correlated with rising currents in sweep reversal and sweep-hold experiments.

3.2 Experimental

Polycrystalline platinum wire (Johnson-Matthey 99.998%) was sealed in glass and used as the working electrode in a glass cell of conventional design. Potentials were measured and are quoted against a hydrogen reference electrode in the same solution (RHE). Current densities are reported relative to the true surface area, calculated by assuming that the area under the underpotentially-deposited hydrogen cyclic voltammetry peaks corresponded to 220 $\mu C\ cm^{-2}$. The electrodes and cell were cleaned in warm chromic acid for at least three hours and then thoroughly rinsed several times in Milli-Q water. Sulphuric acid (Anachemia/Seastar for a.c. experiments, Fluka for d.c. experiments) was made up in Milli-Q water and purged with Ar for at least 30 minutes before adding the methanol (Acros residue-free electronic grade). Ar was bubbled through the solution throughout the experiments. Unless otherwise specified, all experiments were carried out in 0.25 M CH_3OH, 0.5 M H_2SO_4 at a sweep rate of 5 $mV\ s^{-1}$.

The Pt electrode was cycled for 2 h in sulphuric acid prior to all methanol experiments, and for a further 2 h after methanol was added before experiments were done. Currents slowly decreased indicating some degradation in the electrode activity over the time period of many hours required for these slow-sweep experiments. For the d.c. reversal and hold experiments, the measured currents were normalized to a reference curve to correct for this degradation. This correction amounted to no more than 10%. For the a.c. voltammograms,

several sets of data were collected, and all showed similar behaviour. The data analyzed quantitatively in the equivalent circuit analysis came from a single set of a.c. voltammograms collected over a nine-hour period in which the degradation amounted to less than 10%, as judged by the decrease in the charge of the methanol oxidation peak (forward scan).

A.c. voltammograms were recorded at 5 mV s^{-1} with an applied sinusoidal signal of 0.75 mV rms using a sweep generator, a custom-built potentiostat, and two Ametek Signal Recovery 7265 dual phase lock-in amplifiers (LIA). The use of the very small amplitude signal means that behaviour occurring over small potential regions can be examined in the linear regime; changes in qualitative behaviour over regions of tens of millivolts in the voltammograms were found in the present study. The a.c. current (both in-phase and quadrature components) was measured differentially across a 100 Ω resistor in the counter-electrode circuit to eliminate possible phase shifts in the potentiostat's current-to-voltage converter. The phase and amplitude shifts introduced by the potentiostatic control loop were corrected for by simultaneously measuring the a.c. potential applied to the cell with the second LIA, and the impedance was calculated by dividing the complex number for potential by the complex number for current density in the usual way. A mixed filtering strategy was used [32]: analog filtering using the time constant settings on the LIAs was used to a minimum extent (5 s for $f < 1$ Hz, 1 s for f up to 20 Hz; 0.1 s for higher frequencies) and FFT-based smoothing was then used after data collection. Some earlier data sets were collected at 5 mV rms amplitude sweeping at 10 mV s^{-1}, using a Stanford Research 530 LIA.

A.c. voltammograms were collected for frequencies from ca 0.1 Hz to 20 kHz, one frequency per cycle. Custom software then collected the data from all frequencies at a given potential, interpolating between potentials if necessary. In this way a single EIS spectrum at a given potential is obtained, comprised of one data point from each a.c. voltammetry cycle. Such spectra were generated for every 2 mV around the voltammogram. It is evident that valid measurements cannot be made at too low frequencies since the sweep slowly changes the system; frequencies need to be significantly greater than $F\nu/2\pi RT = 0.03$ Hz at 5 mV s^{-1} [32]. The 0.1-0.3 Hz data points in the spectra showed significant variability and so were not fitted; this may be an indication that the frequency condition is borderline for these points.

EIS spectra were fitted to equivalent circuits using ZSimpWin [34] with modulus weighting. Elements were added to the equivalent circuits only when warranted by the F-ratio test for adding a parameter [35]. For example, the

double-layer was better modelled as a constant-phase element (CPE, admittance $Q(\mathrm{i}\omega)^{\alpha}$) than as a capacitor: at 0.75 V scanning up, the fit to 5 parameters (inductive circuit L with capacitor for the double-layer, $\chi^2(5) = 9.7\times10^{-2}$, $N = 25$ frequencies) improves going to 6 parameters (inductive circuit with CPE for the double-layer, $\chi^2(6) = 2.5\times10^{-2}$). The *F*-ratio with *a* and 2*N*-*n* degrees of freedom for adding *a* parameters to give *n* parameters in the new circuit is

$$F(a, 2N-n) = \frac{\left(\chi^2(n-1) - \chi^2(n)\right)/a}{\chi^2(n)/(2N-n)} \quad (1)$$

Here we have $a = 1$, $n = 6$ and find $F = 127$, which has a probability of being exceeded by chance of much less than 1%, the level that we chose for acceptance. The CPE exponent α was in the range 0.83-0.98, similar values to those found in our earlier study of Pt oxide [33]. About 4400 equivalent circuit/spectrum combinations were fitted in the course of this study.

3.3 Results

3.3.1 D.c. voltammetry

The characteristic potential regions for methanol oxidation in relationship to the behaviour in H_2SO_4 alone are discussed in reference to the d.c. voltammograms in Figure 1.

As is well known, the hydrogen underpotential deposition (UPD) peaks at 0-0.3 V in base electrolyte are suppressed in the presence of methanol, due to the adsorption of the CO intermediate. The initial current for methanol oxidation current on the forward (positive-going) sweep begins at around 0.5 V in a region where the blank shows no electroactivity, and it is therefore usually assumed that the oxygen source in this region is adsorbed or dissociated water. At low concentrations, the main methanol oxidation peak occurs at 0.7 V. There is a shoulder on the positive-potential side of this peak at ca. 0.85 V, a potential where Pt initially forms an oxide film, and so the oxygen source here is assumed to be the oxide. Since oxidation of carbon monoxide occurs here, the process here is usually taken to be the oxidation of adsorbed CO to give CO_2. At higher methanol concentrations, this second peak predominates and the first peak appears now only as a shoulder. The decrease in oxidation current after 0.85 V corresponds to the presence of more surface oxidation, i.e., a more

extensive surface oxide film inhibits the methanol oxidation. However, at the most positive potentials methanol oxidation increases again, suggesting a change in mechanism, perhaps due to a change in the oxide structure.

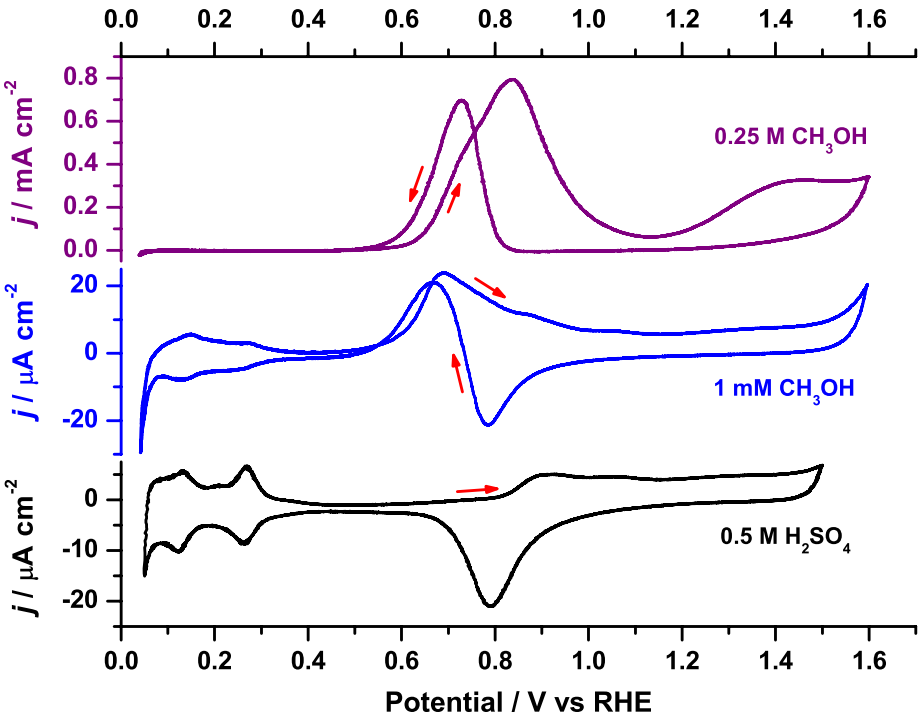

Figure 1 D.c. voltammograms for methanol oxidation at Pt, 5 mV s^{-1}. (a) 0.25 M methanol in 0.5 M H_2SO_4 (b) 1 mM methanol in 0.5 M H_2SO_4 (c) baseline behaviour in 0.5 M H_2SO_4 without methanol.

On the reverse sweep the current initially remains anodic but decreases. Once the potential reaches the region where the oxide is reduced, the electrode is reactivated for methanol oxidation and the current increases. This is seen most clearly in the 1 mM curve, where the curve follows the baseline curve well into the oxide reduction peak before the oxidation current takes over; at higher concentration the oxidation current takes place at about the same potential. The resulting oxidation peak corresponds to the first peak in the forward sweep though it is displaced slightly to negative potentials.

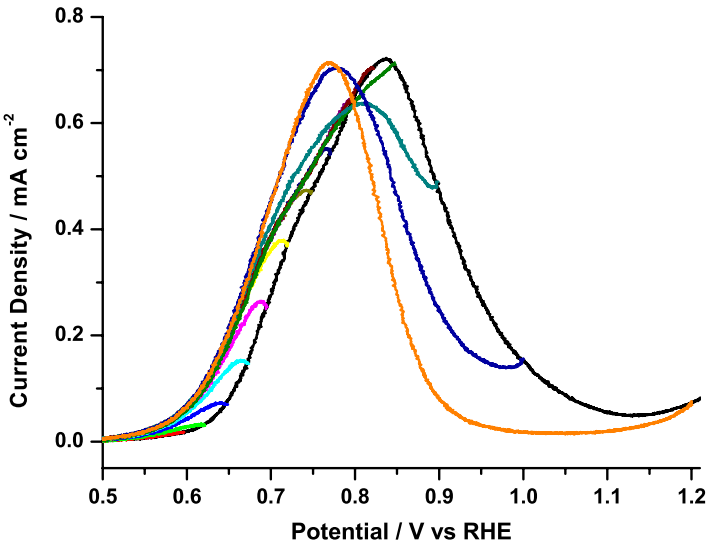

Figure 2 Voltammetry varying upper limit sweep reversal potentials. 0.25 M CH_3OH, 0.5 M H_2SO_4, 5 mV s^{-1}.

Cyclic voltammograms with varying upper-limit reversal potentials (Figure 2) show an increasing current after reversal at potentials in the early stages of the oxidation peak. This is typically taken as a signal for NGC behaviour. Later in the rising part of the peak, the current does not rise significantly, indicating that either island growth has slowed, or that sufficient island collisions have occurred that the total island perimeter is no longer increasing. The larger increasing currents after reversal on the downward sweep do not occur immediately after reversal, and so do not definitively indicate NGC. These rising currents occur after the opportunity for significant coverage change and likely indicate reactivation of the surface after oxide has been reduced. Another signal for NGC behaviour is that the current increases after holding the potential, and this is observed in the rising part of the peak, predominantly in the early stages (Figure 3).

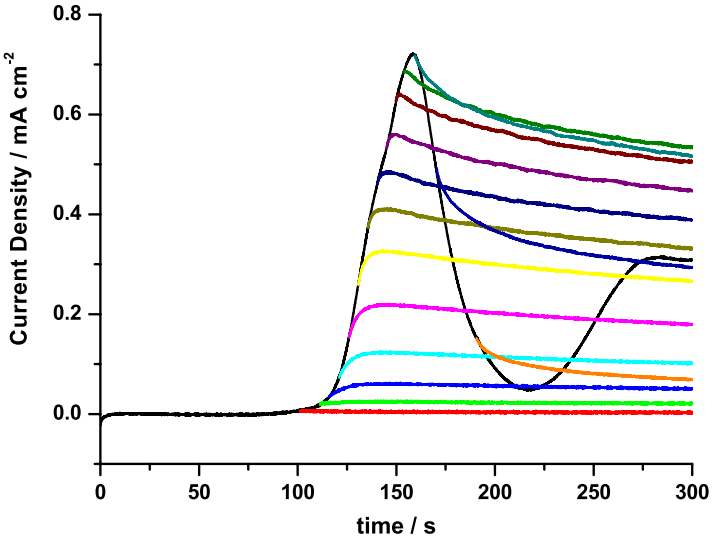

Figure 3 Sweep-hold experiments. Potential is swept up to the selected potential at 5 mV s^{-1} and then held. Time is measured from the beginning of the sweep at 0.04 V.

3.3.2 A.c. voltammetry

Some of the a.c. voltammograms that formed the basis for the impedance spectra are shown in Figure 4 and Figure 5.

Some correlation with the d.c. voltammogram is already apparent. For example, the imaginary part of the admittance at higher frequencies (Figure 4) is largely a measure of the double-layer capacitance, and the higher values above about 0.75 V are where Pt oxide forms (compare blank voltammogram in Figure 1), suggesting that the oxide-covered surface has a higher double-layer capacitance. At the lowest frequencies, the points where the admittance components both become very small are points of high impedance and are expected to correlate with points of zero slope in the voltammogram. For example, both components at 0.5 Hz cross zero on the forward sweep near 0.83 V (Figure 5), which is the location of the d.c. voltammetry peak. Interestingly, the return sweep values also go through zero at this point, even though the d.c. current does not peak there. Also on the low-frequency voltammograms, we see that the real-part of the admittance becomes negative on the forward sweep where the current is decreasing; this corresponds to the impedance moving into the second quadrant and requires an equivalent circuit with a negative resistor.

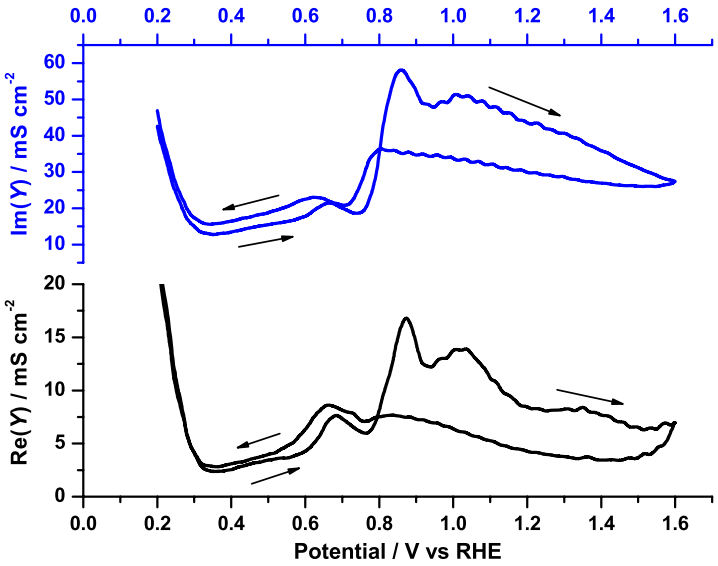

Figure 4 A.c. voltammograms at 100 Hz, 5 mV s^{-1}.

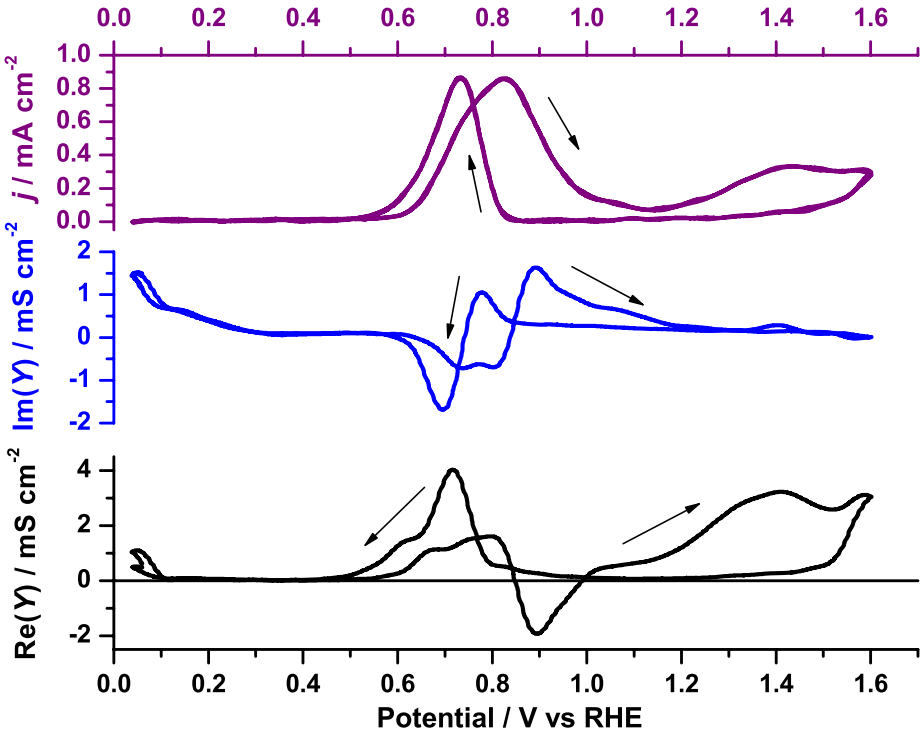

Figure 5 Comparison of a.c. voltammograms at 0.5 Hz with d.c. voltammogram, all at 5 mV s^{-1}. (a) d.c. voltammogram, (b) Imaginary part of admittance, (c) real part of admittance.

It is clear that the forward and reverse scans are different and it is to be emphasized that the impedance spectra we obtain are not for the steady-state condition, but for the condition that applies during the slow sweep. Since the surface condition at a given potential does depend on sweep rate, the impedance will also be a function of sweep rate. In this respect, the real part of the admittance on the return sweep is interesting: at 5 mV s^{-1} it does not go negative at frequencies measurable in our experiment (Figure 5), but at 10 mV s^{-1} it does (Figure 6). In the latter case, the negative region is just after removal of the oxide, as measured by the changing double-layer capacitance (high-frequency imaginary part of the admittance). In the slower sweep measurement, the oxide removal occurs in a narrow potential range, but in the faster sweep-rate experiment, the negative region can be captured because the oxide removal is spread out in potential. In both cases, after extrapolation to zero frequency the real part of the admittance is negative.

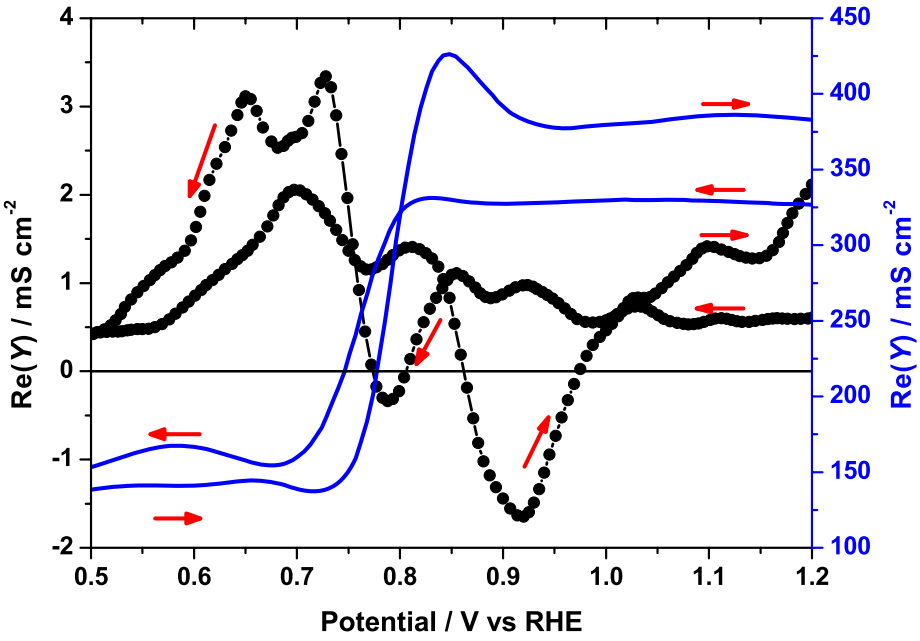

Figure 6 A.c. voltammograms at 10 mV s^{-1}. Real part of admittance at 1 Hz (circles, left axis) and 1 kHz (line, right axis).

3.3.3 EIS spectra

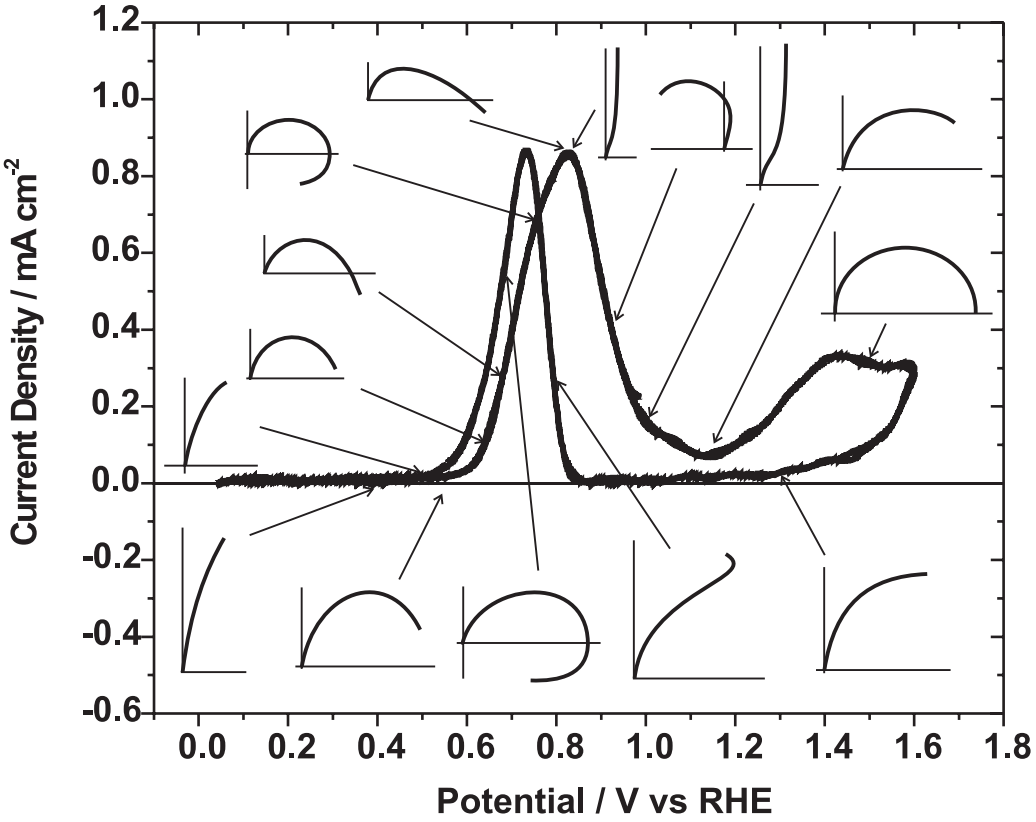

Figure 7 Summary of the EIS behaviours found. Insets are Nyquist diagrams of the impedance at selected points around the d.c. voltammogram.

The EIS spectra showed the qualitative features of Figure 7. These were analyzed using the equivalent circuits of Figure 8. The element values for these circuits were converted to parameters relevant in the kinetic theory for mechanisms with a single adsorbed species [36]:

$$R_{\mathrm{ct}}^{-1} = F\left(\frac{\partial r_{\mathrm{e}}}{\partial E}\right)_{\theta} \tag{2}$$

$$B = \frac{1}{L} = -\frac{1}{C_2 R_{\mathrm{ct}}^2} = \frac{F}{\Gamma_{\mathrm{m}}}\left(\frac{\partial r_{\mathrm{e}}}{\partial \theta}\right)_{E}\left(\frac{\partial r_{\theta}}{\partial E}\right)_{\theta} \tag{3}$$

$$\tau^{-1} = \frac{R_{\mathrm{ct}} + R_2}{C_2 R_{\mathrm{ct}} R_2} = \frac{R_0}{L} = -\frac{1}{\Gamma_{\mathrm{m}}}\left(\frac{\partial r_{\theta}}{\partial \theta}\right)_{E} \tag{4}$$

The circuits chosen in the different potential regions and the signs of the parameters are summarized in Table 1. Circuits C and L are interchangeable for ideal data, provided that the signs of the elements are not constrained to always be positive, but for real data one or the other circuit gives better fits. In cases where good fits were obtained with either circuit, we preferred the inductive circuit because the value of the inductor is more simply related to the kinetic parameters in the single-adsorbed species theory. This choice also led to CPE exponent α values more consistent across potential regions.

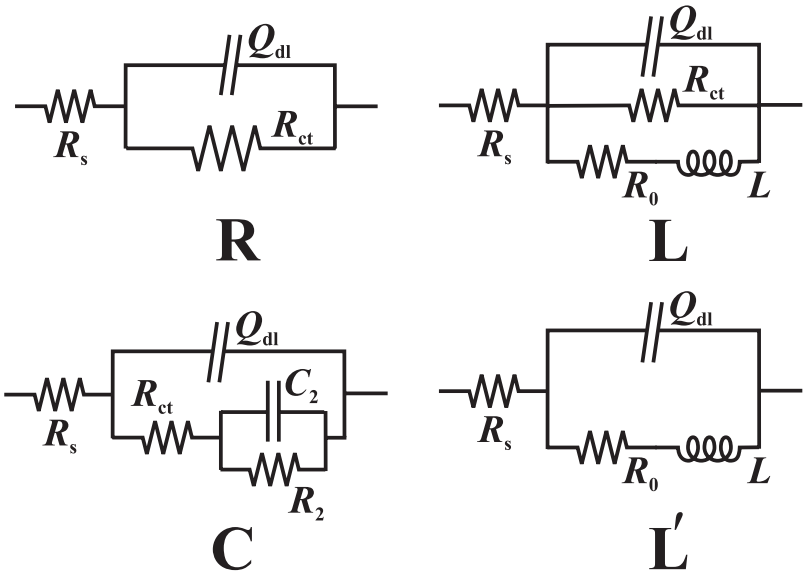

Figure 8 Equivalent circuits used in this work. Q_{dl} is a CPE representing the double-layer.

Charge-transfer and double-layer parameters

Although various spectral shapes were fitted with different circuits in different potential regions, the charge-transfer resistances extracted from these circuits merged seamlessly into a single curve, Figure 9. Nice Tafel behaviour was observed over 1.5 decades in R_{ct} between 0.50 V to 0.66 V on the forward (positive-going) sweep, with a Tafel slope of 110 ± 2 mV dec^{-1} ($\alpha = 0.53$, T = 23 °C). The negative-going sweep showed a similar Tafel region in the positive-slope region of the oxidation peak with the same Tafel slope, 111 ± 2 mV dec^{-1}. This region (0.6 V - 0.4 V) was displaced negatively (corresponding with the negative shift in the voltammetry peak) due to hysteresis in the oxide formation and reduction.

The double-layer capacitance is extracted from the CPE parameters as $\left(QR^{1-\alpha}\right)^{1/\alpha}$, where R is the parallel combination of R_s and R_{ct} [37]. However, $R_s \ll R_{ct}$, and we approximated R as R_s in this calculation Figure 10. The capacitance shows higher values in the oxide region. The values for the oxide-covered surface in the negative-going sweep are the same as found previously in the blank solution [33], but for the forward sweep the values appear to be significantly higher. This observation appears to parallel the observation in d.c. voltammetry that the current in the oxide region is higher than in blank solution on the forward sweep, but similar to blank solution on the reverse sweep.

Table 1 Summary of fitting results.

Potential Region	Circuit	Sign of R_0	Sign of B or L	Sign of τ	Sign of R_p
0.400-0.638 pos [1]	R	n/a	n/a	n/a	+
0.640-0.660 pos	L	+	+	+	+
0.662-0.700 pos	L	-	+	-	mixed
0.702-0.816 pos	L	+	+	+	+
0.818-0.848 pos	L	-	+	-	mixed
0.850-0.996 pos	L' [2]	-	-	+	-
0.998-1.500 pos	R	n/a	n/a	n/a	+
0.826-1.500 neg	R	n/a	n/a	n/a	+
0.786-0.824 neg	L	-	-	+	mixed
0.750-0.784 neg	L	+	-	-	+
0.720-0.748 neg	R [3]	n/a	n/a	n/a	+
0.652-0.718 neg	L	+	+	+	+
0.602-0.650 neg	L	-	+	-	mixed
0.596-0.600 neg	L	+	+	+	+
0.400-0.594 neg	R	n/a	n/a	n/a	+

1. 0.3-0.4 V showed only $Q_{dl} + R_s$, except that circuit C without R_2 sometimes fit better

2. Circuit C with R_{ct} removed and negative R_2 also fit well here.

3. Low frequency points too scattered for fitting a more complex circuit.

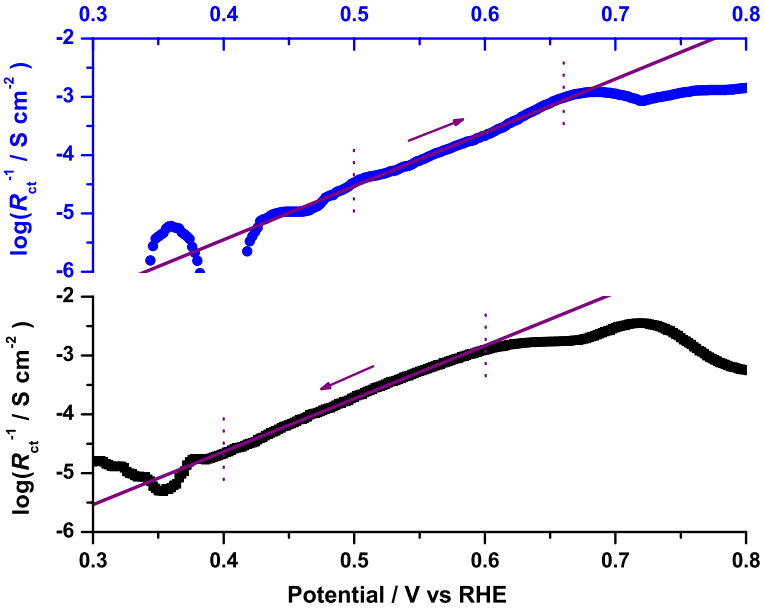

Figure 9 Tafel plots of R_{ct} for forward and reverse sweeps. Fitted regions and regression lines are shown.

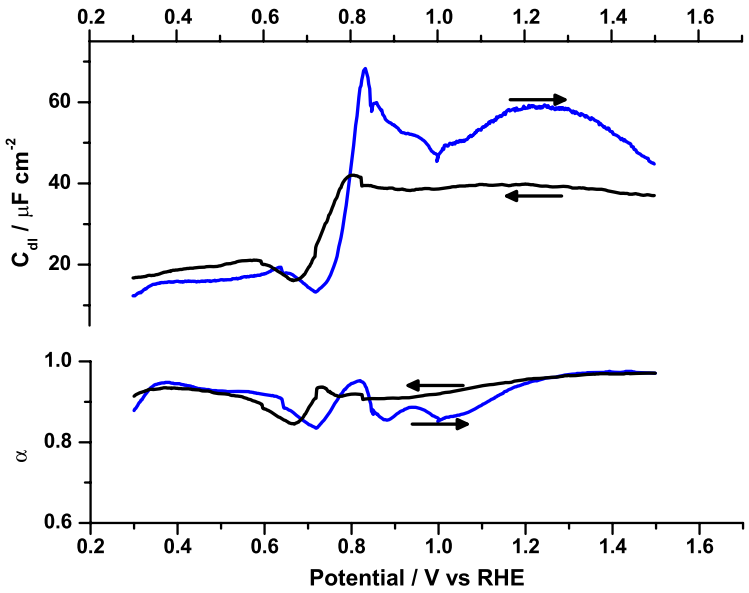

Figure 10 Double-layer capacitance and CPE exponent α from fits to all circuits in forward and reverse sweeps.

In the region where the d.c. current leaves the baseline on the forward sweep, we observed an interesting dip in the phase that we attributed to a double-layer effect. For example, at 0.57 V (Figure 11) the phase is not flat at the CPE value, but dips around 200 Hz. This feature can be fit better by the two-semicircle circuit C rather than the single-semicircle circuit R (F-test probability < 0.1% at 0.57 V), though visually two semicircles could not be distinguished. The capacitance in circuit C seems rather small (9 μF cm^{-2} at 0.57 V), suggesting it is more likely associated with a double-layer process than an adsorption relaxation, and it is possible that this capacitance is combining with the CPE to give a better fit of the phase of the double-layer in this region. Although not favoured by the statistical test, similar qualitative behaviour was observed in the downward sweep in a similar potential range, suggesting that this feature may be real. It defines a high-frequency relaxation with a resistance of several hundred Ω cm^2, which decreases with potential until somewhere in the inductive region, at which point it is undetectable. Rather than over-interpret such a small feature, which is probably related to the double-layer rather than to kinetics, we extracted R_{ct} in this region from the single-relaxation circuit R.

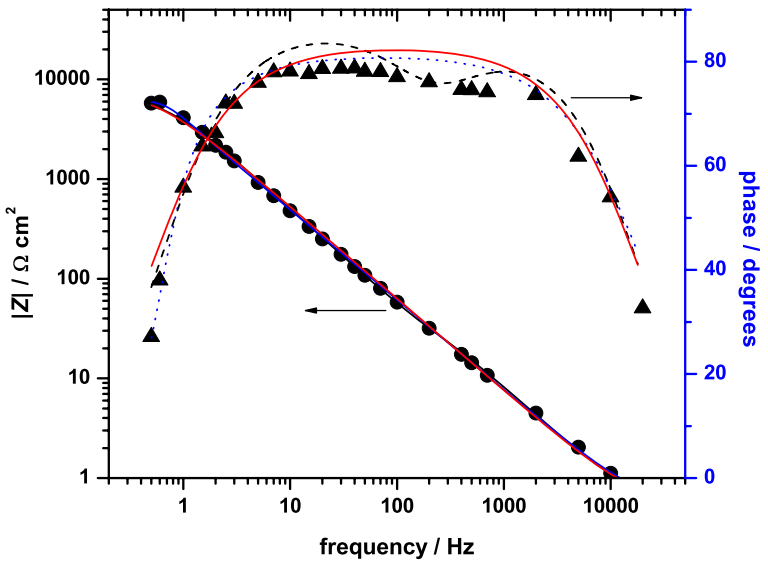

Figure 11 Bode plot at 0.570 V on positive-going sweep, showing the change in phase at about 200 Hz. Fits are shown for circuits R (solid line), C (dashed line) and L (dotted line). Fits to magnitude are closely overlapping on this scale.

Forward sweep

Nyquist plots of selected spectra for the forward sweep are shown in Figure 12.

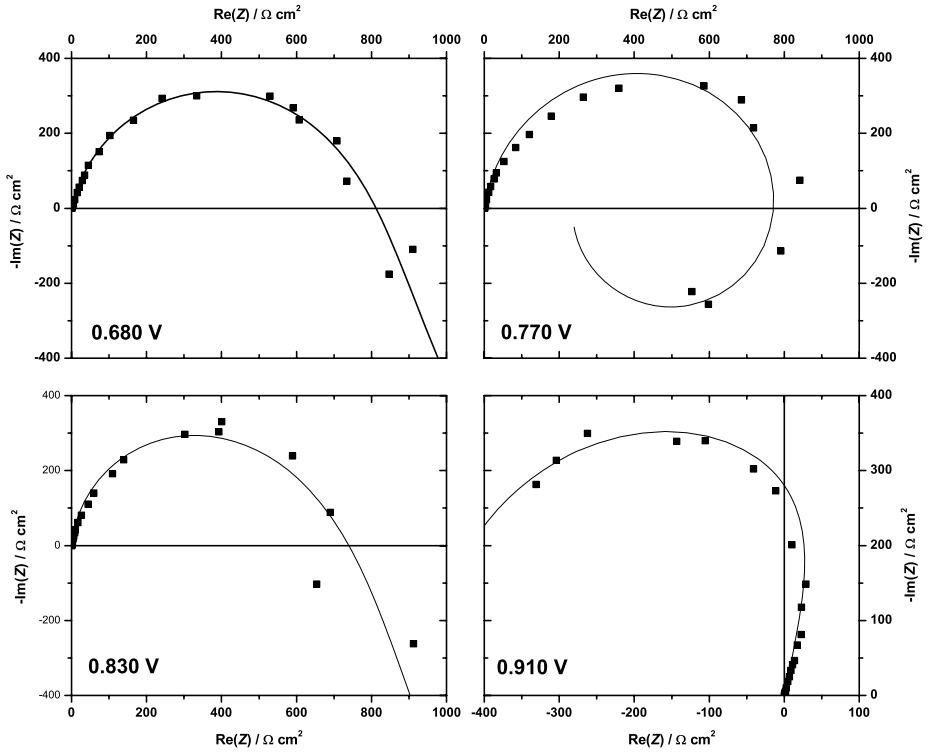

Figure 12 Selected spectra for the forward sweep. Lines are the fits to the selected equivalent circuits (specified in Table 1).

The first reliable evidence of charge transfer occurs around 0.47 V where the d.c. voltammogram current leaves the baseline. The curvature in the impedance plot shows that the spectra are the beginning of a semicircle, which develops until the lowest frequency points cross the axis into the fourth quadrant (Im(Z) > 0) at about 0.65 V. By 0.64 V, the inductive circuit is preferred and L and R_0 are determined with an error of about 50%. The derived parameters $B = 1/L$ and $\tau^{-1} = R_0/L$ are shown in Figure 13. The circuit L with a positive inductor applies nearly up until the voltammetry peak, but R_0 and hence τ becomes negative over narrow regions (0.66-0.70 V and 0.818-0.848 V). In the early part of the latter region, R_0 and the inverse time constant become more negative, but later the errors increase and preclude us from deciding where the time constant

goes to at the peak. The low frequency impedance moves from the fourth quadrant up into the first quadrant and becomes almost vertical near the voltammetry peak.

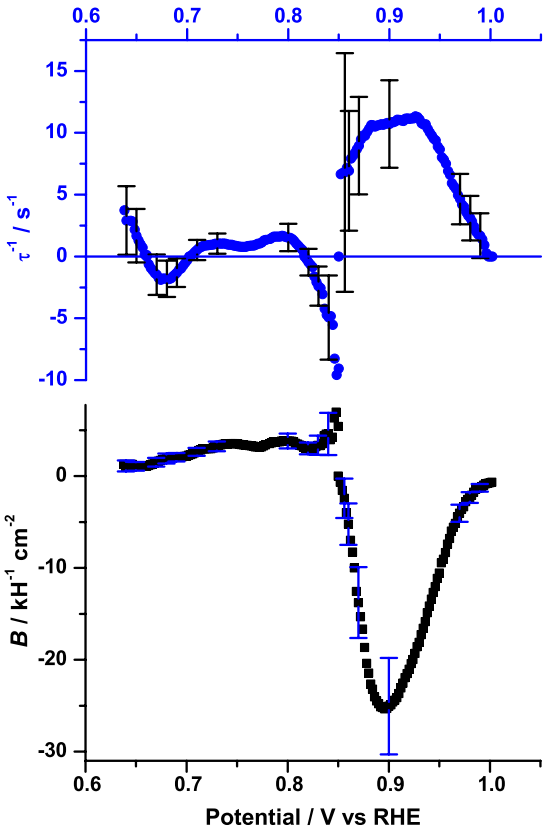

Figure 13 Parameters B and τ for the forward sweep. Extracted from the equivalent circuits specified in Table 1, using equations (3) and (4).

The low frequency behaviour at, and slightly past, the voltammetry peak (0.83-0.85 V) is scattered, but the tendency is up and back, eventually entering the second quadrant in the Nyquist plot. The errors are large here, because we are taking the reciprocal of small numbers crossing through zero, and a slight change in the zero-crossing point on the a.c. voltammograms at different frequencies is magnified. In fact, at 0.848 V, where the transition occurs, some of the low-frequency points are tending into the second quadrant while others, collected later in time, are in the first quadrant. Nonetheless, this time-dependent behaviour of a transition from second quadrant to first quadrant behaviour was seen before [31]. At higher potentials, the second quadrant behaviour appears as a single semicircle whose shape is distorted at high

frequencies by the requirement of the CPE to have a positive slope. The obvious circuit to fit here is circuit R with a negative resistor. However, fits were dramatically better for circuit L' with a negative inductor. Note that R_{ct} is absent here; its presence made the fits worse. The values of R_0 and L show a maximum at 0.894 V, approximately at the inflection point on the descending part of the voltammetry peak, but $\tau^{-1} = R_0/L$ peaks later.

The second quadrant behaviour persists to near 1.00 V, where the resistance R_0 has become large enough that the spectra appear again as a near vertical line. Then the impedance is back in the first quadrant, as part of a semicircle that develops to a full semicircle for the last part of the sweep. In this region, the fitting gives no evidence for additional parameters beyond those of the single-semicircle circuit R. The parameter R_{ct}^{-1} shows a shoulder around 1.1 V and then peaks at 1.4 V, close to the second peak in the voltammogram (see Figure 16; $R_p = R_{ct}$ in this region). Past the peak, it changes by only 25%, and appears to track the voltammogram peak shape.

Reverse sweep

Nyquist plots of selected spectra in the reverse sweep are shown in Figure 14.

After reversal, the impedance continues to show a single semicircle, but by 1.2 V only a small fraction of it is observed. As the d.c. voltammogram current rises, circuit L gives better fits, initially with both R_0 and L negative. Unlike for the forward sweep, the R_{ct} value could be determined in this region. The fits show that the apparent scatter of the lowest few frequency points is the beginning of the Nyquist plot bending back toward the second quadrant (Figure 14, 0.800 V). The parameters B and τ^{-1} (Figure 15) are reliably measured and change systematically in this region. The calculated resistance at zero frequency (Figure 16) indicates that the impedance extrapolates into the second quadrant even though none of the data points are in the second quadrant at this sweep rate. At the faster sweep rate of 10 mV s^{-1}, data points at measurable frequencies did enter the second quadrant (negative real admittances in Figure 6).

Circuit L with various sign patterns continues to fit the data down to 0.596 V except for a brief region where the low frequency points are too scattered for fitting. More negative than 0.596 V, there is no further evidence for adsorption.

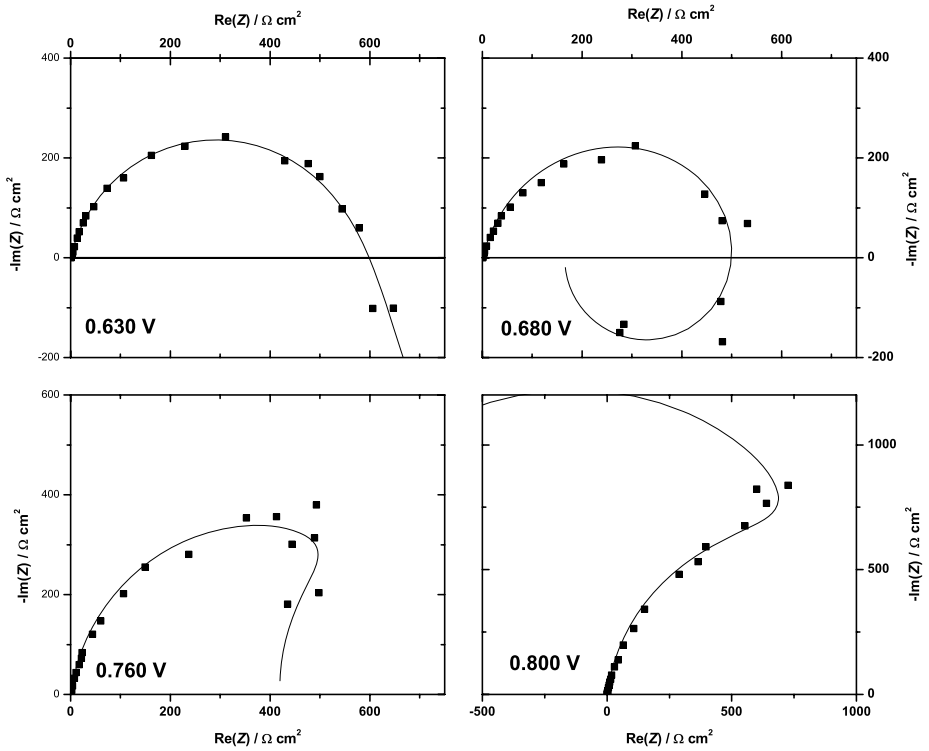

Figure 14 Selected spectra for the reverse sweep. Lines are the fits to the selected equivalent circuits (specified in Table 1).

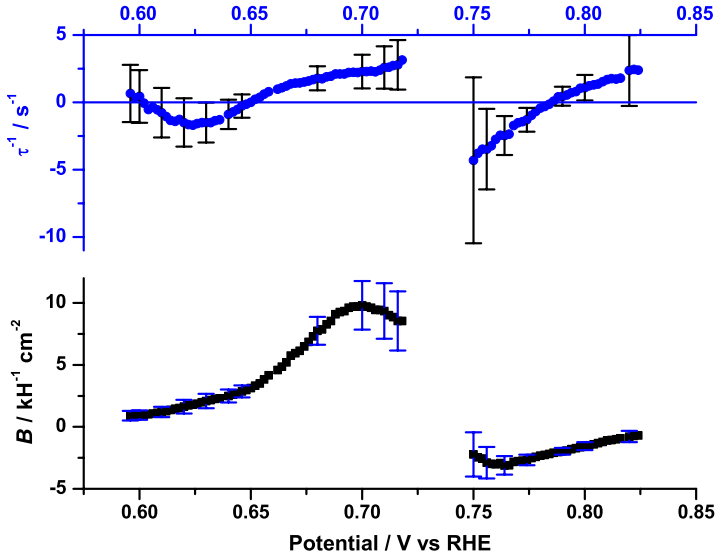

Figure 15 Parameters B and τ for the reverse sweep. Extracted from the equivalent circuits specified in Table 1, using equations (3) and (4).

Zero-frequency limit

To decide whether or not features of the EIS spectra are missing because we cannot measure at lower frequencies, we used the fitted equivalent circuit parameters to determine the impedance at zero frequency. For equivalent circuits that have a d.c. current path, the impedance at zero frequency is real and equal to the inverse of the slope of the (quasi) steady-state polarization curve [38,39]:

$$R_p^{-1} = \left(\lim_{\omega \to 0} Z\right)^{-1} = \frac{dj_{ss}}{dE} \tag{5}$$

For circuits with blocking behaviour at d.c., the impedance tends to infinity at zero frequency, a condition that can also be considered as fulfilling equation (5). As we will show in the appendix, the derivation of this requires stability, so we cannot expect the relationship to hold in those regions where $\tau < 0$. In the present case, the voltammetry curve itself is the polarization curve for comparison, because the perturbations are away from this condition, which is sufficiently constant during an a.c. cycle.

The extrapolated impedance R_p was evaluated appropriately from the equivalent circuits in the different regions and collated (Figure 16, Table 1). Excluding the regions with negative τ, R_p agrees in sign with dj_{ss}/dE on the positive-going sweep up to about 1 V: it is positive going up to the peak, is infinite at the peak and is negative beyond the peak. The agreement of the Tafel slope for R_{ct} with the Tafel slope for the steady-state current [40] is a quantitative measure of this agreement, since R_{ct} is equal to R_p in the Tafel region. In the second quadrant region, where $R_p = R_0$ (circuit L'), R_p^{-1} correctly shows a minimum at the inflection point in the voltammetry curve. More quantitatively, the slope of the current potential curve at that point agrees within a factor of two with R_p^{-1}, which is good agreement considering the long extrapolation to find R_0 and the error in the slope. Later in the sweep, the expectation of equation (5) is not met: R_p tends to minus infinity at 1.00 V and not at the current minimum near 1.1 V. Also the inverse of the resistance taken from the single semicircle in the last part of the sweep (>1.0 V) appears to track the current rather than its derivative, showing a finite maximum when it should become infinite at 1.46 V. Therefore, in this last part of the forward sweep, there may be unmeasured features at lower frequencies inaccessible to our experiment.

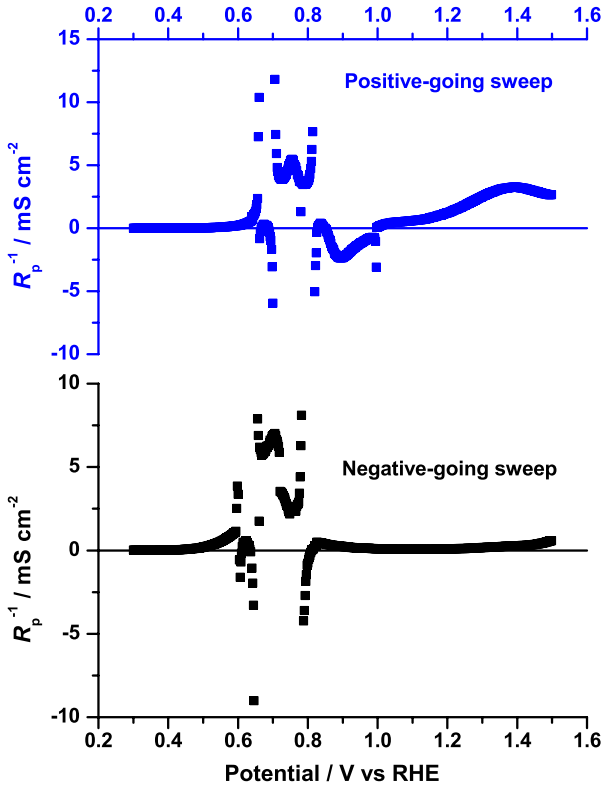

Figure 16 Polarization resistance R_p determined by extrapolation of the impedance to zero frequency.

On the reverse sweep the signs of R_p and the voltammetry slope agree, except in the negative τ regions and near the peak where we could not fit the low-frequency relaxation. Also, as the potential goes below 0.825 V, the current rises, but there is a delay of 20 mV before R_p becomes negative. In this region at this sweep rate the second quadrant behaviour indicating negative R_p is seen only in extrapolation. The long extrapolation and the consequent large error in R_p may explain the apparent delay of 20 mV.

3.4 Discussion

Our discussion will be in terms of a fairly well accepted simplified version of the mechanism:

$$CH_3OH \xrightarrow{\nu_{CO}} CO_{ads} + 4H^+ + 4e^- \quad (6)$$

$$H_2O \xrightarrow{\nu_{OH}} OH_{ads} + H^+ + e^- \quad (7)$$

$$CO_{ads} + OH_{ads} \xrightarrow{\nu_{CO_2}} CO_2 + H^+ + e^- \quad (8)$$

or

$$CH_3OH \rightarrow CO_{ads} + 4H^+ + 4e^- \quad (9)$$

$$H_2O \rightarrow O_{ads} + 2H^+ + 2e^- \quad (10)$$

$$CO_{ads} + O_{ads} \rightarrow CO_2 \quad (11)$$

CO is assumed to be the only carbon-containing adsorbate on the surface. Adsorbed CO is then oxidized to CO_2, and there are several possibilities for the oxygen source. Since Pt oxide does not form below 0.75 V, we assume that the oxygen source below 0.75 V is dissociated water, i.e., OH_{ads} [41,42] (adsorbed water or oxide, perhaps in activated forms, are other species suggested to exist in this potential region [43-46], and the exact identity of the species remains inconclusive). For potentials above 0.75 V, we write the involvement of the oxide as O_{ads}, though the species is not really this simple. The initial stages of Pt oxide were long thought to involve formation of an adsorbed OH species, though Harrington argued against this [33] and more recent EQCM evidence also suggests that the species is oxygen and not OH [47].

3.4.1 Number of adsorbed species

Equivalent circuits for a mechanism with a single adsorbed intermediate generally contain one capacitor or inductor in addition to the double-layer element and the charge-transfer resistance [36,48,49]. A second resistor is also found provided that the d.c. current is not zero. The circuits found here all fall into this category, or are simpler than this. For two adsorbed species we may in general expect an additional capacitor or inductor, but we do not find any evidence for this. We conclude that the kinetics can be written in terms of a single adsorbed intermediate. Because the above mechanism requires at least

two adsorbed species, it is surprising that the circuit is not more complicated. Evidently we have only a single "kinetically-significant" adsorbed intermediate.

Müller et al. [24] and Otomo et al. [30] interpreted their data to mean that there was only one adsorbed species on the surface, namely CO, but it is evident that adsorbed water, OH or oxide must also be present on the surface. Melnick et al. [28] recognized that other species must be present on the surface, despite the fact that they also found equivalent circuits appropriate for a single adsorbed intermediate, and concluded that the rate of turnover of all but one intermediate is fast. However, since the rate-determining step (rds) involves reaction of the two adsorbed intermediates at least in some potential regions, e.g., reaction (8), their rates of removal and production must be coupled, and we therefore propose an alternative explanation.

Before the main methanol oxidation peak, the surface is fully covered with CO, $m\theta_{CO} = 1$. Here m is the number of Pt atoms occupied by an adsorbed CO (not necessarily an integer) and the coverage θ_{CO} is defined as the ratio of the number of adsorbed CO molecules to number of Pt atoms in the surface layer. As the surface oxidizes, the adsorbed oxygen source will partially cover the surface with coverage θ_O (or θ_{OH}), with each adsorbate covering n Pt atoms. Furthermore, if the reaction between these species is the rds, then immediately after they react to release reaction sites, the reaction sites will become covered with either adsorbed CO or adsorbed O, via the fast reaction (7) or (6). In this way the surface will always be fully covered with adsorbates, and we expect that $n\theta_O + m\theta_{CO} = 1$. Therefore, any kinetic equations involving the two species may be converted to kinetic equations for one of them by using this relationship to eliminate one of the variables, e.g., substituting θ_O with $(1-m\theta_{CO})/n$ will lead to equations only in θ_{CO}. Note that under this assumption, the two differential equations for the two species become multiples of each other and one may be discarded: $md\theta_{CO}/dt = -nd\theta_O/dt$. In this sense there is only one kinetically-significant intermediate. This treatment assumes that OH and CO compete for the same adsorption sites, e.g., an OH could not be on an atop site with a CO on a bridge site involving the same platinum atom. It could be modified to allow for different types of adsorption sites and local repulsions without affecting the qualitative conclusions.

Hsing et al. [29] interpreted their impedance data in terms of a model with two adsorbates (CO and OH) but found that the parameters are such that the total coverage is close to one (Figure 5 in ref. [29]). Their impedance spectra show only two arcs as would occur for a single-adsorbate mechanism, so that their data are also consistent with the above idea of one kinetically-significant

intermediate. Both Hsing and Melnick have spectra which go into both the second and third quadrants, where we see only second quadrant behaviour. However, this is a region where we do not have a higher-frequency semicircle, so the evidence for more than a single adsorbate is weak.

On the other hand, there have been reports of more complicated EIS spectra. Lee et al. [25] saw evidence for more relaxations near the shoulder on the leading edge in the forward peak, and related their spectra to the presence of a Hopf bifurcation. They report spectra only over a very narrow potential range. This is the potential range where the mechanism transitions from one oxygen source to another, and so the presence of at least one additional species is expected. We assume that, except for this transition region, one of the oxygen sources dominates. Diard et al. [23] have argued that three adsorbed intermediates are present, based on preliminary measurements in a working fuel cell. However, given that Otomo et al. see a high-frequency semicircle unrelated to kinetics on supported catalysts, and that the presence of a CPE may distort semicircles, this point needs further investigation.

3.4.2 Mechanism

Initial NGC kinetics

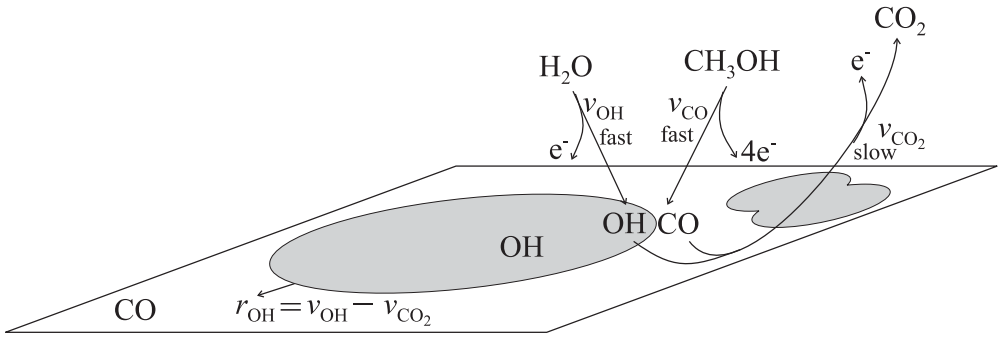

Figure 17 Reaction scheme for potentials < 0.75 V, where OH is assumed to be the oxygen source.

The time for CO_{ads} production from methanol is of the order of a few tenths of a second [8] (see also chapter 2 in this thesis), so that there is adequate time during the reverse scan to produce a surface fully covered by CO. As the methanol oxidation peak current rises in the forward sweep, the Tafel behaviour

of R_{ct} indicates a one-electron process. We also find evidence for involvement of the changing coverage of an adsorbed species, since the circuits have a lower-frequency relaxation in addition to the double-layer/R_{ct} relaxation. Evidence for an NGC mechanism (sweep reversal and sweep hold experiments, negative τ) is found early after the evidence of the second relaxation, but persists only for a small potential region. We suppose that the water dissociates in this region to give OH_{ads} according to reaction (7), and then small islands of OH_{ads} grow in the sea of CO_{ads}. The rate-determining step is reaction (8) at the edge of the islands, and then the OH_{ads} quickly fills the vacant reaction sites, leading to island growth as shown in Figure 17. Oxidation of CO as the rds has often been proposed, e.g., [50,51].

The fresh Pt reaction sites created by the rds are quickly filled by adsorbed molecules from the relatively faster CO and OH adsorption steps. In effect these steps are fast steps after the rds, and so the 1-electron Tafel slope is explained by reaction (8) rather than the water dissociation reaction (7). The methanol to CO conversion must be a complex series of steps, but viewing them as fast downhill processes following the rds step explains why it is reasonable to treat them as a single reaction with apparently simultaneous transfer of four electrons, and also why more intermediate adsorbed species are not detected in large quantities.

A feature of this mechanism is the competition of these two reactions for the sites, and the fact that the relative rates of these competitive reactions may change with potential. This competition determines the rate of growth of the OH islands. If $v_{CO} = v_{OH} = v_{CO2}$, we have steady state and the islands do not grow. For $v_{OH} > v_{CO}$, the islands grow in size; for $v_{OH} < v_{CO}$, they shrink. We suppose that OH adsorption is strongly favoured in the early stages and the islands grow. If the methanol to CO reaction (6) increases rate more quickly with potential than the OH adsorption reaction (7), then CO production may eventually dominate and stifle island growth, or even lead to shrinking islands. In the classical NGC mechanisms [52], it is usually assumed that every electron causes island growth and that the growth rate is positive (no shrinking). Accordingly, we must be wary of applying the classical NGC equations in too simplistic a fashion.

Many signatures of NGC can also be exhibited by the classical Langmuir-Hinshelwood mechanism, i.e., with the rds reaction rate proportional to the

product $\theta_{CO}\theta_{OH}$ and not on the island perimeter.[1] This includes rising current transients at constant potential or upon sweep reversal. Both NGC [53,54] and LH [20] have been proposed for electrochemical oxidation of CO; NGC has been shown by STM for gas-phase CO oxidation [55]. Pletcher and Solis [56] suggested NGC kinetics for methanol oxidation on Pt and it is clear that NGC is appropriate on nanostructured Pt/Ru electrodes where the CO and OH species are physically segregated. Hsing et al. [29] have shown satisfactory agreement between their impedance spectra and detailed modelling of LH kinetics on the same mechanism as equations (6)-(8), so the LH and NGC versions of these mechanisms are not easily distinguished. Schell has likewise used LH kinetics to explain exotic dynamic behaviour in methanol oxidation [57]. The mass-action form $\theta_{CO}\theta_{OH}$ in LH kinetics implies that all CO and OH molecules have equal access for reaction, a condition that seems to be inapplicable for coverages close to unity, so we prefer NGC kinetics.

Three qualitative observations support the NGC mechanism proposed here. (1) Rotating disk electrode (RDE) studies show that increasing the rotation rate decreases the current in this potential region [58,59], in contrast to the cases of formic acid and formaldehyde oxidation [58]. A decreased current is unexpected since most mechanisms lead to a rate increase when the reactant flux to and product flux away from the electrode are enhanced. However, increasing the methanol flux to the surface in the proposed mechanism will increase ν_{CO}, leading to a decrease in island size and so a reduction in the rate of the rds, and reduced current. (2) This RDE inhibition is suppressed on high area carbon supported Pt catalysts, consistent with fixed island sizes constrained by the nanoparticle geometry (ref. [59] explains these effects instead in terms of formaldehyde diffusion away from the electrode). More generally, methanol oxidation at Pt is sensitive to restructuring of the electrode caused by aging or electrochemical or thermal pretreatment [51,56,60,61]. Such surface treatments can affect nucleation density or size or shape of the islands of OH, thus affecting the number of active perimeter sites. (3) The observation of instability (negative τ) is not easily explained by the classical LH mechanism, which cannot show instability at any steady state [62]; at least when all reactions have non-zero back-reaction rates and $m = n = 1$. Interestingly, the experimental spectrum of Hsing et al. at 0.300 V vs. Ag|AgCl ([29], Fig. 1a) shows a distorted region at low frequencies suggestive of heading below the real axis with negative slope as our data does in the negative τ region (e.g., 0.680 V spectrum in Figure 12). Their theoretical spectrum (using LH kinetics) at the

[1] The term Langmuir-Hinshelwood means that the products form from reaction of two adsorbed species, but often also implies kinetics proportional to the product of the coverages; we use the term in the latter more restrictive sense here.

same potential shows a slightly different shape and it is not clear whether below-axis behaviour would have been observed either experimentally or theoretically. It may be that the slow-sweep impedance used here allows access to regions that cannot be probed at true steady state. We note that instability can arise in the LH mechanism if *m* or *n* is two or higher [62].

A detailed derivation of the impedance for the proposed model is outside the scope of the present paper, since the model has features requiring further theoretical development, such as reversible or negative island growth rates, disappearance of nuclei and incorporation of NGC in a multistep reaction sequence (disappearance of nuclei has been considered by Fletcher [63], though not for impedance and not with growth of the nuclei.). Accordingly, we defer a more detailed derivation and discuss the qualitative features expected. Nonetheless, the presence of inductive behaviour under other NGC scenarios has been predicted theoretically [64-66] and observed experimentally [66,67]. The sign of the inductor in Rangarajan's approach for progressive NGC depends on $\partial \mathrm{n}K/\partial\eta$, where K is the island growth rate [65]. In his model, the growth rate and electron transfer rate are the same, and so a change of sign of the inductor as the current changes slope is predicted. Here, the growth rate and electron transfer rate are not the same, but we do see that B (or L) changes sign at the main oxidation peak on both forward and reverse sweeps.

The three steps in the simplified mechanism all occur at island edges, and so their rates each have the form $v = kp$, where p is the total island perimeter. We assume that p plays a role similar to θ in Langmuir kinetics. In the case of instantaneous NGC, there is a formula for p as a function of θ and so either variable may be used as the state variable. The situation is less clear for progressive NGC, but we assume that the parameters τ and B remain the relevant combinations of kinetic parameters.

The parameter $\tau^{-1} = -\left(\partial r_\theta/\partial\theta\right)_E \big/ \Gamma_\mathrm{m}$ is related to the stability of the mechanism [48,49,68]. The tendency for the system to relax back to steady state after a small perturbation defines stability and is indicated by positive τ. In simple Langmuir adsorption, deposition of adsorbate decreases the number of free sites and reduces the adsorption rate, i.e., $\left(\partial r_\theta/\partial\theta\right)_E < 0$ and $\tau > 0$. For NGC with island sizes increasing but small enough that collision effects are insignificant, deposition of adsorbate increases the perimeter and increases the adsorption rate; this positive feedback effect leads to negative τ, as observed in the early stages of the peak (0.662-0.700 V).

In the classical NGC theory, τ becomes positive when the islands collide to such an extent that the island perimeter is decreasing with coverage. The fractional coverage at which this change of sign occurs for instantaneous NGC is 0.39; for progressive NGC it depends on the nucleation history. Christensen's IR data shows that significant CO coverage decrease takes place from about 0.6 V and is reduced to about half by 0.7 V [51], which is approximately the region where $\tau > 0$. Other studies lead to similar conclusions about the potential region where significant CO coverage decrease occurs, e.g., [69,70], but the experimental conditions vary widely and the CO coverage under our conditions remains uncertain. Further uncertainty arises because classical NGC mechanisms are irreversible, and do not account for the possibility of a growth rate that decreases with potential or becomes negative. An alternative explanation for $\tau > 0$ is that the CO adsorption rate outstrips the OH adsorption rate. Then a notional deposition of OH adsorbate leads to an increased perimeter, at which CO adsorption is favoured and the island shrinks back; this is a negative feedback situation with positive τ. In either case, the change in perimeter may be relatively small (a four-fold increase in coverage from 0.1 to 0.4 leads to only a 50% increase in perimeter for classical instantaneous NGC). The rise to the peak is then a quasi steady-state regime (p roughly constant) in which the current and the charge-transfer resistance show Tafel dependence reflective of the single-electron rds.

Oxide Region

Just before the peak, τ becomes briefly negative again, and the double-layer capacitance indicates that oxide formation is significant (as in the blank solution at these potentials). This indicates growth of islands of oxide, perhaps forming preferentially on the regions previously covered by OH. The downward part of the peak demonstrates the inhibiting nature of the oxide. This inhibition effect is demonstrated most dramatically on the reverse sweep at low methanol concentrations where oxide reduction current must occur before anodic methanol oxidation current is possible (Figure 1). However, this inhibition cannot be total because methanol oxidation can occur on the fully-covered oxide at higher potentials on the forward sweep and on the reverse sweep at higher methanol concentrations. The inhibition on the downward part of the sweep could be due to the oxide progressively removing area on which the $OH_{ads} + CO_{ads}$ reaction can take place, or could be due to a reduction in the perimeter of oxide islands at which the $O_{ads} + CO_{ads}$ reaction takes place. We note that NGC signatures are not seen for oxide growth in base electrolyte, so

island growth in the presence of methanol would be an effect induced by the presence of CO on the surface.

The oxide formation in the voltammetry leads to decreasing current and second quadrant impedance behaviour. Here $\tau > 0$ and the resistance R_0 in circuit L' is negative. It is negative because it is equal to the polarization resistance, which is negative because the current-potential curve has negative slope. Therefore, the inductance in circuit L' must be negative ($L = R_0/\tau$). The more difficult fact to explain is that the parallel charge-transfer resistance in circuit L is not detectable here. One possibility is that R_0 may play the role of a charge-transfer resistance; Melnick and Palmore [28] interpreted the negative resistance in this region as a charge-transfer resistance. However, a charge-transfer resistance that is negative and that is not the limiting high-frequency element in the faradaic impedance is unusual. It seems more likely that R_{ct} is present, but is not detectable by the fitting routine. A slight curvature in the CPE slope caused by a very large R_{ct} might not be reliably detected (see 0.910 V curve in Figure 12); similarly a very small R_{ct} at high frequencies might not be detected. It is interesting that R_{ct} is detectable as a parallel element in the corresponding region of negative current-potential slope on the reverse sweep. This region occurs at more negative potentials on the reverse sweep, and therefore the oxidation reactions have lower overpotentials. This should lead to larger R_{ct}, making it probable that R_{ct} is not detected on the forward sweep because it is too small. Further modelling is required to resolve this issue.

For potentials more positive than 1.1 V, the impedance is less informative, since only a resistor can be reliably extracted from the data to represent the faradaic process. This is the region in which the oxide growth shows a current plateau in the base electrolyte. The oxide growth itself should give resistances in this region of the order of 10 kΩ cm^2 (from [33], with a correction factor of two because of the sweep rate difference). The observed resistances here are much smaller, so that it is unlikely that oxide growth is rate-limiting. The absence of an adsorption relaxation in this region may be attributed to the fact that the oxide fully covers the surface in this region, and therefore gives kinetics that are zero-order with respect to oxide.

Melnick et al. [31] have discussed a slow time-dependent process that takes place during methanol oxidation. In particular, the impedance around 0.75 V shows an evolution from second quadrant to first quadrant behaviour with time, attributed by them to slow build-up of an intermediate such as OH_{ads}. Because we are sweeping, we are able to show that the second quadrant behaviour is due to inhibition by Pt oxide, and therefore the time dependence arises from the

continuous irreversible formation of oxide. The impedance evolves from that seen here during the inhibition as the current decreases on the forward sweep (0.85 - 1.0 V) to that seen on the oxide-covered surface (>1 V).

Reverse Sweep

Most of the impedance features on the reverse sweep may be explained similarly to the corresponding features on the forward sweep. The principal differences have already been noted: (1) the second quadrant behaviour on the reverse sweep is observed only in extrapolation at 5 mV s^{-1},but can be observed already at frequencies around 1 Hz at 10 mV s^{-1} (Figure 6), due to the initial oxide reduction being spread out in potential at the faster sweep rate, and (2) in this region of negative current-potential slope, a parallel charge-transfer resistance is detected.

3.5 Conclusions

The slow-sweep collection of EIS spectra allows correlation of spectral features with d.c. voltammetry features, aiding in their interpretation. A variety of spectral types were observed, and these showed only a single adsorption relaxation aside from the double-layer/charge-transfer relaxation, though some structure in the phase of the latter relaxation hints at another process. Regions of negative relaxation times were observed, and these and the inductive behaviour were interpreted in terms of a nucleation-growth-collision mechanism. The negative τ corresponds to island growth before island collisions predominate, an unstable behaviour that is not accessible through conventional steady-state EIS measurements.

The potential dependence of the charge-transfer resistance in the rising part of the oxidation peak indicates that the rds involves a single electron transfer. This was assumed to be the reaction of adsorbed OH and CO at the edge of OH islands. The rest of the surface is covered with CO, so that only one single coverage, that of OH, is required to describe the state of the surface and the kinetics. This explains the observation of only a single adsorption relaxation. Release of reaction sites by the rds is followed by a competition for these sites by OH and CO adsorption from water and methanol respectively. Enhancement of mass transfer of methanol at the RDE favours CO adsorption and decreases the rate at which the islands grow.

Just prior to the peak, a second region of negative τ indicates growth of islands of Pt oxide, and this is followed by inhibition of the methanol oxidation current by the oxide. This oxide inhibition is associated with second quadrant behaviour in the impedance, and is postulated to be the source of the slow evolution of EIS spectra observed in steady-state experiments.

Further development of this model requires advances in the theory of nucleation and growth impedance, coupled with ongoing quantitative analyses of RDE and hydrodynamic impedance data.

3.6 Acknowledgements

F.S. thanks the Norwegian Research Council for the award of a scholarship. We thank Science and Engineering Research Canada, the University of Victoria, and the Norwegian University of Science and Technology (NTNU) for financial support of this research.

3.7 Appendix

Here we give a mathematical proof that stability is a prerequisite for the polarization resistance measured by impedance to be the same as that measured from the slope of the current-potential curve. Suppose that the system is under potentiostatic control at potential E at which the steady-state current density is j. We make a small step in potential δE away from steady-state and wait for a new steady-state. The Laplace transform of a small potential step at time $t = 0$ is δE/s. Therefore the Laplace transform of the current output perturbation of the linearized system is the transfer function Y(s) times δE/s. The value of the current perturbation can be found from the final value theorem $f\left(t=\infty\right)=\lim_{s\to 0} sF\left(s\right)$, [71].

The result is that $\delta j=\lim_{s\to 0} sY\left(s\right)\delta E/s=\lim_{s\to 0} Y\left(s\right)\delta E=\delta E\lim_{s\to 0} Y\left(s\right)$. Thus the slope of the polarization curve $\delta j/\delta E$ is equal to $\lim_{s\to 0} Y\left(s\right)$, which is the polarization resistance determined by extrapolating the impedance spectrum to zero frequency. The proof of the final value theorem requires stability, i.e., the absence of poles in the closed right half plane.

References

[1] T. Iwasita, in: *Handbook of Fuel Cells - Fundamentals, Technology and Applications*, W. Vielstich, H.A. Gasteiger, A. Lamm (Eds.), *Vol 2 Electrocatalysis*, John Wiley & Sons, Chichester, 2003, p. 603

[2] T. Iwasita, *Electrochim. Acta*, **47** (2002) 3663

[3] J.-M. Léger, *J. Appl. Electrochem.*, **31** (2001) 767

[4] S. Wasmus, A. Küver, *J. Electroanal. Chem.*, **461** (1999) 14

[5] P. Waszczuk, G.-Q. Lu, A. Wieckowski, C. Lu, C. Rice, R.I. Masel, *Electrochim. Acta*, **47** (2002) 3637

[6] K. Franaszczuk, E. Herrero, P. Zelenay, A. Wieckowski, J. Wang, R.I. Masel, *J. Phys. Chem.*, **96** (1992) 8509

[7] E. Herrero, W. Chrzanowski, A. Wieckowski, *J. Phys. Chem.*, **99** (1995) 10423

[8] G.-Q. Lu, W. Chrzanowski, A. Wieckowski, *J. Chem. Phys. B*, **104** (2000) 5566

[9] T.D. Jarvi, E.M. Stuve, in: *Electrocatalysis*, Eds. J. Lipkowski and P.N. Ross, Wiley-VCH, New York, 1998, p. 75

[10] T. D. Jarvi, S. Sriramulu, and E.M. Stuve, *J. Phys. Chem. B*, **101** (1997) 3650

[11] T.D. Jarvi, S. Sriramulu, E.M. Stuve, *Colloids and Surfaces A* **134** (1998) 145

[12] C. Korzeniewski and C.L. Childers, *J. Phys. Chem. B*, **102** (1998) 490

[13] S. Sriramulu, T.D. Jarvi, E.M. Stuve, *J. Electroanal. Chem.*, **467** (1999) 132

[14] B. Ren, X.Q. Li, C.X. Shi, D.Y. Wu, Z.Q. Tian, *Electrochim. Acta*, **46** (2000) 193

[15] H. Wang, C. Wingender, H. Baltruschat, M. Lopez, M.T. Reetz, *J. Electroanal. Chem.*, **509** (2001) 163

[16] H. Wang, T. Löffler, H. Baltruschat, *J. Appl. Electrochem.*, **31** (2001) 759

[17] E.A. Batista, G.R.P. Malpass, A.J. Motheo, T. Iwasita, *Electrochem. Comm.* **5** (2003) 843

[18] E.A. Batista, G.R.P. Malpass, A.J. Motheo, T. Iwasita, *J. Electroanal. Chem.*, **571** (2004) 273

[19] K. Jambunathan, S. Jayaraman, A. C. Hillier, *Langmuir* **20** (2004) 1856

[20] N.P. Lebedeva, M.T.M. Koper, J.M. Feliu, R.A. van Santen, *J. Electroanal. Chem.* **524-525** (2002) 242.

[21] N. Nakagawa, Y. Xiu, *J. Power Sources*, **118** (2003) 248

[22] J.C. Amphlett, B.A. Peppley, E. Halliop, A. Sadiq, *J. Power Sources*, **96** (2001) 204

[23] J-P Diard, N. Glandut, P. Landaud, B. Le Gorrec, C. Montella, *Electrochim. Acta*, **48** (2003) 555

[24] J.T. Müller, P.M. Urban, W.F. Hölderich, *J. Power Sources*, **84** (1999) 157

[25] J. Lee, C. Eickes, M. Eisworth, G. Ertl, *Electrochim. Acta*, **47** (2002) 2297

[26] E.H. Yu, K. Scott, R.W. Reeve, *J. Electroanal. Chem.*, **547** (2003) 17

[27] D.C. Azevedo, W.H. Lizcano-Valbuena, E.R. Gonzalez, *J. New Mat. Electrochem. Systems*, **7** (2004) 1

[28] R.E. Melnick, G.T.R. Palmore, *J. Phys. Chem. B*, **105** (2001) 1012

[29] I.-M. Hsing, X. Wang and Y.-J. Leng, *J. Electrochem. Soc.*, **149** (2002) A615

[30] J. Otomo, X. Li, T. Kobayashi, C. Wen, H. Nagamoto, H. Takahashi, *J. Electroanal. Chem.*, **573** (2004) 99

[31] R.E. Melnick, G.T.R. Palmore, *J. Phys. Chem. B*, **105** (2001) 9449

[32] D.A. Harrington, *J. Electroanal. Chem.*, **355** (1993) 21

[33] M.E. Van der Geest, N.J. Dangerfield, D.A. Harrington, *J. Electroanal. Chem.*, **420** (1997) 89

[34] ZSimpWin v 3.10, 2002, Echem Software, *http://www.echemsw.com*

[35] P.R. Bevington, *Data Reduction and Error Analysis for the Physical Sciences*, McGraw Hill, New York, 1969, p. 200

[36] D.A. Harrington, B.E. Conway, *Electrochim. Acta*, **32** (1987) 1703

[37] G.J. Brug, A.L.G. van den Eeden, M. Sluyters-Rehbach, J.H. Sluyters, *J. Electroanal. Chem.*, **176** (1984) 275

[38] D. Schuhmann, *Electrochim. Acta*, **35** (1990) 1527

[39] C. Gabrielli, B. Tribollet, *J. Electrochem. Soc.*, **141** (1994) 1147

[40] V.S. Bagotsky, Yu.B. Vassilyev, *Electrochim. Acta*, **12** (1967) 1323

[41] N.M. Markovic, T.J. Schmidt, B.N. Grgur, H.A. Gasteiger, R.J. Behm, P.N. Ross, *J. Phys. Chem. B*, **103** (1999) 8568

[42] A.B. Anderson, N.M. Neshev, *J. Electrochem. Soc.*, **149** (2002) E383

[43] K. Shimazu, H. Kita, *J. Electroanal. Chem.*, **341** (1992) 361

[44] E. Herrero, K. Franaszczuk, A. Wieckowski, *J. Phys. Chem.* **98** (1994) 5074

[45] L.D. Burke, *Electrochim. Acta.*, **39** (1994) 1841

[46] L.D. Burke, A.J. Ahern, *J. Solid State Electrochem.*, **5** (2001) 553

[47] G. Jerkiewicz, G. Vatankhah, J. Lessard, M.P. Soriaga, Y.-S. Park, *Electrochim. Acta*, **49** (2004) 1451

[48] R.D. Armstrong, M. Henderson, *J. Electroanal. Chem.*, **39** (1972) 81

[49] D.A. Harrington, P. van den Driessche, *J. Electroanal. Chem.*, **501** (2001) 222

[50] H.A. Gasteiger, N. Markovic, P.N. Ross Jr., E.J. Cains, *J. Phys. Chem.*, **97** (1993) 12020

[51] P.A. Christensen, A. Hamnett, G.L. Troughton, *J. Electroanal. Chem.*, **362** (1993) 207

[52] M. Fleischmann, H.R. Thirsk, *Adv. Electrochem. Electrochem. Eng.*, **3** (1963) 123

[53] C. McCallum, D. Pletcher, *J. Electroanal. Chem.*, **70** (1976) 277

[54] B. Love, J. Lipkowski, *ACS Symp. Ser.* **378** (1988) 484

[55] J. Winterlin, S. Volkerling, T.V.W. Janssens, T. Zambelli, G. Ertl, *Science*, **278** (1997) 1931

[56] D. Pletcher, V. Solis, *Electrochim. Acta*, **27** (1982) 775

[57] M. Schell, *J. Electroanal. Chem.*, **457** (1998) 221

[58] F. Seland, D.A. Harrington, R. Tunold, 203rd Mtg Electrochem. Soc, Abstr. Vol 2003-01, Abstr. 1229

[59] S. Lj. Gojkovic, *J. Electroanal. Chem.*, **573** (2004) 271

[60] L.D. Burke, L.M. Hurley, *Electrochim. Acta* **44** (1999) 3451

[61] A. Wieckowski, V.N. Andreev, R. Zelenay, J. Sobkowski, V.E. Kazarinov, *Elektrokhimiya* **16** (1980) 668

[62] J.D. Campbell, D.A. Harrington, P. van den Driessche, J. Watmough, *J. Math. Chem.*, **32** (2002) 281

[63] S. Fletcher, *J. Electroanal. Chem.*, **215** (1986) 1

[64] R.D. Armstrong, A.A. Metcalfe, *J. Electroanal. Chem.*, **71** (1976) 5

[65] S.K. Rangarajan, Symp. *Faraday Soc.*, **12** (1977) 101

[66] C. Cachet, I. Epelboin, M. Keddam, R. Wiart, *J. Electroanal. Chem.*, **100** (1979) 745

[67] I. Epelboin, M. Ksouri, R. Wiart, Symp. *Faraday Soc.*, **12** (1977) 115

[68] C.-N. Cao, *Electrochim. Acta*, **35** (1990) 831

[69] P. Waszczuk, A. Wieckowski, P. Zelenay, S. Gottesfeld, C. Coutanceau, J.-M. Léger, C. Lamy, *J. Electroanal. Chem.*, **511** (2001) 55

[70] R. Liu, H. Iddir, Q. Fan, G. Hou, A. Bo, K.L. Ley, E. S. Smotkin, Y.-E. Sung, H. Kim, S. Thomas, A. Wieckowski, *J. Phys. Chem. B*, **104** (2000) 3518

[71] F.F. Kuo, *Network Analysis and Synthesis*, 2nd Ed., Wiley, New York, 1966, p. 167

Chapter 4

Impedance Study of Formic Acid Oxidation on Platinum Electrodes

Frode Seland [a,b], Reidar Tunold [a] and David A. Harrington [b]

[a] *Electrochemistry Group, Department of Materials Science and Engineering, Norwegian University of Science and Technology, NO-7491, Trondheim, Norway.*

[b] *Department of Chemistry, University of Victoria, Victoria, British Columbia, V8W 3V6, Canada.*

Abstract

The electrooxidation of formic acid on polycrystalline platinum electrodes in sulphuric acid is studied by a.c. voltammetry. Corresponding impedance spectra in the frequency range 0.7 Hz to 30 kHz are assembled and analyzed using appropriate equivalent circuits in distinct potential regions. Potential regions of negative differential resistance (NDR) and hidden negative differential resistances (HNDR) are identified. Two potential regions in the positive-going scan and one in the negative-going scan are identified with HNDR impedance characteristics implying the ability to sustain oscillations at these potentials. Investigations of the zeroes of impedance showed only real values, eliminating the possibility of oscillations arising from purely chemical reasons.

Keywords: Impedance, Formic Acid, HCOOH, Oxidation, Platinum, Methanol, A.c. Voltammetry, EIS, Bifurcation, Oscillation

4.1 Introduction

The oxidation of formic acid on platinum electrodes has received considerable attention in electrocatalysis research and has been reviewed several times [1-7]. Much of the motivation for the research done on the oxidation of formic acid is based on its potential as a fuel cell feed. Even though the oxidation of formic acid on platinum is considered as a model reaction in electrocatalysis due its simple structure, with only two electrons involved in the total oxidation process to carbon dioxide, the reaction has been found to be rather complex. It is widely accepted that formic acid oxidizes through a dual-path mechanism on platinum electrodes, as originally suggested by Capon and Parsons [8,9]. One of the paths leads to direct formation of CO_2 via short-lived intermediates, whereas the other involves the formation of a stable intermediate, generally accepted to be adsorbed CO, which poisons the catalyst surface and requires a higher voltage to be oxidized.

Virtually all electrochemical reactions are nonlinear, and in electrocatalytic reactions, formation of poisons, oxidation of catalytic surfaces as well as the adsorption of anions, strongly promote the occurrence of dynamic instabilities. Current and potential oscillations in electrochemical systems has been the subject of numerous studies e.g. in metal dissolution [10,11], reduction of hydrogen peroxide [12,13], anodic oxidation of hydrogen [14-18], carbon monoxide [19-21], or in the oxidation of small organic molecules like formaldehyde [22-30], methanol [31,32], and formic acid [22,33-44]. Although it is generally believed that current oscillations arise from oscillating surface coverages by adsorbed formic acid, adsorbed intermediates, oxygen containing species and anions from the supporting electrolyte, the true nature of the oscillatory behaviour is still controversial, e.g. [43,45]. The role of anions is important, and Schmidt et al. [43] suggest that the adsorption of anions leads to competition for free surface sites between three species: water, formic acid and anions. This competition complicates the kinetics and provides another way to induce complex nonlinear dynamics. Schell and co-workers suggest that the adsorbed anions are not only blocking the active surface sites for formic acid adsorption and oxidation, but also that they have an effect on the nature and reactivity of surface water and hydroxide, and consequently their reaction with adsorbed CO [46-49]. They found a remarkable enhancement in the oxidation rate of formic acid [47,49,50] and methanol [51] when replacing a small amount of the supporting electrolyte with HBF_4.

The formic acid system is known to exhibit oscillations and dynamic instabilities primarily due to the interplay between adsorbed species at the

catalyst surface and the catalyst itself, together with a direct oxidation route as the prime current carrier. Wojtowicz [52] pointed out the dissimilarity between chemical and electrochemical oscillatory systems: whereas it is the chemical autocatalysis that leads to instability in the former systems, it is the interplay of chemical and electrical variables which make the latter systems depart from stationary state. Operating a nonlinear electrochemical system far from the thermodynamic equilibrium can provoke a great many dynamic states other than the single stationary state. Koper et al. [53-56], emphasized the central role of a negative differential resistance (NDR) for electrochemical oscillations. A hidden negative differential resistance (HNDR), or hidden negative impedance, is a notation introduced by Koper and Sluyters [56] to explain oscillatory behaviour on a positive slope of the polarization curve. A prominent feature of the hidden negative impedance is the fact that the negative impedance, which makes a system unstable, appears only on a fast time scale and is not visible in a stationary polarization curve [57]. The hidden negative impedance has become a basic concept in the dynamics of electrochemical systems and is used when classifying electrochemical oscillators [53,58].

Electrochemical impedance spectroscopy (EIS) is a powerful tool for studying electrochemical reaction mechanisms and kinetics, but only a small number of experimental studies exist concerning the formic acid oxidation. Matsui et al. [59] showed, by studying the faradaic impedance, that the rate determining step was the adsorption of formic acid molecules at potentials above 0.35 V (outside the hydrogen region). Nonetheless, most work has been done relating oscillatory behaviour to impedance spectra theoretically and showing how to identify bifurcations based on the Nyquist stability criterion [60] and on intuitive physical considerations [53,54,58]. Since EIS involves a small perturbation around the stationary state, experimentally collecting the system's frequency response for a wide enough frequency range gives all the linear information needed to evaluate the system's stability. By remembering that a bifurcation constitutes a transition point where the system changes qualitatively from one type to the other, impedance spectroscopy can be used qualitatively to recognize Hopf and saddle-node bifurcations in an electrochemical system. Ultimately, a bifurcation is a situation where the impedance spectrum intersects or ends up in origin of the complex impedance plane. If it ends up in the origin as $\omega \to 0$ then the system has a saddle-node bifurcation, and if the spectrum intersects the origin, the system undergoes a Hopf bifurcation. In summary, for a fixed applied potential an electrochemical system will exhibit [53]:

$$\text{A saddle-node bifurcation if } Z(\mathrm{i}\omega) = 0,\ \omega = 0 \tag{1}$$

$$\text{A Hopf bifurcation if } Z(\mathrm{i}\omega) = 0,\ \omega = \omega_{\mathrm{H}} \neq 0 \tag{2}$$

Strasser et al. [41] stressed the fact that a sufficiently large ohmic resistance is a prerequisite to obtain oscillations in the formic acid system. This is most commonly achieved by adding a resistor to the working electrode circuit or decreasing the concentration of the supporting electrolyte.

This work is an EIS analysis of impedance data for formic acid oxidation on a polycrystalline platinum electrode collected during slow a.c. voltammetry scans, one frequency per cycle. By introducing a small a.c. signal on top of a slow d.c. ramp we are able to record electrochemical impedance spectra at all potentials during cycling, including where the system is not necessarily at a true steady-state e.g., with partially-covered surfaces. In addition, any slow drifts in the system that occur during steady-state impedance measurements are avoided, and the impedance features can be directly correlated with the d.c. voltammetry. This method has been shown theoretically to give valid results provided that $\omega \gg F\nu/RT$, where $\omega = 2\pi f$ is the angular frequency and ν is the sweep rate [61]. This method was used previously to study the growth of the oxide film on platinum [62] and recently the methanol oxidation on platinum in sulphuric acid (chapter 3 in this thesis, accepted for publication [63]).

4.2 Experimental

Electrooxidation of formic acid in sulphuric acid was studied at a polycrystalline platinum wire (Johnson-Matthey 99.9985%) in a glass cell of conventional design. All electrodes were sealed in glass for easy cleaning and potentials were measured against a hydrogen reference electrode in the same solution (RHE). The electrodes and glass equipment were cleaned in hot chromic acid for a minimum duration of three hours and thoroughly rinsed with Milli-Q water (>18 MΩ cm). Sulphuric acid (Anachemia/Seastar) was made up in Milli-Q water and bubbled with Argon (5.0) prior to and after the addition of formic acid (Fluka Chemica, puriss, p.a. 98%), minimizing the concentration of oxygen present. Current densities are reported with respect to the true surface area in the usual way, by assuming that the charge related to the underpotential deposited hydrogen corresponds to 220 μC cm^{-2}. 0.25 mol dm^{-3} formic acid and 0.5 mol dm^{-3} sulphuric acid was used in all experiments unless otherwise stated.

The platinum working electrode was cycled between the onset of hydrogen evolution and oxygen evolution for at least one hour prior the addition of formic acid. With formic acid present, current densities slowly increased, indicating some enhancement in the electrode activity over the time period required for these slow sweep experiments. To minimize this effect, the

platinum working electrode was further cycled for about 2 hours after addition of formic acid to the electrolyte. The data analyzed in this work came from a single set of a.c. voltammograms collected over an eleven-hour period during which the enhancement was less than 10%, as judged by the increase in charge of the formic acid oxidation peak in the negative-going scan. No features in the voltammogram was altered or created during the experiment other than the slight increase of activity.

The experimental set-up to record a.c. voltammograms at a sweep rate of 5 mV s^{-1}, was identical to that used in the study of methanol oxidation described earlier [63]. It is important to emphasize the use here of a very small amplitude (0.75 mV rms) thus allowing us to examine behaviours occurring over small potential regions in the linear regime. In fact, changes in impedance behaviour over only a few millivolts were found in this study. A mixed analog/digital filtering strategy was used as described previously [61,63]. A.c. voltammograms employing frequencies higher than 30 kHz showed evidence of artifacts and therefore only lower frequencies were used. The impedance was calculated by dividing the complex number for potential by the complex number for current density in the usual way.

A.c. voltammograms were collected from 0.2 Hz up to 30 kHz, one frequency per cycle. Custom software collected the data from all frequencies at a given potential and in this way EIS spectra at given potentials were obtained, comprising of one data point from each a.c. voltammetry cycle. Valid measurements can not be made at too low frequencies since the d.c. sweep is slowly changing the system ($f \gg \nu F / (2\pi RT) = 0.03$ Hz at 5 mV s^{-1} [61]). Impedance spectra were generated for every 2 mV around the voltammogram. However, frequencies lower than 0.7 Hz showed significant randomness indicating that these measurements were on the borderline of validity at this sweep rate and consequently they were not fitted.

The electrochemical impedance spectra were fitted to suitable equivalent circuits by using the software ZSimpWin with modulus weighting. Elements were added to the equivalent circuits only when accepted by the F-ratio test for adding a parameter [64]. As usual the double-layer was better modelled as a constant phase element (CPE) instead of as a capacitor and the fits were significantly improved. More than 5000 equivalent circuit/spectrum combinations were fitted in the course of this study.

4.3 Results

4.3.1 D.c. voltammetry

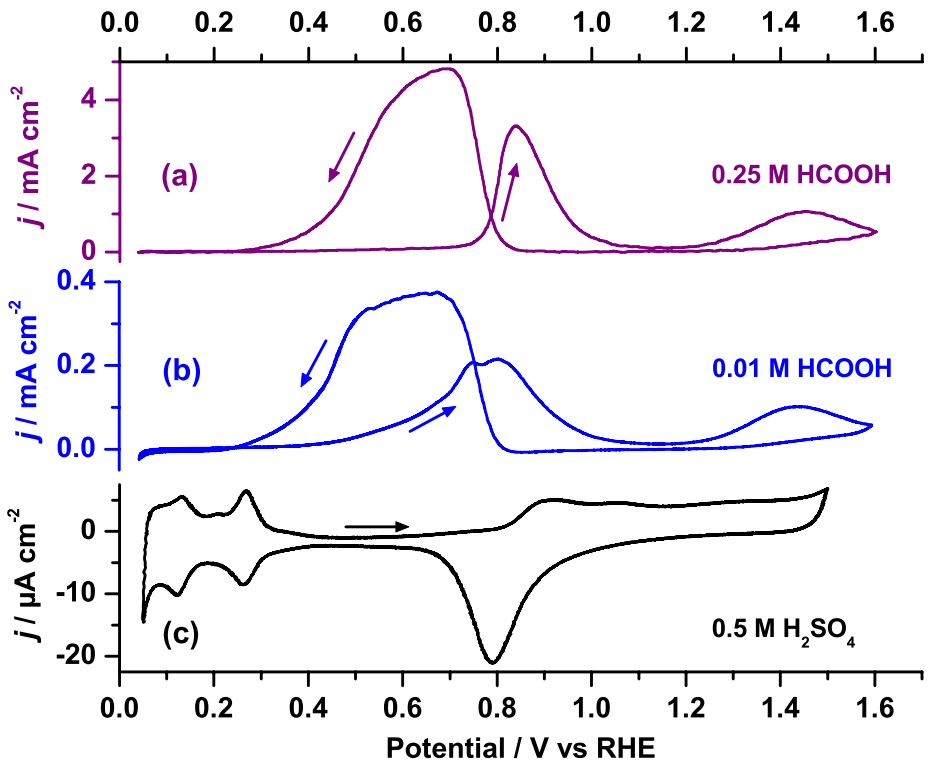

Figure 1 D.c. voltammograms for formic acid oxidation in 0.5 M H_2SO_4 on polycrystalline Pt at room temperature and a sweep rate of 5 mV s^{-1}. (a) 0.25 M HCOOH (b) 0.01 M HCOOH (c) sulphuric acid electrolyte only.

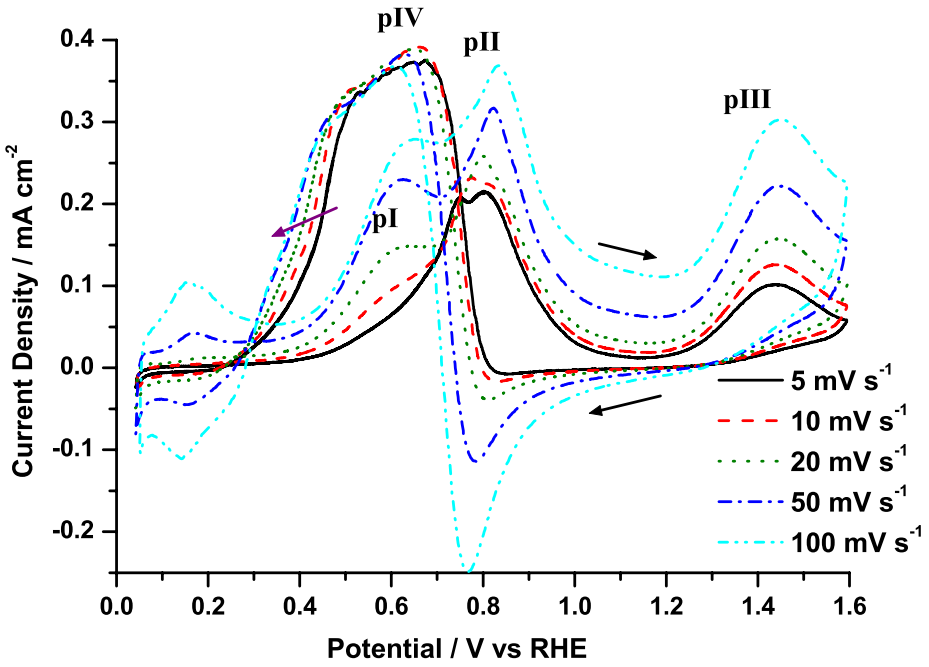

Figure 2 D.c. voltammograms for formic acid (0.01 M) oxidation on platinum, different sweep rates; 5 mV s^{-1} (solid line), 10 mV s^{-1} (dashed line), 20 mV s^{-1} (dotted line), 50 mV s^{-1} (dash-dot line) and 100 mV s^{-1} (dash-dot-dot line).

Representative voltammograms are given in Figure 1 and Figure 2 to illustrate the characteristics of formic acid oxidation on polycrystalline platinum in relationship to the behaviour in sulphuric acid alone. As expected, the hydrogen underpotential deposition peaks at 0-0.3 V in the base electrolyte are suppressed in the presence of formic acid due to the strong adsorption of a poisoning intermediate, most likely CO. When sweeping with a low scan rate, the current slowly increases from about 0.4 V in the positive-going sweep, and goes into the main oxidation peak, which peaks at 0.84 V, exactly the same potential as in the case of methanol with the same sweep rate [63]. The peak is narrower here than for methanol and a rapid increase in current does not happen until 0.73 V at 5 mV s^{-1}. It is important to note that increasing the sweep rate from 5 mV s^{-1} up to 100 mV s^{-1} reveals other voltammetric features, most importantly another oxidation peak in the positive-going scan that commences immediately after the hydrogen region at about 0.3 V, peaks at 0.55 V and merges with the main oxidation peak at 0.73 V. At a concentration of 0.01 M, the main oxidation peak consists of two peaks even at 5 mV s^{-1}. Okamoto et al. showed that the limiting voltammogram at very low sweep rates for formic acid oxidation on platinum at

42 ºC has only one oxidation peak in both the positive and the negative-going sweep directions, peaking at about 0.6 V vs. NHE [65]. They concluded that the adsorbed CO is being oxidized to CO_2 in the positive-going peak, and adsorbed CO is formed in the oxidation peak during the negative-going potential scan. As the concentration is increased, the second peak predominates and the first peak disappears (Figure 1a) and exists now only as a slow, but steady, increase in current density from about 0.3 V up to the main oxidation peak. Although a negative current/potential-slope is not visible in the d.c. voltammogram, signs of other processes in this potential region are visible in the impedance spectra collected at 5 mV s^{-1} based on the indication of a negative resistance when the frequency goes to zero, as discussed below. The decrease in oxidation current above 0.84 V is due to the formation of more platinum oxide, which inhibits further oxidation of formic acid. Further increase in potential leads to an increased current at the most positive potentials suggesting a change in oxidation mechanism probably due to a change in the structure of the surface oxide.

On the negative-going scan, the current initially stays positive but decreases. Once the surface oxide is being reduced, more active Pt sites are made available for adsorption and oxidation of formic acid and the oxidation current increases. This is most easily seen in the low concentration curves with elevated sweep rates (Figure 2), where the current follows the baseline curve (similar voltammogram in sulphuric acid without formic acid present) well into the oxide reduction peak before the oxidation current takes over, i.e., the oxidation of formic acid occurs at freshly reduced platinum sites (peak IV). The oxidation commences at about the same potential with higher formic acid concentration and goes into a broad peak with a noticeable shoulder on the negative potential side. This peak in the negative-going scan supposedly corresponds to the positive-going peak(s) (peak I and II) just slightly shifted to more negative potentials. Finally, the current decreases again, due to formation of strongly bonded intermediates that are not oxidized at lower potentials, thus blocking the active sites for further oxidation.

Sweep rate dependence

Figure 3 demonstrates the oxidation peak current density on Pt in 0.01 M formic acid extracted from the experiment displayed in Figure 2 and plotted against the square root of sweep rate since this will give an indication of diffusion control.

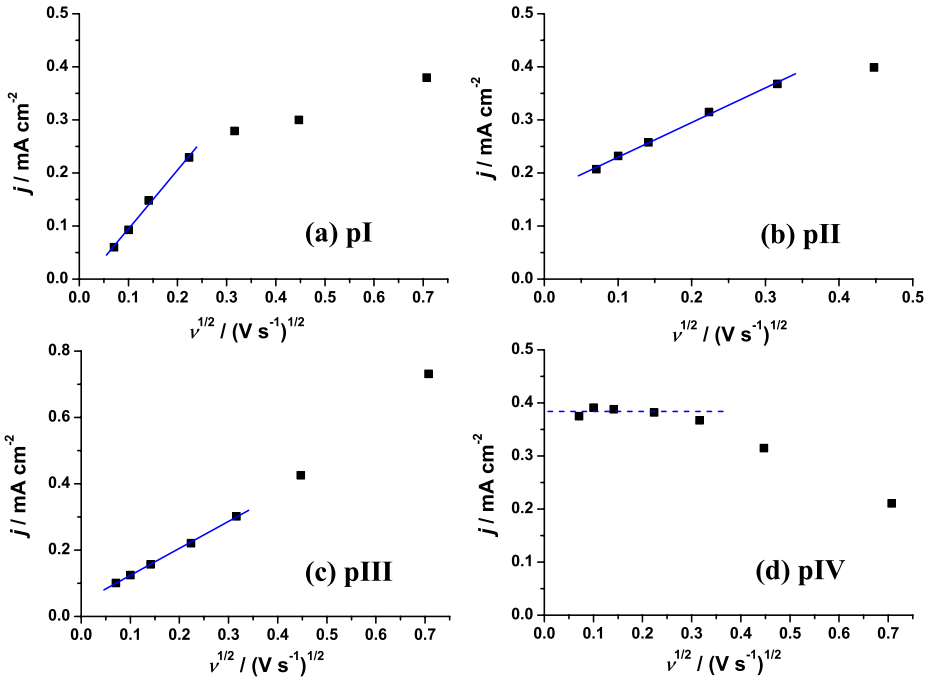

Figure 3 Peak current densities (see also Figure 2) plotted versus the square root of sweep rate, (a) First peak in the positive-going direction, pI (b) Second peak in the positive-going direction, pII (c) High potential peak in the positive-going direction, pIII (d) anodic peak in the negative-going scan, pIV.

Surface processes like adsorption of a complete monolayer hydrogen and oxide formation, are fast reactions that involve equal amounts of charge regardless of sweep rate. This implies that the peak current stemming from a fast surface process, like adsorption, must be proportional to the sweep rate in order to capture the same charge. Finally, the peak current is supposed to be constant if the main faradaic process is coupled with a fast diffusion of reactive species to the electrode without formation of adsorbed species blocking the surface. In our experiment (Figure 2, Figure 3) we observe all these dependencies on the sweep rate. At the slowest scans, some features are lost in the voltammogram, in other words, some features are masked at lower scan rates by a process that does not exhibit the same sweep rate dependence (i.e. pI). However, all peaks in the positive-going scan exhibit a linear relation with the square root of sweep rate at intermediate sweep rates as shown in Figure 3a-c. The hardest one to interpret is the oxidation peak at high potentials, peak III, which involves enhanced oxidation probably due to restructuring of oxide to a more electrocatalytic

active one. The other two peaks in the positive-going scan, peak I and II, are related to the oxidation of formic acid, formation of adsorbed species and surface processes. Irreversible production of CO_2 is assumed to be the main reaction in the last oxidation peak, through oxidation of adsorbed CO with some oxygen containing species at the surface, most likely surface oxide. The first peak, which is detected only as a shoulder and eventually not visible, at slower sweep rates, is a process that is faster than the process in the main oxidation peak. At these potentials, adsorbed CO is being oxidized at a moderate rate by reaction with adsorbed water or hydroxide. The freed sites are being occupied through a competition between adsorption of the oxygen donor and CO. At a slow sweep rate, the CO_{ads} blocking prevails, indicating the immobility of the oxygen donor and the need for free sites, and therefore surface diffusion might be the rate determining step. As the sweep rate is further increased, the underlying surface processes will start to dominate, since they will be proportional to the sweep rate, and then all the peaks will disappear if the sweep rate is fast enough and no faster processes manifests themselves. Interestingly, the oxidation peak in the reverse scan is independent of sweep rate (as long as it is not too high) indicating that only the direct route is happening on freshly reduced platinum at relative low formic acid concentration. This peak is prone to sweep rate mainly due to the platinum oxide's irreversibility leading to a shift in potential to lower values compared to where it is reduced at higher sweep rates, thus causing a delay in the oxidation reaction.

4.3.2 A.c. voltammetry

Examples of the a.c. voltammograms, that are the raw data for the impedance spectra, are given in Figure 4. Some correlation with the d.c. voltammogram is already apparent. The imaginary part of the admittance for the highest frequencies is mainly representative of the double-layer capacitance, and the increased values for potentials above 0.75 V are where the formation of platinum oxide begins, which is known to have a higher double-layer capacitance [62]. Interestingly, the double-layer capacitance seems to exhibit a larger value in the lower end of the double-layer potential region in the reverse scan as compared to the positive-going scan. Clearly, the positive- and negative-going scans are dissimilar, which emphasizes that the impedance spectra that we collect are not for the steady-state condition.

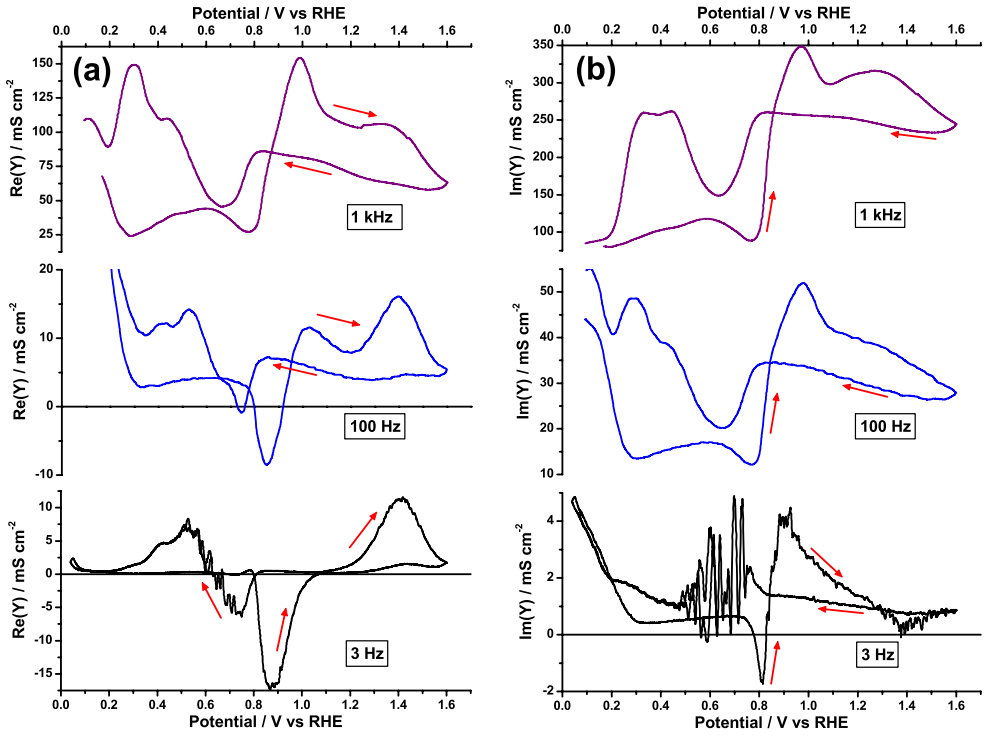

Figure 4 A.c. voltammograms at 1 kHz, 100 Hz and 3 Hz; (a) real part of the admittance, and (b) imaginary part of the admittance

The most interesting potential regions are where the real or the imaginary part of the admittance goes through zero. According to Figure 4, both the real and imaginary part of the admittance possesses potential regions where they cross through zero for the lowest frequencies. More specifically, when the real part of the admittance becomes negative, the impedance spectra are moving into the second quadrant in the Nyquist diagram, while a negative imaginary impedance involves third or fourth quadrant behaviour. Alternatively, when the imaginary part of the admittance crosses through zero and becomes negative, it requires a relaxation involving an inductor (or perhaps a negative capacitor). A negative real part of impedance implies a relaxation involving a negative differential resistor which gives a positive feedback. An expanded version of the 3 Hz curves in Figure 4 are given in Figure 5, for the positive-going sweep only, allowing for more precise determination of potential regions with negative real or imaginary behaviour. First of all it clearly demonstrates that we can expect the impedance to move into all four quadrants in the Nyquist diagram. Specifically, third quadrant behaviour is suggested to happen when both real and imaginary parts of the admittance possess negative values simultaneously at

low frequencies. Figure 5 suggests that this occurs in the potential region 0.8 to 0.83 V, at slightly more negative potentials than the main oxidation peak (Figure 1). Although Figure 4 suggests that this occurs in the negative-going sweep as well, it is less clear due to the noisy results at lower frequencies, especially in the imaginary response in the potential region just on the negative potential side of the main oxidation peak. This is an indication of incipient instability.

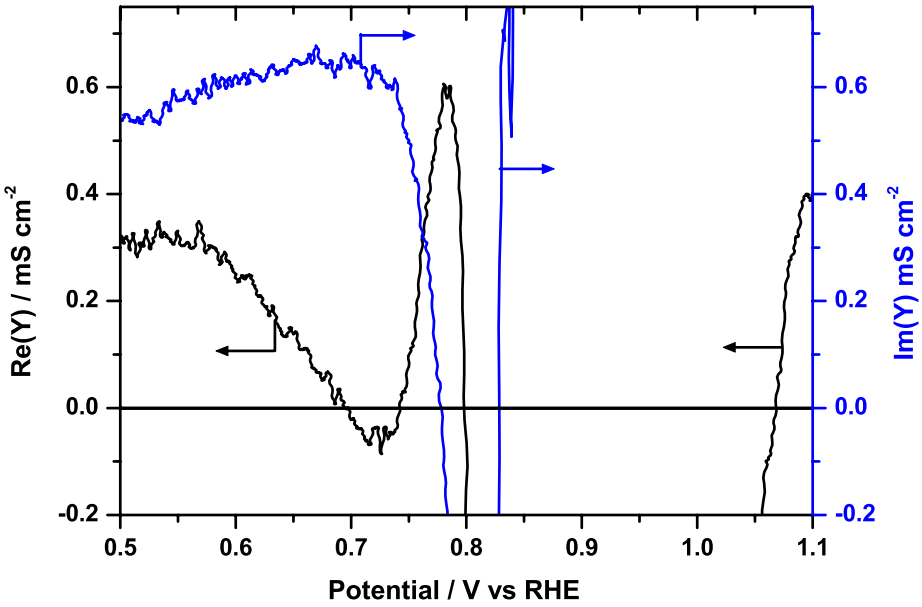

Figure 5 A.c. voltammograms of the positive-going sweep at 3 Hz allowing for easy estimation of the potential regions that exhibit negative real and/or imaginary admittance, and also high-impedance potentials.

Zooming in on the regions of high impedance (regions where the admittance goes through zero) in Figure 5 we see that the real part of the admittance dips below zero and becomes slightly negative at 3 Hz at around 0.69 V. It remains negative until about 0.74 V where there is a sharp increase in the admittance peaking at about 0.78 V indicating a lower polarization resistance at this potential. The real part of admittance goes rapidly to zero and becomes negative just below 0.80 V shaping into a broad (with respect to potential) negative peak and continuing to be negative until about 1.07 V. Simultaneously, the imaginary part of the admittance at a frequency of 3 Hz becomes negative at 0.78 V and positive again at about 0.83 V. Clearly, 3Hz works only as a model frequency as to what happens at lower frequencies, and for even lower frequencies the potential regions that exhibit negative real and/or imaginary admittances are expanded. Both positive-going and negative-going scans exhibit a negative real

part of impedance (not infinity) at the main oxidation peaks suggesting that the peak potentials are not equal to the peak potentials in the steady-state polarization curve. Interestingly, the imaginary part of admittance suggests very high impedance values at potentials approximately at, or slightly more negative (Figure 5) than the voltammetric peak. The low frequency impedance data take on large errors here and become scattered, mainly due to the large errors invoked by taking the reciprocal of small numbers that crosses through zero.

4.3.3 EIS spectra

The experimentally recorded EIS spectra showed the qualitative features of Figure 6. These were analyzed using the equivalent circuits of Figure 7, where circuit 2L represents the equivalent circuit used in this work in potential regions where two kinetically significant species occurred.

The charge-transfer resistance

A negative impedance characteristic caused by a negative differential resistance is often taken to be just the charge-transfer resistance crossing through zero and becoming negative, thus a simple semicircle is obtained in the Nyquist plot that proceeds into the second quadrant (except when $R_{ct} \leq -R_s$; $R_{ct} = -R_s$ defines a saddle-node in this case). The fit to the semicircle can be interpreted as the charge-transfer resistor in parallel with the double-layer, but this raises the issue of what a negative charge-transfer resistance means. An appropriate interpretation of the charge-transfer resistance is that it is a measurement of how much the current increases when increasing the electric field while keeping all concentration and coverage variables constant. Now, an increase in (positive) field $\left(\phi_{\text{metal}} - \phi_{\text{solution}}\right)$ must tend to drive positive charges into the solution or electrons into the metal thus indicating that the charge-transfer resistance conceptually can not be negative. Consequently, the observed transfer of impedance into the second quadrant at lower frequencies in some potential regions must be due to a resistance related to adsorption and/or surface processes rather than a negative R_{ct}. Therefore, fitting to an impedance spectrum that proceeds into the second quadrant must be done to an equivalent circuit with a second time constant. We found in our corresponding work on methanol oxidation that a better fit was achieved without the charge-transfer resistance present, circuit L' (Figure 7) in the potential region where a negative slope in the polarization curve was obtained [63]. There is no reason why the

charge-transfer resistance should be neglected, but it is most probably not detectable in the fitting routine used, due to either a negligibly small value of the R_{ct} hidden in the high frequency region, or a very large value of the R_{ct} existing just as a small curvature in the CPE slope.

Positive-going sweep

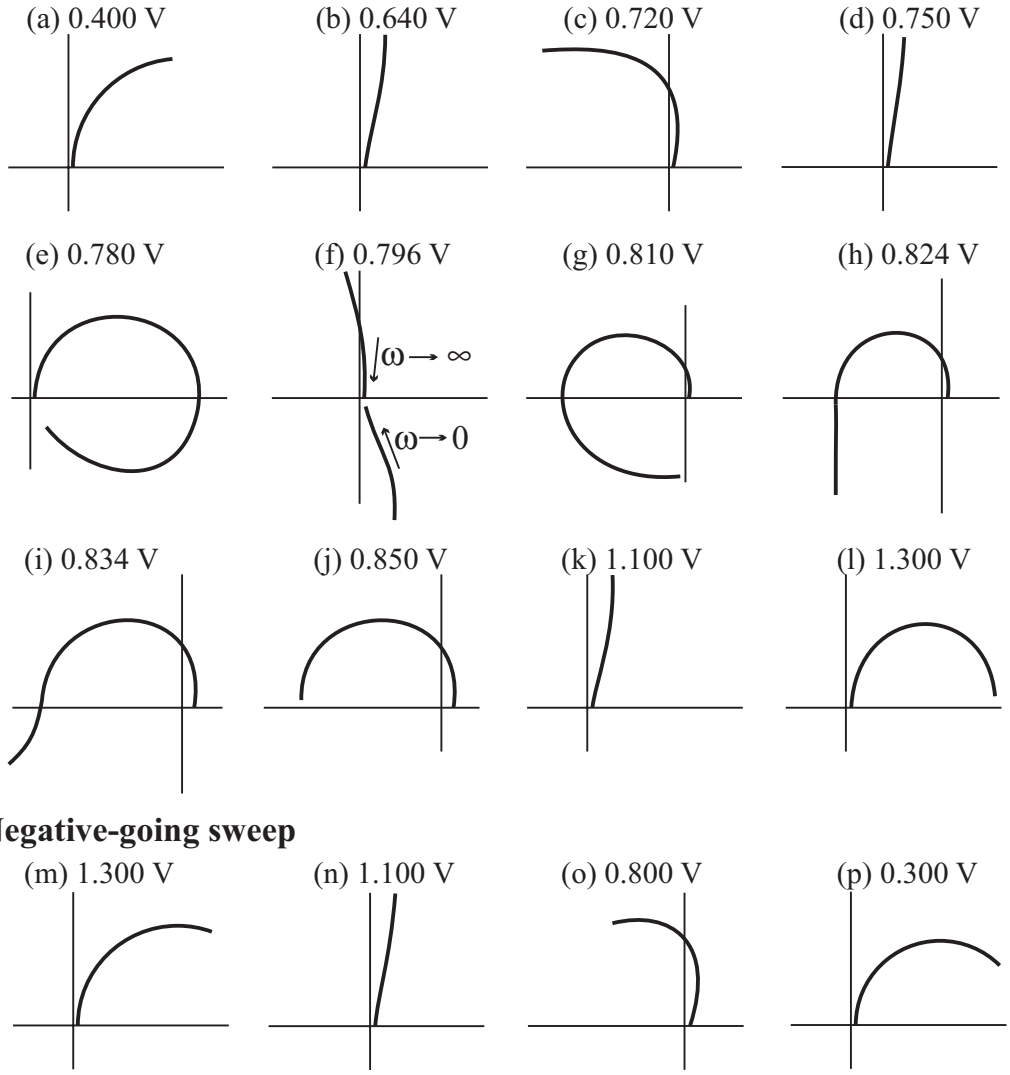

Negative-going sweep

Figure 6 Summary of the EIS behaviours found shown by Nyquist diagrams. (a)-(l) represent potentials in the positive-going scan; 0.400, 0.640, 0.720, 0.750, 0.780, 0.796, 0.810, 0.824, 0.834, 0.850, 1.100 and 1.300 V respectively, while (m)-(p) represent the negative-going scan; 1.300, 1.100, 0.800 and 0.300 V respectively.

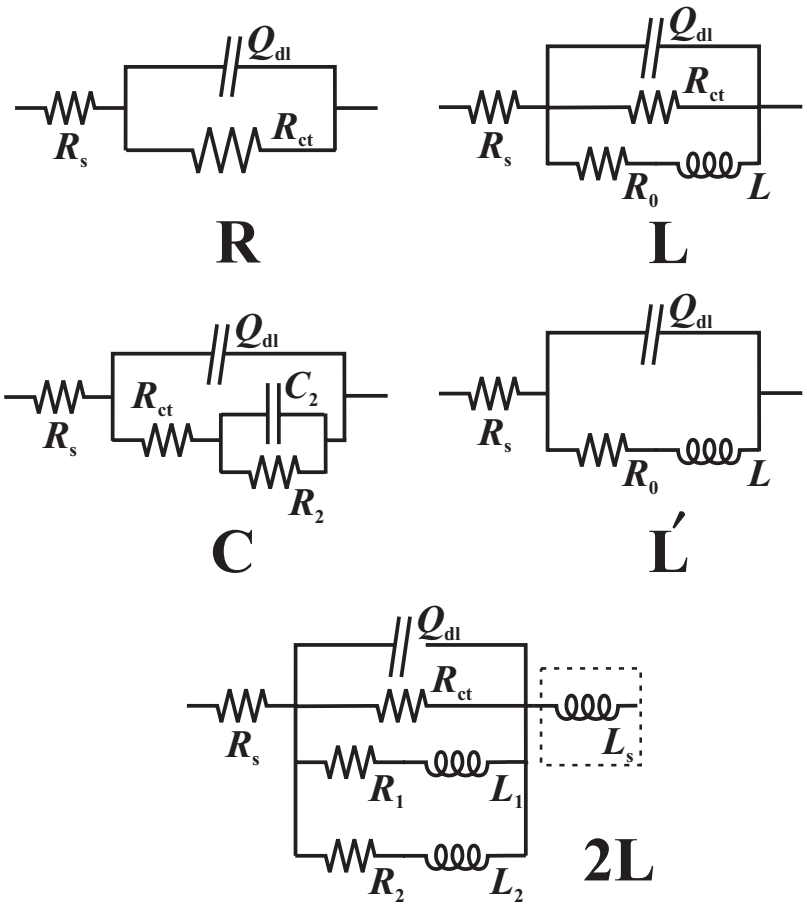

Figure 7 Equivalent circuits used in this work, where Q_{dl} implies a constant phase element (CPE) representing the double-layer. L_s (highlighted in circuit 2L) represents an optional inductor added in order to account for stray inductances in wiring etc., affecting the high-frequency regime. Fitting was primarily done without L_s, but in certain potential regions where negative real impedance was observed, fitting was remarkable easier with L_s present.

Positive-going sweep

Brief summary of the impedance spectra in the positive-going sweep are given in Figure 6a-l, revealing interesting features especially during the main oxidation peak. At lower potentials (less than 0.6 V), where the coverage of adsorbed poison still is assumed to be high, the Nyquist plot is just the beginning of a semicircle indicating that the impedance is best fitted to a parallel combination of the charge-transfer resistance and the double-layer

capacitance in series with the electrolyte resistance, circuit R. However, at the end of the hydrogen region (around 0.3 V), some process somehow interferes with the electrochemical process being studied, as clearly seen by a dip in phase in Figure 8, thus a more complicated equivalent circuit than R, like circuit L and C in Figure 7, can provide better fits to the high frequency points. Instead of over-interpreting this feature, the standard equivalent circuit R, was used even though the F-ratio test tended to contradict it.

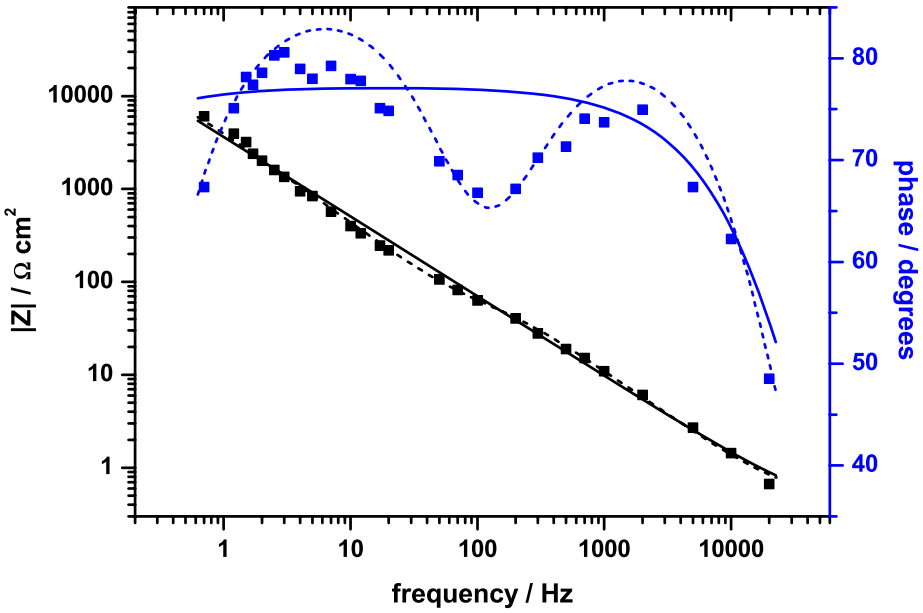

Figure 8 Bode plot at 0.270 V on positive-going sweep, showing a clear change in phase at about 100 Hz. Fits are shown for circuits R (solid lines), C (dashed lines). Fits to magnitude are harder to distinguish on this scale.

As the potential is further increased above 0.6 V, the current starts to increase at a faster pace, hence we are continuously observing a positive polarization slope in the quasi stationary voltammogram (Figure 1). Intuitively, zero frequency is just the d.c. signal and the resistance at zero frequency is expected to be related to the steady-state behaviour. The inverse of the slope of the steady state current-potential relationship is known as the polarization resistance, R_p, and EIS provides an easy way to measure it. An important application of this result is to decide whether all features have been captured in the experimental frequency range used or not. The apparent (extrapolated) low frequency intercept can be compared with the measured slope of the steady-state current potential curve, and if they match there is nothing significant missing at low frequencies. Of course if a reaction is so slow that it is missed by both

impedance and slow sweep measurements, then it is not detectable anyway. In this work we assume that the slow d.c. scan of 5 mV s^{-1} defines the quasi steady-state behaviour (Figure 1), and thus we expect a large R_p when the slope of the current-potential curve is zero. The current is continuously increased as the potential is slowly increased towards the main oxidation peak. The corresponding fitted value of the polarization resistance (resistance at zero frequency) is first increasing, but at potentials around 0.63 V it seems to tend to more negative values; in other words the impedance spectrum (in a Nyquist plot) and the fitted parameter values start to show the presence of second quadrant behaviour above this potential. In fact, in the potential region 0.632 V up to 0.750 V the fitted parameters indicate second quadrant behaviour with a negative zero frequency limit, even though the slope of the quasi steady-state curve is positive. This result clearly indicates that we are missing at least one relaxation in our impedance data. This is also visualized in Figure 5, where the real part of the admittance becomes negative in the potential region 0.69 to 0.74 V at a frequency of 3 Hz. Fitting to the impedance curves in this potential region was best done to circuit L' with negative R_0, or circuit R with negative R_{ct} (the former was preferred according to our definition of the charge-transfer resistance). In the potential region from 0.702 up to 0.75 V the circuit 2L was favoured by the statistical F-test. As we will see later for even more positive potentials, this observation is what has become known as hidden negative differential resistance (HNDR) and may play a crucial role in the dynamics and stability of the formic acid oxidation process at platinum electrodes.

At about 0.75 V the impedance curve is quickly flipping back to the first quadrant again, even including some fourth quadrant behaviour that indicates the influence of an inductor, and is best fitted with circuit L with all parameters positive. The fourth quadrant behaviour is further pronounced as the potential is increased into the potential region where initial formation of platinum oxide is expected. Figure 6e and Figure 9 (closed circles, right) clearly illustrates the fourth quadrant semicircle observed at 0.78 V. The impedance is getting very large at around 0.794 V and involves a sudden flip around this potential (Figure 6f) from being a clockwise loop at 0.794 V to be an anticlockwise loop at 0.796 V, proceeding into the second, third and even fourth quadrant. Experimental and fitted data before and after this flip is given in Figure 9 for 0.780 (circles, right) and 0.804 V (squares, left). Fitting to an equivalent circuit was impossible at 0.796 V, where the spectrum undergoes a drastic change. Intuitively, this behaviour must be related to the platinum oxide being formed. Oxide is observed at potentials above about 0.75 V without formic acid present, but is likely suppressed to higher potentials when formic acid is present.

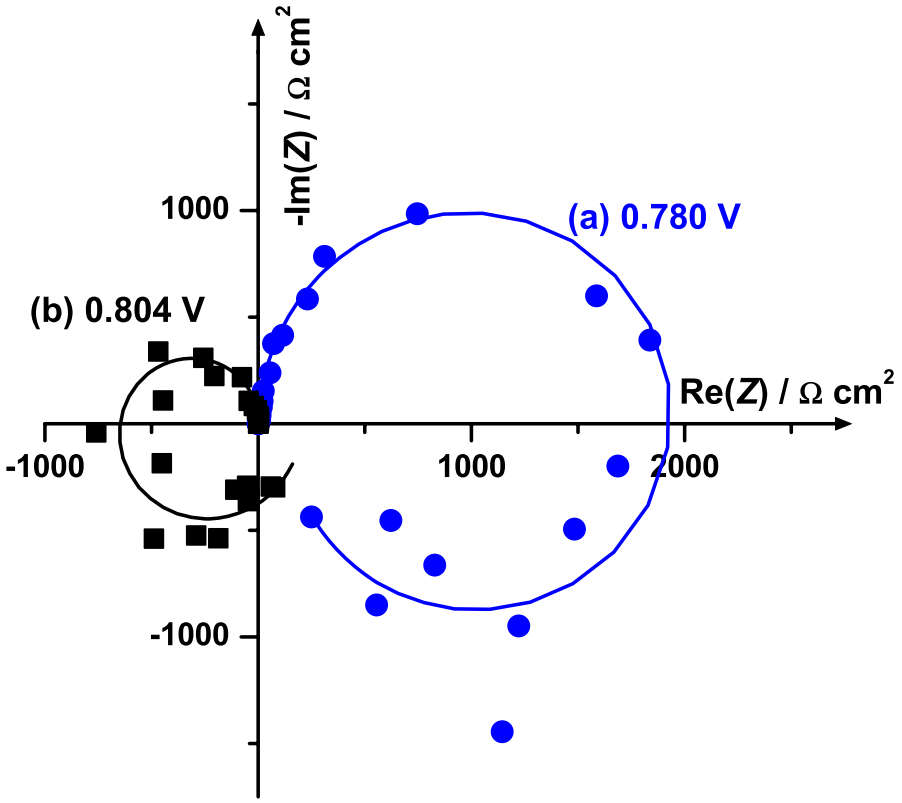

Figure 9 Nyquist plots before and after the abrupt change at 0.794/0.796 V showing qualitatively different impedance behaviour, a) 0.780 V (circles) and b) 0.804 V (squares). The solid lines represent the best fits.

As the potential is further increased, ultimately a high impedance at the main oxidation peak is expected. Unfortunately, since the experimental conditions do not allow for very low frequencies, it is hard to tell how the impedance spectra develops in this potential region, and a slight mismatch between the d.c. and a.c. data may occur. Nevertheless, a sign of a high impedance value is found at potentials just below 0.83 V, around 20 mV prior to the oxidation peak in the d.c. voltammogram. Figure 10 displays the Nyquist plots for the experimental and the corresponding fitted lines at several potentials, demonstrating how the impedance seems to move through a high impedance point at about 0.824 V ending up as just a semicircle in the second quadrant at 0.854 V (see also Figure 6g-j).

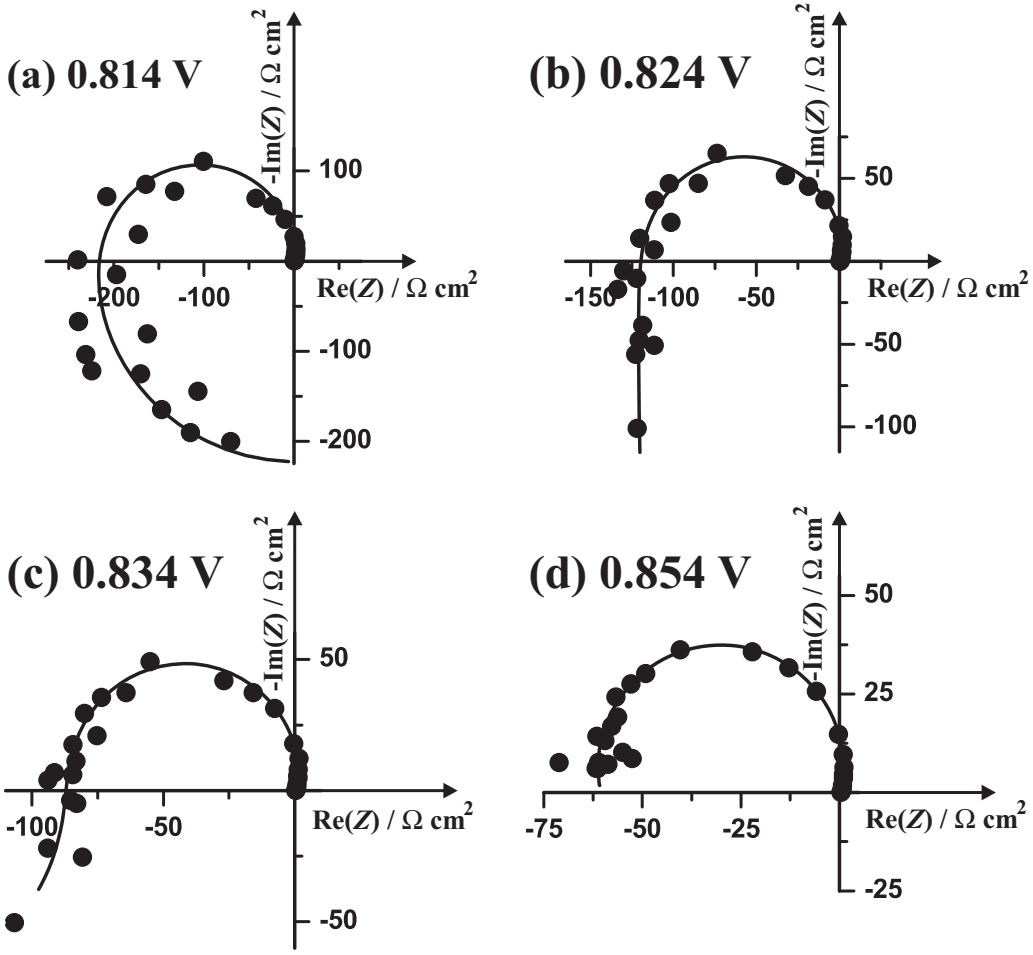

Figure 10 Nyquist plots of experimental data at (a) 0.814, (b) 0.824, (c) 0.834 and (d) 0.854 V in the positive-going sweep. The solid lines represent fits to the circuit 2L in the first three cases and to circuit L' for the latter.

Furthermore, at potentials above about 0.824 V, the impedance spectra tend to lead to a negative real value as the frequency goes to zero, thus indicating a negative slope in the polarization curve. Although this does not happen until about 0.85 V, a slight mismatch may exist between the a.c. and d.c. measurements, such that a negative slope should have been found in the true current/potential-slope at this slow sweep rate. Incidentally, increasing the potential some 20-30 mV to about 0.85 V, the measured impedance at the lowest frequencies clustered around the negative real axis without actually crossing it, giving no more than first and second quadrant behaviour. This must involve a transition from three relaxations to two relaxations, implying that the number of essential species in the mechanism can be reduced at this potential. This behaviour continues until the real part of the impedance turns positive

again, forcing the impedance spectrum to flip back to the first quadrant at about 1.13 V, roughly where we expect one complete monolayer of oxide to be formed. A single semicircle in the first quadrant is observed at the high potential end of the positive-going scan.

Negative-going sweep

Typical experimental and fitted impedance spectra from the negative-going sweep are given in Figure 11 for 1.400, 1.200, 0.750, and 0.400 V (brief summary of spectra are also given in Figure 6m-p). After reversing the potential, the impedance continues to show a single semicircle best fitted to circuit R. From about 1.25 V down to about 0.83 V only a fraction of the semicircle can be seen, and the estimated charge-transfer resistance is large. From 0.83 V down to about 0.63 V, the impedance spectrum proceeds into the second quadrant and is best fitted to circuit L' with negative R_0 and negative L (see Table 1 for fitting summary). However, potentials from about 0.72 V down to 0.56 V provide remarkably noisy impedance values for the lowest frequencies. The noise in the real and the imaginary parts of the impedance in this potential region is easily seen in the a.c. voltammogram for 3 Hz displayed in Figure 4. The oxidation peak in the d.c. voltammogram occurs at about 0.70 V. A negative real part of the impedance is observed for a broad range of frequencies at potentials where the voltammogram has a positive slope, suggesting that one or more relaxations are missed at these potentials. A positive slope indicates a positive value of the impedance as the frequency approach zero, and we conclude that we have a hidden negative differential resistance in at least one potential region in the negative-going scan. Once again, it should be pointed out that the measurements are not for a true steady-state.

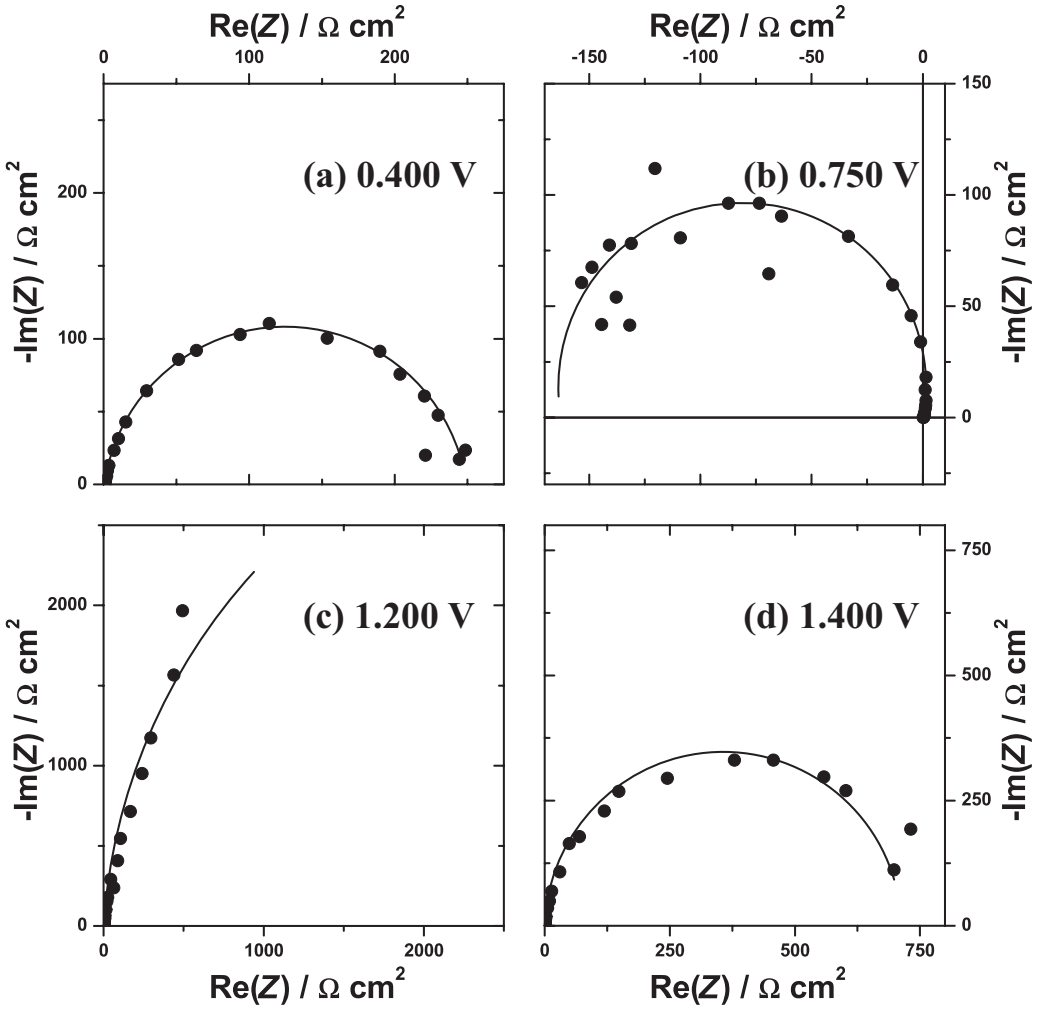

Figure 11 Selected impedance spectra for the reverse sweep. (a) 0.400, (b) 0.750, (c) 1.200 and (d) 1.400 V. The solid lines represent the fits to the selected equivalent circuit listed in Table 1.

Charge-transfer and double-layer parameters

Despite the possible influence of competitive surface processes as we move up to the first oxidation peak in the positive-going sweep, the charge-transfer resistance showed no discontinuities. A Tafel slope as high as 298 ± 4 mV dec^{-1} was found in the potential region from 0.30 V up to 0.50 V, as shown in Figure 12. Assuming a one-electron process this corresponds to an unexpectedly low symmetry factor (23 °C, $n = 1$, $\alpha = 0.20$).

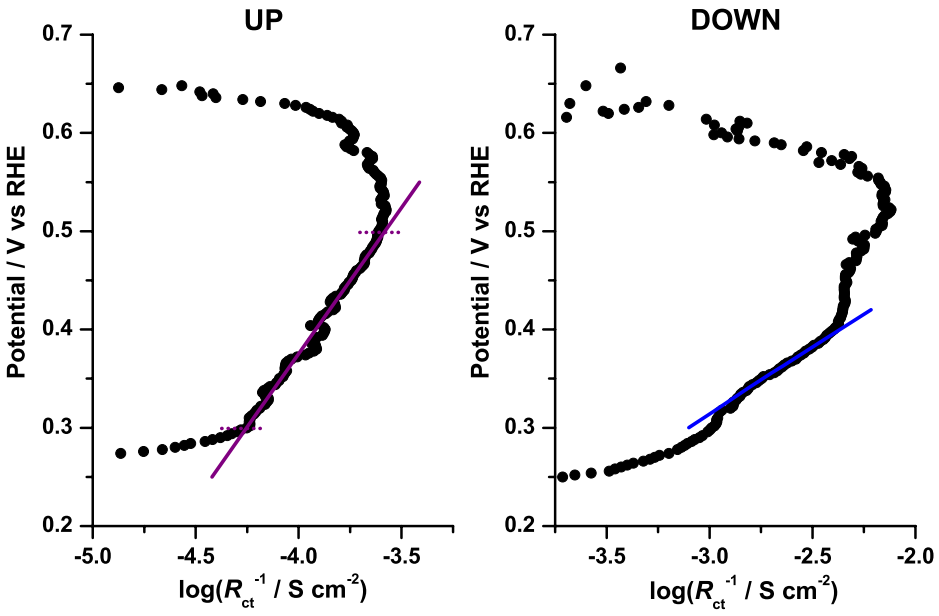

Figure 12 Tafel plots of R_{ct} for both forward and reverse sweeps, with regression lines displayed.

In the negative-going sweep it was harder to single out Tafel regions. In the narrow potential region of 0.34 – 0.39 V, a Tafel slope of 133 ± 2 mV dec^{-1} was found, indicating a rate determining step involving one electron (23 °C, α = 0.44). Clearly, the conditions are very different in the positive- and negative going sweeps. It is worth noticing that both the current and the double-layer capacitance are significantly higher in the Tafel potential region in the negative-going sweep compared to the positive-going sweep (Figure 1 and Figure 13).

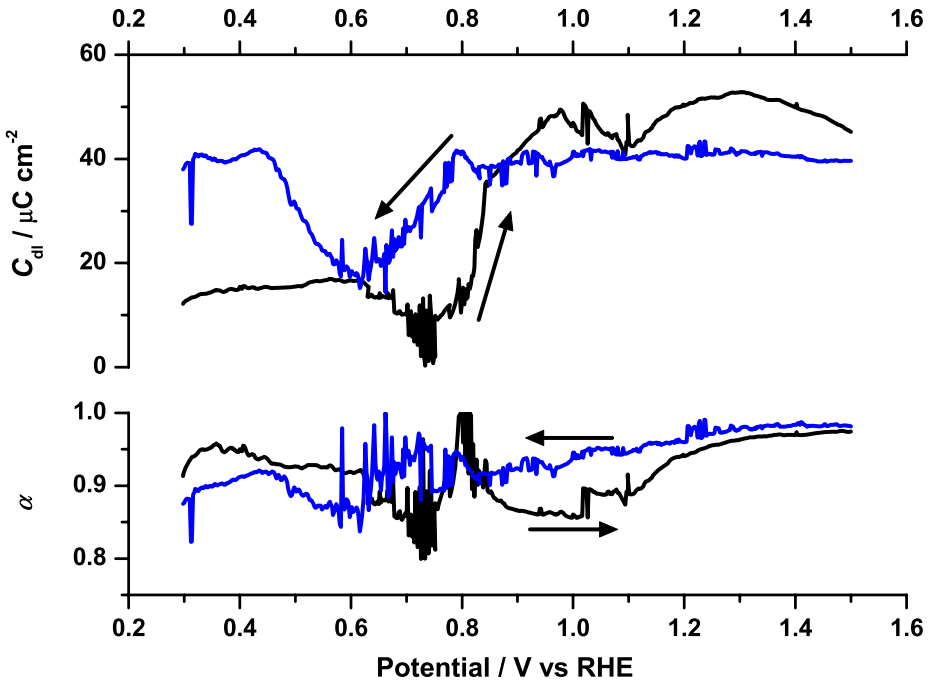

Figure 13 Double-layer capacitance (top) and CPE exponent α (bottom) from fits to all circuits in the forward and reverse sweeps.

The double-layer capacitance is extracted from the CPE parameters as $(QR^{1-\alpha})^{1/\alpha}$, where R is the parallel combination of R_s and R_{ct}. Usually R_s is much lower than R_{ct}, thus we approximate R to be just the ohmic resistance R_s in the calculations. Figure 13 shows the calculated double-layer capacitance and the corresponding CPE exponent α, for both forward and reverse sweeps. Clearly, the outline of the double-layer capacitance follows the imaginary part of the admittance for higher frequencies as expected (Figure 4). The double-layer capacitance values are similar, although slightly lower, to the double-layer capacitance values that we found in a similar experiment with methanol [63], except for low potentials in the reverse sweep, where formic acid interference leads to a significantly increased double-layer capacitance.

Table 1 Summary of fitting results

Potential region		Circuit	Comment	sign of $Z_{\omega=0}$	Sign of R_p
0.250-0.298	pos	C	dip in phase	+	+
0.300-0.630	pos	R		+	+
0.632-0.674	pos	L’	neg. R_0	-	+
0.676-0.700	pos	L’ + L_S	neg. R_0	-	+
0.702-0.750	pos	2L	neg. L_1 and R_1	-	+
0.752-0.776	pos	L	all positive	+	+
0.778-0.784	pos	2L	all positive	+	+
0.786-0.794	pos	2L	R_1 or R_2 neg.	-	+
0.796	pos	n/a	impossible to fit	n/a	n/a
0.798-0.840	pos	2L	neg. L_1 and R_1	+ early, - later	+
0.842-1.100	pos	L’	neg. L and R_0	-	-
1.102-1.500	pos	R		+	+
1.500-0.834	neg	R		+	+
0.832-0.636	neg	L’	neg. L and R_0	-	-
0.634-0.300	neg	R		+	+

Table 2 Theoretical values of the poles and zeroes

Circuit	Zeroes	Poles
C	$-(C_2(R_{ct}\|\|R_2))^{-1}$	negative and real, complicated
R	none	$-(C_{dl}R_{ct})^{-1}$
L	$-R_0/L$	complicated
L’	$-R_0/L$	negative and real for L>0, $C_{dl}R_0^2 > 4L$
L' + L_S	complicated	negative and real for L>0, $C_{dl}R_0^2 > 4L$
2L	$-R_1/L_1$, $-R_2/L_2$	complicated

Notes: The double-layer is assumed to be a pure capacitor for the purposes of these calculations. C_{dl} and R_{ct} are assumed to be positive. $R_{ct}\|\|R_2$ indicates the parallel combination of R_{ct} and R_2.

4.3.4 Oscillations and sign of zeroes of impedance

As discussed elsewhere [53,54,66], the critical potential of where the impedance curve crosses the negative real axis (i.e., crossing into the third quadrant; imaginary part of impedance becomes positive as the real part is negative) marks the galvanostatic transition to periodic behaviour (Hopf bifurcation). This behaviour starts at around 0.796 V and the Bode plots of experimental and fitted data at 0.814 V given in Figure 14 clearly demonstrate the sudden phase shift at 5 Hz from +180° to –180° as the impedance curve crosses the negative real axis. This frequency value of 5 Hz represents the intrinsic frequency of oscillation in the oxidation of formic acid on platinum at this potential.

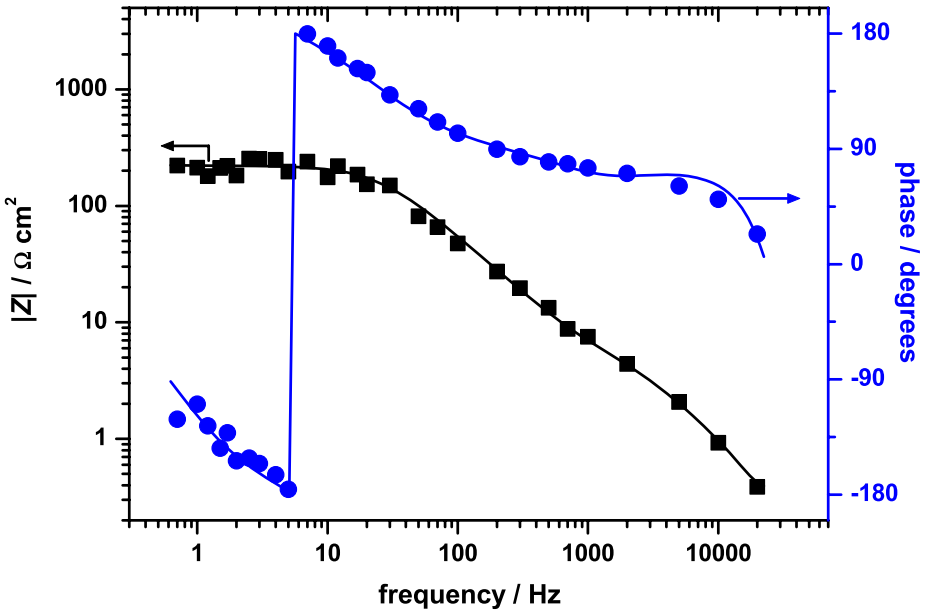

Figure 14 Bode plot at 0.814 V in the positive-going sweep direction illustrating the phase shift that gives evidence for third quadrant behaviour. The solid lines represent fits made to the equivalent circuit 2L with either L_1 and R_1, or L_2 and R_2 negative.

The negative real resistor value observed when the impedance curve crosses into the third quadrant is of importance. By adding an external resistance to the working electrode circuit of equal size, we can force the impedance curve to go through zero, which causes the system to be unstable and oscillate. According to the Nyquist plot of 0.814 V in Figure 10, adding a resistor of ca. 200 Ω cm^2

to the working electrode circuit forces the system to oscillate at this potential. Figure 9 predicts an even higher resistor value closer to the critical potential of 0.796 V. Examples of oscillations in the cyclic voltammogram are given in Figure 15 when external resistances of 2000, 3000 and 5000 Ω are added to the working electrode circuit. With a surface area of 0.1 cm^2 these resistors corresponds to resistor values where oscillations are expected. Figure 15d is corrected for the ohmic drop and suggests that the oscillations are initiated at potentials slightly below 0.75 V, and that the impedance curve indeed proceeds into the third quadrant in this potential region as proposed earlier. This happens at low frequencies, and as seen from Figure 15c,d for 5000 Ω, the intrinsic oscillation frequency is rather low (about 0.1 Hz), thus indicating a frequency for the phase shift lower than what is detectable in our experiments.

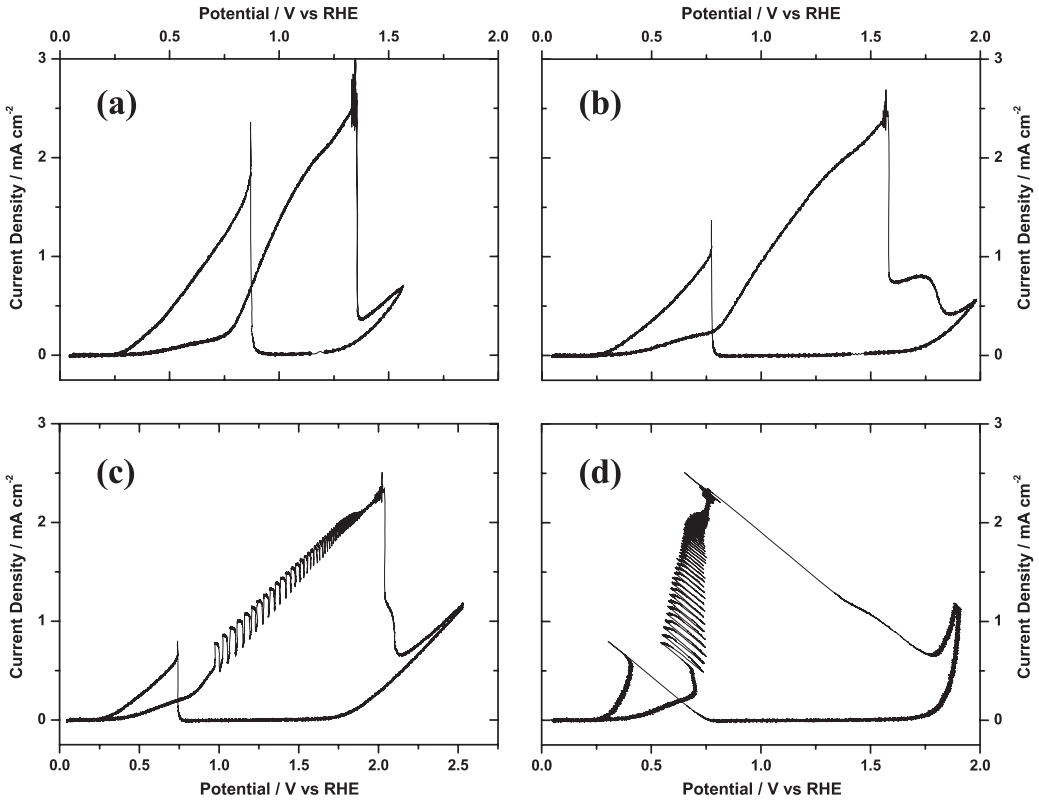

Figure 15 Cyclic voltammograms of electrooxidation of formic acid on platinum in sulphuric acid with various additional external resistors in the working electrode circuit; (a) 2000 Ω, (b) 3000 Ω, (c) 5000 Ω and (d) 5000 Ω after correcting for the ohmic potential drop (5000 Ω).

As discussed briefly already, it is impossible from our data to tell how many time constants that are changing sign, and when, in the potential region where

the adsorption of dissociated water in the electrolyte causes a HNDR to appear, i.e. in the potential region from 0.632 up to 0.75 V in the positive-going scan. This is due to the frequency limitation in our experiments that prevent us from detecting all relaxations in this potential region. It is also impossible to distinguish the time constants and map their behaviour in the noisy part in the negative-going scan. However, NDR and HNDR behaviours are indicated for the potential region 0.832-0.636 V in the reverse sweep, based on the fitting to the impedance curves and the a.c. and d.c. voltammograms. In these potential regions a simple equivalent circuit (normally L or L') implying only one kinetically significant adsorbed species model was used. However, it is most likely that a model for two kinetically-significant species should be used (e.g. circuit 2L), but this was not verified by the statistical F-test mainly due limitations and noise in the recorded data.

Potentials where one or more time constants are changing sign can in general easily be identified from a series of Nyquist plots as a function of potential. Clearly, the real part of a time constant becomes negative at a potential where the impedance spectra start to show second quadrant behaviour (negative real part of impedance). Circuits L and 2L comprise an easy relationship between the zeroes of impedance and time constants (Table 2). Circuit 2L gives the time constants directly as $\tau_1 = L_1/R_1$ and $\tau_2 = L_2/R_2$, with the zeroes given as $-\tau^{-1}$; a change in sign of one of the parameters L_1, R_1, L_2 or R_2 indicates a change in sign of one of the time constants (zeroes). The fitting summary is given in Table 1 and the theoretical values for the poles and zeroes for the different circuits are given in Table 2. The potential region 0.752-0.776 V proved to be difficult to fit. In this potential region the impedance curve bends back to the first quadrant and is best fitted to circuit L (circuit 2L does fit reasonably well to this potential region, but is not favoured by the statistical F-test). However, the likeliness of going from circuit 2L with two time constants to one time constant and back to two is low. Perhaps even though the sign of the extrapolated impedance equals the sign of the voltammetry curve the magnitude doesn't agree; there is a time constant missing and there really are two kinetically significant species on the surface.

Furthermore, the fitting results in Table 1 tell us that one time constant becomes negative at 0.786 V as one of the resistors, R_1 or R_2, becomes negative. Only some 10 mV later, a totally new impedance curve arises (Figure 6f,g), and indicates that one of the time constants (or zeroes) changes sign again. The two-variable model (circuit 2L) implies that one of the zeroes (impedance) goes through zero and yields a positive value indicating that a bifurcation occurs at this potential. However, it is impossible to tell whether it is the same time

constant/zero that becomes positive, due to the resistor becoming positive again simultaneously as the other inductor/resistor pair both become negative, or simply the matching inductor becoming negative at the flip-potential causing the corresponding time constant to be positive again. Intuitively it is more likely that one parameter changes sign than three, so the latter would be more plausible, but concluding this from the impedance alone is impossible since the impedance value is a function of all four parameters.

4.4 Discussion

4.4.1 Mechanism of formic acid oxidation

The mechanism of formic acid at platinum electrodes in acid solution is reasonably well established as the so-called dual pathway mechanism, originally proposed by Capon and Parsons [1,8,9]. These authors suggested that the initial adsorption of formic acid leads to formation of the highly reactive intermediate $COOH_{ads}$ which immediately oxidizes further to CO_2. This reaction is the main current contributor comprising of two consecutive one-electron charge-transfer reaction steps (dehydrogenations), and is referred to as the direct path, equations (4) and (5):

$$\mathrm{Pt(site)} + \mathrm{HCOOH} \rightleftarrows \mathrm{Pt-HCOOH} \tag{3}$$

$$\mathrm{Pt-HCOOH} + \mathrm{Pt(site)} \rightarrow \mathrm{Pt-COOH} + \mathrm{Pt-H} \tag{4}$$

$$\mathrm{Pt-COOH} \rightarrow \mathrm{Pt-H} + \mathrm{CO_2} \tag{5}$$

The rate of reaction (5) is clearly very fast since radical species are involved, however reaction (3) may be of comparable rate to reaction (4) depending on diffusion, concentration and available sites. The oxidation of hydrogen radicals is very fast at elevated potentials, where we encounter significant oxidation of formic acid, and is normally not taken into consideration. Even so, it is important to keep in mind that every dehydrogenation step requires a neighbouring free surface site (reaction (4)). The adsorbed hydrogen atom is then desorbed (oxidized) according to reaction (6):

$$\mathrm{Pt-H} \rightarrow \mathrm{Pt(site)} + \mathrm{H^+} + \mathrm{e^-} \tag{6}$$

Despite the fact that reaction (6) is fast at potentials of interest, there are many possible reactions that might constitute part of the direct path, for example the suggested reaction of Capon and Parsons [9]:

$$HCOOH + Pt - H \rightarrow Pt - COOH + H_2 \quad (7)$$

Even though the simplicity of the formic acid molecule suggests that oxidation easily should lead to CO_2 as the final oxidation product, the dual path mechanism postulates an indirect path involving a stable intermediate that blocks the surface and inhibits further adsorption of formic acid molecules. Experimental evidence has been presented for several different candidates for the poisoning species, including HCO_{ads} and CO_{ads}, with indications of formation of more than one strongly bound intermediate [2] and references therein. However, general agreement on CO_{ads} as the poisoning species has been made based on in-situ IR spectrometry [2,67]. Therefore, in order to present a reasonable condensed mechanism and descriptions, it is convenient to consider that CO_{ads} is indeed the only strongly bound intermediate formed directly from adsorbed formic acid:

$$Pt - HCOOH \rightarrow Pt - CO + H_2O \quad (8)$$

Parsons and VanderNoot [2] suggested that the first step in the poison formation involves the cleavage of the C-OH bond in formic acid which is suggested by isotope labelling and DEMS measurements [68] thus forming HCO_{ads} which is further oxidized to CO_{ads}. The direct oxidation was found to occur without the loss of oxygen, making the dual path mechanism obvious. In addition, the strongly bound species was found to not exchange oxygen with water, and further oxidation to CO_2 showed that only one oxygen atom comes from the parent molecule. However, this is by no means conclusive since they also point out that the isotopically-labelled oxygen was readily exchanged with oxygen atoms in the water molecules in the electrolyte. Kunimatsu and Kita [69] proposed two reactions leading to the formation of adsorbed CO, in addition to direct formation from adsorbed formic acid, reaction (8), as suggested by, for example Sun et al. [70]:

$$Pt - COOH + Pt - H \rightarrow Pt - CO + Pt(site) + H_2O \quad (9)$$

$$2Pt - COOH \rightarrow Pt - CO + Pt(site) + CO_2 + H_2O \quad (10)$$

The formation of poison is most likely not an electrochemical step since the oxidation state of the carbon is the same, +2, in HCOOH and CO. Therefore it is most likely that a potential dependent reaction like formation of adsorbed OH from water is dominating the poison formation at elevated potentials. Adsorbed hydroxide appears at about 0.5 V through water dissociation at a Pt(111) electrode in perchloric acid, as demonstrated by Iwasita and Xia [71]):

$$Pt(site) + H_2O \rightarrow Pt - OH + H^+ + e^- \quad (11)$$

Platinum oxide is as usual formed at potentials above 0.75 V, although the presence of formic acid slightly shifts this potential to more positive values:

$$\mathrm{Pt(site)} + \mathrm{H_2O} \rightarrow \mathrm{PtO} + 2\mathrm{H^+} + 2\mathrm{e^-} \quad (12)$$

The removal of the catalytic poison CO_{ads} proceeds through an electrochemical reaction with an oxygen containing (donor) species at the surface, e.g. surface oxide or dissociated water, according to the following steps:

$$\mathrm{Pt-CO} + \mathrm{Pt-OH} \rightarrow 2\mathrm{Pt(site)} + \mathrm{CO_2} + \mathrm{H^+} + \mathrm{e^-} \quad (13)$$

$$\mathrm{Pt-CO} + \mathrm{PtO} \rightarrow 2\mathrm{Pt(site)} + \mathrm{CO_2} \quad (14)$$

Reactions (8), (11) and (13) (or (8), (12) and (14)) constitutes what is usually referred to as the indirect path to CO_2 in the formic acid oxidation reaction. The competition of available sites and coverage of species are important and essential in the discussion of kinetically significant species. In formic acid it was found by employing a step/cycle potential program, that the rate of CO adsorption is decreasing with potential, hence a negative Tafel slope of about -110 mV dec^{-1} was found [72].

The fact that CO does not oxidize until about 0.5 V means that at lower potentials, where a practical anode operates in a fuel cell, CO will effectively poison the electrode by blocking active sites without being removed. Therefore it is of importance to either prevent the formation of adsorbed CO, catalyze its oxidation at lower potential by for example employing binary catalysts, or add species to the electrolyte that scavenge and oxidize the adsorbed CO.

Simplified Reaction Mechanism

Our simplified mechanism builds on the mechanistic model of Strasser et al. [41] with some extra simplifications. The mass transport of formic acid is ignored, as well as the "essential" role of potential. For the direct pathway we combine the adsorption of formic acid and its rapid desorption to give a net reaction (reaction (15)). However, it is important to be aware that the limiting step in reaction (15) is a one electron process leading to the formation of the highly reactive species $COOH_{ads}$. Reactions (16)-(18) forms the indirect parallel pathway and play a crucial role in formic acid kinetics even at elevated potentials where the reaction rates of reactions (16) and (18) are slow compared to the rate of reaction (17). To make our mechanism as simple and condensed as possible we assume that each adsorbate occupies one surface platinum site,

although this could be modified for more complicated stoichiometries if needed.

$$\mathrm{Pt(site) + HCOOH \xrightarrow[\text{fast}]{v_{\text{direct}}} Pt(site) + CO_2 + 2H^+ + 2e^-} \tag{15}$$

$$\mathrm{Pt(site) + HCOOH \xrightarrow[\text{slow}]{v_{\text{CO}}} Pt - CO + H_2O} \tag{16}$$

$$\mathrm{Pt(site) + H_2O \xrightarrow[\text{fast}]{v_{\text{OH}}} Pt - OH + H^+ + e^-} \tag{17}$$

$$\mathrm{Pt - CO + Pt - OH \xrightarrow[\text{slow}]{v_{CO_2}} 2Pt(site) + CO_2 + H^+ + e^-} \tag{18}$$

The simplified mechanism should be appropriate for the potential region prior to the voltammetric peak in the positive-going scan. As discussed above, two regions of negative impedance behaviour are separated by a small potential region that exhibits positive real impedance values (at least for the frequencies measurable in our experiments) in the positive slope of the quasi steady-state polarization curve. A possible explanation would be to assume that the coverage of OH_{ads} has reached its maximum at potentials close to 0.75 V, which, together with adsorbed CO, is an incomplete coverage of the surface. As a result, one can have islands of CO, OH and a direct path intermediate (if the direct path is limited by desorption), or more likely, free surface sites (if the direct path is limited by adsorption). Consequently, when continuing the anodic polarization (above 0.75 V), the rate of the direct path may be substantially increased at the free surface sites leading to a positive real part of impedance despite the blocking feature of OH_{ads} and CO_{ads}. Introducing more than one kinetically-significant species leads to various ways that they can dominate in different potential regions.

Determination of kinetically significant species

In distinct potential regions, the complexity of the impedance data, and our definition of the charge-transfer resistance, indicates three relaxations implying that a more complicated equivalent circuit than R, L or C is needed to give acceptable fits to the experimental data. 2L is one such equivalent circuit that can be used to fit systems that involve two kinetically significant species. From the summary of fitting, Table 1, we expect two time constants to appear (circuit 2L) in the potential regions where we have additional surface species to adsorbed CO. This could be adsorbed OH from the dissociation of water (or some sort of surface bonded water) at potentials prior to the platinum oxide formation. It has been found that platinum oxide formation commences at 0.75 V in blank electrolyte and that oxygen-containing species on the surface are

present already at 0.5 V in blank electrolyte [71]. These potentials are most likely shifted to higher values with the presence of a fairly high formic acid concentration. Based on the fitting results we assume therefore that at low potentials, where we have only circuits with one time constant, then we have either CO on the surface nearly saturated with the rest OH, or on the return sweep, free surface sites with oxide. In either case one variable describes the surface state (e.g. θ_{OH}) and we have only one kinetically significant species, one time constant, and one zero. The direct path is not affecting this argument if the desorption is fast. Consequently, at high potentials, we have only CO and one oxygen-donating species at the surface, and again one variable suffices. However, in the middle potential region, presumably we have CO_{ads}, OH_{ads} and free surface sites introducing the necessity of having two significant variables which demands a more complex equivalent circuit (2L) to be used. Interestingly, within the latter potential region, apparently only one time constant exists, based on which circuit provides the better fit. Although it fits better and has the same sign of the extrapolated impedance as the slope of the quasi steady-state polarization curve, the magnitude doesn't agree and the missing relaxation is associated with a second kinetically significant species on the surface.

4.4.2 Tafel behaviour

Lu et al. [73] sampled the current data at 0.5 seconds after the potential step in order to evaluate the activation parameters. A specific delay of 0.5 seconds was chosen to avoid double-layer charging effects and to avoid a large amount of CO adsorbed on the catalyst surface (however, the presence of some adsorbed CO at a delay of 0.5 seconds is expected). Furthermore, they report the maximum activity to be achieved at 0.57 V and that the observed Tafel behaviour (133 mV dec^{-1}, at ca. 0.2 - 0.35 V) suggested the deceleration of the oxidation reaction to begin at potentials lower than 0.4 V. The deceleration was proposed to be due to the decrease in electrochemical driving force favouring the oxidation but also hydrogen adsorption. In fact, a negative Tafel slope of -110 mV dec^{-1} was found for the formation of adsorbed CO [72].

Our data are based on collecting impedance data from adding a small-amplitude a.c. signal onto a slow d.c. ramp. The logarithm of the inverse charge-transfer resistance (determined by fitting of the impedance data to an equivalent circuit) is then plotted to search for Tafel-like behaviour in both the negative- and positive-going scan. First of all, the charge-transfer resistance shows Tafel-like behaviour in the potential region 0.30 V to 0.50 V in the positive-going scan

with a slope of 298 ± 4 mV dec^{-1} perhaps suggesting a one-electron process with an unexpectedly low value of the symmetry factor (23 °C, $n = 1$, $\alpha = 0.20$). In the negative-going scan, the R_{ct} in our data displayed Tafel behaviour in the narrow potential region between 0.34 and 0.39 V with a Tafel slope of 133 ± 2 mV dec^{-1}, which is similar to the Tafel slope found by Lu et al. [73], and indicates that the rate determining step involves the transfer of one electron (23 °C, $\alpha = 0.44$).

The surface conditions for oxidation in the potential region 0.35 and 0.7 V are different for the positive- and negative-going scans: (i) there is a saturated layer of CO in the positive scan, (ii) hydrogen adsorption and desorption has occurred prior to the positive-going scan, and (iii) there is freshly reduced platinum surface in the negative-going scan without interference of upd hydrogen. Since Lu et al. [73] are measuring the current in potential step measurements after potentially cleaning the surface and subsequently waiting 0.5 seconds at the final potential, thus allowing only a small amount of CO_{ads} to be formed, it is more likely that their potential/current characteristics are more closely related to the features in the negative-going scan, i.e. oxidation on freshly reduced platinum and a partially covered surface without upd hydrogen interference. Since the rate of formation of CO is increased as the potential is lowered, stepping to a more negative potential leads to more CO on the surface, which is also true when sweeping in the negative direction. Intuitively, the Tafel behaviour should reflect the same rate determining process in both cases. Lu et al. [73] conclude that the deviation from Tafel behaviour at higher potentials is due to the decay in oxidation current caused by surface poisoning; the decay is a function of surface CO coverage. CO blocking formation does not involve electron transfer according to reaction (8).

The Tafel measurement suggests that in the negative-going sweep, the formation of adsorbed CO is eventually not further oxidized, thus a passivation due to blockage by adsorbed CO occurs. Just before entering the hydrogen region, a Tafel region was observed that indicates a rate determining step involving one electron. Drawing conclusions directly from the Tafel slopes itself is coarse and needs substantial support from other studies. The positive-going sweep presents a fairly high Tafel slope in the potential region where almost no current is observed. This may indicate that the rate limiting process is the direct oxidation of formic acid to CO_2 at a surface covered with CO. In addition, the sweep rate dependences (Figure 2 and Figure 3) of the oxidation peaks suggest that different processes are rate limiting in the forward and reverse sweeps, but as the Tafel behaviours show, both involve a one-electron process as the rate determining step.

4.4.3 Prediction of instabilities and chemical oscillations

So, if we consider three species on the surface, CO, OH and X, where X will be thought of as free surface sites in line with the idea that formic acid adsorption is much slower than desorption, we can write the area of X as 1- θ_{CO} - θ_{OH}, giving two independent variables (presumably oxide rather than OH works in a similar way). Neglecting the role of the potential for the moment, we want to investigate the signs of the eigenvalues of the Jacobian matrix that is characteristic of the simplified mechanism. In general, the component of the Jacobian matrix for step *j* is:

$$J_j = -A_j = \begin{bmatrix} n_{1j} \\ n_{2j} \end{bmatrix} \begin{bmatrix} \frac{\partial v_j}{\partial \theta_1} & \frac{\partial v_j}{\partial \theta_2} \end{bmatrix} \tag{19}$$

(Here, A_j is the elementary matrix defined in the theory of Harrington and co-workers [74,75].) Assuming Langmuir kinetics and species order CO, OH then:

$$J_{CO_2} = -A_{CO_2} = \begin{bmatrix} -1 \\ -1 \end{bmatrix} \begin{bmatrix} + & + \end{bmatrix} = \begin{bmatrix} - & - \\ - & - \end{bmatrix} \tag{20}$$

The two plus signs reflects the fact that increasing the coverage of CO or OH increases the rate of this step, reaction (18). Considering this step only and using the fact that the matrix has rank 1, the eigenvalues are zero and a real negative number that is the sum of the two diagonal entries. The absence of any non-negative real parts to the eigenvalues means the matrix is stable. These eigenvalues are the zeroes of the impedance, assuming reaction (18) to be the only step. Intuitively, adding some CO or OH increases this reaction rate consequently removing some CO or OH and tending to return the coverage back to where it was. Now we couple this with the CO_{ads} production from formic acid:

$$J_{CO} = -A_{CO} = \begin{bmatrix} +1 \\ 0 \end{bmatrix} \begin{bmatrix} - & - \end{bmatrix} = \begin{bmatrix} - & - \\ 0 & 0 \end{bmatrix} \tag{21}$$

, where formation of adsorbed CO decreases the rate of the reaction through blockage of surface sites. Likewise for the OH adsorption:

$$J_{OH} = -A_{OH} = \begin{bmatrix} 0 \\ +1 \end{bmatrix} \begin{bmatrix} - & - \end{bmatrix} = \begin{bmatrix} 0 & 0 \\ - & - \end{bmatrix} \tag{22}$$

All these matrices can then be added together with the result of a 2x2 matrix (no longer rank 1) with all negative signs. The sum of the eigenvalues is the sum of the diagonal elements and the product is the determinant of the matrix:

$$J = \begin{bmatrix} \partial r_{CO}/\partial\theta_{CO} & \partial r_{CO}/\partial\theta_{OH} \\ \partial r_{OH}/\partial\theta_{CO} & \partial r_{OH}/\partial\theta_{OH} \end{bmatrix} = \begin{bmatrix} -k_{CO} - k_{CO_2}\theta_{OH} & -k_{CO} - k_{CO_2}\theta_{CO} \\ -k_{OH} - k_{CO_2}\theta_{OH} & -k_{OH} - k_{CO_2}\theta_{CO} \end{bmatrix} \quad (23)$$

, where r_{CO} and r_{OH} are the net rates of formation of CO_{ads} and OH_{ads} respectively.

Experimental results have shown that the adsorption rate of CO from formic acid is very slow at potentials of interest, e.g. [73], thus the first row elements on the right hand side of the equation (23), can be simplified by neglecting the first term, k_{CO}. This matrix can have a positive eigenvalue (e.g. for θ_{OH} = 0.25, θ_{CO} = 0.5, k_{CO_2} = 1 and k_{OH} = 2 the eigenvalues are 0.17 and -2.92). To predict whether a positive eigenvalue will occur requires a detailed model of the kinetics and in particular the coverages as a function of potential. Supposing nucleation-growth and collision (NGC) behaviour with OH_{ads} islands in a sea of CO_{ads}, we might expect that $\partial v_{CO_2}/\partial\theta_{OH}$ is positive (equation (20)) in the early stages and negative in the later stages. The desired knowledge in this context, in order to predict instabilities and oscillatory behaviour, is to be able to map the eigenvalues as a function of potential. Note that the off-diagonal elements must have opposite signs in order to get complex eigenvalues. Complex eigenvalues for this 2x2 matrix are a prerequisite for the chemical part of the mechanism to have a Hopf bifurcation. The simplified version of the direct path, reaction (15), does not affect the coverage of either CO_{ads} or OH_{ads}, has zero stoichiometric coefficients for these species, and does not contribute to the 2x2 Jacobian matrix. However, it will appear in the 3x3 matrix that arises when potential is considered.

Looking at our experimental results, in the potential region where we have two time constants (circuit 2L) we have a 2x2 matrix as discussed above. From the summary tables (Table 1 and Table 2), all the time constants are real (although they might go complex at 0.796 V) implying that the two off-diagonal elements can not have opposite signs for any potentials which exhibit two time constants (aside from the double-layer/charge-transfer relaxation). Any sort of sign pattern would narrow down to two possibilities; one negative and one positive, or two negative zeroes. The most likely scenario in our experiments is that both are normally negative and then one goes positive leading to a sudden instability, where the surface just quickly becomes covered with OH_{ads} (or oxide). On poly-crystalline platinum, the slowness of the oxide process probably modifies the extremeness of the behaviour, which sharpens up and leads to a more vertical transition when adding an external resistor. We conclude that because no complex zeroes were observed in the formic acid oxidation on polycrystalline

platinum (with reservations for 0.796 V), we can eliminate the possibility that oscillations arise from purely chemical reasons. Any oscillations cannot be purely potentiostatic and must involve the potential as an essential variable.

Oscillations in the oxidation of formic acid

Although purely potentiostatic oscillations are precluded according to our impedance results, adding an external resistor to the working electrode circuit makes it impossible to eliminate the potential at the surface, and oscillations may be possible. A 3x3 Jacobian matrix which explicitly includes potential is required, and deducing the nature of the eigenvalues from sign considerations is much more complicated. Therefore we adopted an experimental approach. Figure 15 shows oscillatory behaviour in the formic acid oxidation on platinum in sulphuric acid at room temperature by applying external resistors in the working electrode circuit. The oscillations occur in the rising part of the voltammogram shutting off instantaneously at the current peak. Oscillations were only observed in the positive-going scan with the selected resistors. The absence of oscillations in the negative-going scan may be explained by the potential being too low after reactivation (oxide reduction) for oscillations to occur, due to the high ohmic drop. However, Strasser and co-workers [40,76] were able to observe oscillatory behaviour in the negative-going scan by stopping the sweep after reactivation. Oscillations were found for potentials in the cathodic sweep at 0.70 and 0.763 V in 0.05 M formic acid and 1 mM perchloric acid on a Pt(100) single crystal [76].

As long as the experimental results show that the impedance does not go to zero at a finite frequency ω_H (without an external resistor), we know that there are no complex zeroes, since otherwise $i\omega_H$ would be a complex zero, and the system would oscillate without adding an external resistor. Taking the interfacial part of the impedance and adding a resistor moves all the zeroes (although not the poles) and any deductions made about the zeroes in the previous section need to be modified. The zeroes of the interfacial potential are important in determining the nature of the mechanism, but are less useful for predicting oscillations.

The study of oscillations is nonetheless interesting and may provide useful in some context. Schell et al. [77] found that in the periodically driven system more formic acid follows the direct route than in the unperturbed system even though the average current applied was the same. This demonstrates that nonlinear processes may lead to beneficial effects for the efficiency of electrochemical processes.

4.5 Conclusions

Collection of EIS spectra during a slow sweep shows a variety of spectral types and allows for direct correlation with the features of a d.c. voltammogram, aiding in the interpretation. Potential regions of negative impedance and hidden negative impedance behaviour were observed and related to the formation of surface species. One kinetically significant species was indicated at low potentials and potentials higher than the main voltammetric peak At potentials prior to the voltammetric peak, two relaxation times were observed (aside from the double-layer/charge-transfer relaxation), which is evident for two kinetically significant species, assumed to be OH_{ads}, and CO_{ads}. That is, the kinetics are determined once the coverages of these two species are given. Negative differential resistance is observed in the potential regions that possess a negative d.c. polarization slope and arises because the predominant formation of surface oxide inhibits the oxidation of formic acid. Two potential regions with hidden negative differential resistance behaviour were identified in the positive-going sweep, one prior to platinum oxide formation at about 0.63-0.75 V (assumed to involve adsorbed dissociated water, OH_{ads}), and one just negative of the main oxidation peak (assumed to involve Pt oxide).

An equivalent circuit with two well-defined zeroes of impedance was employed in the potential regions with two kinetically-significant species. Our fitted data showed no complex zeroes, thus eliminating the possibility that oscillations arise from purely chemical reasons. In other words, no purely potentiostatic oscillations can occur in the formic acid oxidation on polycrystalline platinum at the operating conditions used here. Adding an external resistor to the working electrode circuit makes the potential an essential variable, and led to oscillatory behaviour under conditions that could be predicted from the impedance spectra.

4.6 Acknowledgements

F.S thanks the Norwegian Research Council for the award of a scholarship. We greatly appreciate the financial support from the Sciences and Engineering Research Canada, the University of Victoria and the Norwegian University of Science and Technology.

References

[1] A. Capon, R. Parsons, *J. Electroanal. Chem.*, **44** (1973) 1

[2] R. Parsons, T. VanderNoot, *J. Electroanal. Chem.*, **257** (1988) 9

[3] T.D. Jarvi, E.M. Stuve, in: *Electrocatalysis*, J. Lipkowski, P.N. Ross (Eds.), Wiley-VCH, New York, 1998, pp. 75-154

[4] S.-G. Sun, in: *Electrocatalysis*, J. Lipkowski, P.N. Ross (Eds.), Wiley-VCH, New York, 1998, pp. 243-291

[5] W. Vielstich, in: *Encyclopedia of Electrochemistry*, A.J. Bard, M. Stratmann (Eds.), *Vol 2*, Wiley-VCH Verlag GmbH & Co, Weinheim, 2003, pp. 466-511

[6] a) E. Leiva, C. Sánchez, in: *Handbook of Fuel Cells - Fundamentals, Technology and Applications*, W. Vielstich, H.A. Gasteiger, A. Lamm (Eds.), *Vol 2 Electrocatalysis*, John Wiley & Sons, Chichester, 2003, pp. 47-61. b) C. Sánchez, E. Leiva, in: *Handbook of Fuel Cells - Fundamentals, Technology and Applications*, W. Vielstich, H.A. Gasteiger, A. Lamm (Eds.), *Vol 2 Electrocatalysis*, John Wiley & Sons, Chichester, 2003, pp. 93-131

[7] J.M. Feliu, E. Herrero, in: *Handbook of Fuel Cells - Fundamentals, Technology and Applications*, W. Vielstich, H.A. Gasteiger, A. Lamm (Eds.), *Vol 2 Electrocatalysis*, John Wiley & Sons, Chichester, 2003, pp. 625-634

[8] A. Capon, R. Parsons, *J. Electroanal. Chem.*, **44** (1973) 239

[9] A. Capon, R. Parsons, *J. Electroanal. Chem.*, **45** (1973) 205

[10] H. Degn, *J. Chem. Soc. Faraday Trans.*, **64** (1968) 1348

[11] P. Russel, J.S. Newman, *J. Electrochem. Soc.*, **133** (1986) 2093

[13] T.G.J. Van Venrooij, M.T.M. Koper, *Electrochim. Acta*, **40** (1995) 1689

[12] N. Fetner, J.L. Hudson, *J. Phys. Chem.*, **94** (1990) 6506

[14] M. Thalinger, M. Volmer, *Z. Phys. Chem.*, **150** (1930) 401

[15] D.T. Sawyer, E.T. Seo, *J. Electroanal. Chem.*, **5** (1963) 23

[16] B.E. Conway, D.M. Novak, *J. Phys. Chem.*, **81** (1977) 1459

[17] G. Horányi, C. Visy, *J. Electroanal. Chem.*, **103** (1979) 353

[18] W. Wolf, M. Lübke, M.T.M. Koper, K. Krischer, M. Eiswirth, G. Ertl, *J. Electroanal. Chem.*, **399** (1995) 185

[19] M.T.M. Koper, T.J. Schmidt, N.M. Markovic, P.N. Ross, *J. Phys. Chem. B*, **105** (2001) 8381

[20] D.C. Azevedo, A.L.N. Pinheiro, E.R. Gonzalez, *Electrochem. Solid St.*, **5** (2002) A51

[21] S. Malkhandi, A. Bonnefont, K. Krischer, *Electrochem. Commun.*, **7** (2005) 710

[22] M. Schell, F.N. Albahadily, J. Safar, Y.H. Xu, *J. Phys. Chem.*, **93** (1989) 4806

[23] M. Hachkar, M. Choy de Martinez, A. Rakotondrainibe, B. Beden, C. Lamy, *J. Electroanal. Chem.*, **302** (1991) 173

[24] H. Okamoto, N. Tanaka, *Electrochim. Acta*, **38** (1993) 503

[25] B.W. Mao, B. Ren, X.W. Cai, L.H. Xiong, *J. Electroanal. Chem.*, **394** (1995) 155

[26] M.T.M. Koper, M. Hachkar, B. Beden, *J. Chem. Soc. Faraday, Trans.*, **92** (1996) 3975

[27] H. Okamoto, N. Tanaka, M. Naito, *J. Phys. Chem. A*, **101** (1997) 8480

[28] H. Okamoto, N. Tanaka, M. Naito, *J. Phys. Chem. A*, **102** (1998) 7343

[29] H. Okamoto, N. Tanaka, M. Naito, *J. Phys. Chem. A*, **102** (1998) 7353

[30] H. Okamoto, N. Tanaka, M. Naito, *J. Electrochem. Soc.*, **147** (2000) 2629

[31] M. Krausa, W. Vielstich, *J. Electroanal. Chem.*, **399** (1995) 7

[32] J. Lee, C. Eickes, M. Eiswirth, G. Ertl, *Electrochim. Acta*, **47** (2002) 2297

[33] J. Wojtowicz, N. Maricic, B.E. Conway, *J. Chem. Phys.*, **48** (1968) 4333

[34] F. Raspel, R.J. Nichols, D.M. Kolb, *J. Electroanal. Chem.*, **286** (1990) 279

[35] A. Tripkovic, K. Popovic, R.R. Adzic, *J. Chem. Phys.*, **88** (1991) 1635

[36] N.M. Markovic, P.N. Ross, *J. Phys. Chem.*, **97** (1993) 9771

[37] F. Raspel, M. Eiswirth, *J. Phys. Chem.*, **98** (1994) 7613

[38] V. Kertész, G. Inzelt, C. Barbero, R. Kötz, O. Haas, *J. Electroanal. Chem.*, **392** (1995) 91

[39] H. Okamoto, N. Tanaka, M. Naito, *Chem. Phys. Lett.*, **248** (1996) 289

[40] P. Strasser, M. Lübke, F. Raspel, M. Eiswirth, G. Ertl, *J. Chem. Phys.*, **107** (1997) 979

[41] P. Strasser, M. Eiswirth, G. Ertl, *J. Chem. Phys.*, **107** (1997) 991

[42] M. Naito, H. Okamoto, N. Tanaka, *Phys. Chem. Chem. Phys.*, **2** (2000) 1193

[43] T.J. Schmidt, B.N. Grgur, N.M. Markovic, P.N. Ross, Jr., *J. Electroanal. Chem.*, **500** (2001) 36

[44] J. Lee, J. Christoph, P. Strasser, M. Eiswirth, *Phys. Chem. Chem. Phys.*, **5** (2003) 935

[45] Y. Honda, M.B. Song, M. Ito, *Chem. Phys. Lett.*, **273** (1997) 141

[46] SL. Chen, T. Noles, M. Schell, *Electrochem. Commun.*, **2** (2000) 171

[47] SL. Chen, D. Lee, M. Schell, *Electrochem. Commun.*, **3** (2001) 81

[48] SL. Chen, M. Schell, *J. Electroanal. Chem.*, **504** (2001) 78

[49] SL. Chen, D. Lee, M. Schell, *Electrochim. Acta*, **46** (2001) 3481

[50] B.E.K. Swamy, J. Maye, C. Vannoy, M. Schell, *J. Phys. Chem. B*, **108** (2004) 16488

[51] B.E.K. Swamy, C. Vannoy, J. Maye, M. Schell, *Electrochem. Commun.*, **6** (2004) 1032

[52] J. Wojtowicz, in: *Modern Aspects of Electrochemistry*, J.O'M. Bockris, B.E. Conway (Eds.), Plenum, Vol. 8, New York, 1973, pp. 47-120

[53] M.T.M. Koper, *Adv. Chem. Phys.*, **92** (1996) 161

[54] M.T.M. Koper, *J. Electroanal. Chem.*, **409** (1996) 175

[55] M.T.M. Koper, *Electrochim. Acta*, **37** (1992) 1771

[56] M.T.M. Koper, J.H. Sluyters, *J. Electroanal. Chem.*, **371** (1994) 149

[57] A. Naito, N. Tanaka, H. Okamoto, *J. Chem. Phys.*, **111** (1999) 9908

[58] M.T.M. Koper, *J. Chem. Soc., Faraday Trans.*, **94** (1998) 1369

[59] H. Matsui, M. Yasuzawa, A. Kunugi, *Electrochim. Acta*, **38** (1993) 1899

[60] H. Nyquist, *Bell. Syst. Tech. J.* **11** (1933) 126

[61] D.A. Harrington, J. Electroanal. Chem. 355 (1993) 21.

[62] M.E. Van der Geest, N.J. Dangerfield, D.A. Harrington, *J. Electroanal. Chem.*, 420 (1997) 89

[63] F. Seland, R. Tunold, D.A. Harrington, *Electrochim. Acta*, accepted for publication (2005)

[64] P.R. Bevington, *Data Reduction and Error Analysis for the Physical Sciences*, McGraw Hill, New York, 1969, pp. 200

[65] H. Okamoto, W. Kon, Y. Mukouyama, *J. Phys. Chem. B*, **108** (2004) 4432

[66] P. Strasser, M. Eiswirth, M.T.M. Koper, *J. Electroanal. Chem.*, **478** (1999) 50

[67] B. Beden, C. Lamy, N.R.D. Tacconi, A.J. Arvia, *Electrochim. Acta*, **35** (1990) 691

[68] O. Wolter, J. Willsau, J. Heitbaum, *J. Electrochem. Soc.*, **132** (1985) 1635

[69] K. Kunimatsu, H. Kita, *J. Electroanal. Chem.*, **218** (1987) 155

[70] S.G. Sun, J. Clavilier, A. Bewick, *J Electroanal. Chem.*, **240** (1988) 147

[71] T. Iwasita, S.H. Xia, *J. Electroanal. Chem.*, **411** (1996) 95

[72] A. Wieckowski, J. Sobkowski, *J. Electroanal. Chem.*, **63** (1975) 365

[73] G-Q, Lu, A. Crown, A. Wieckowski, *J. Phys. Chem. B*, **103** (1999) 9700

[74] J.D. Campbell, D.A. Harrington, P. van den Driessche, J. Watmough, *J. Math. Chem.*, **32** (2002) 281

[75] D.A. Harrington, P. van den Driessche, *J. Electroanal. Chem.*, **501** (2001) 222

[76] P. Strasser, *Electrochem. Soc. Interface*, Winter (2000) 46

[77] M. Schell, F.N. Albahadily, J. Safar, *J. Electroanal. Chem.*, **353** (1993) 303

Chapter 5

Improving the Performance of High-Temperature PEM Fuel Cells based on PBI Electrolyte

Frode Seland[*], Torsten Berning [a], Børre Børresen and Reidar Tunold

Electrochemistry Group, Department of Materials Science and Engineering, Norwegian University of Science and Technology, NO-7491, Trondheim, Norway

[a] *Present address: Adam Opel AG, International Technical Development Center, D-65423 Rüsselsheim, Germany*

Abstract

This paper describes the testing of the gas-diffusion electrodes for polymer electrolyte membrane fuel cells utilizing phosphoric acid doped polybenzimidazole (PBI) electrolyte, which allows for an operating temperature as high as 200 ºC. Membrane-electrode assemblies (MEAs) with an active area of 4 cm^2 were prepared and tested in a commercial fuel cell test-rig with 5 cm^2 flow field pattern. In order to determine the optimum structure of our anodes and cathodes, the platinum content in the Pt/C catalyst and catalyst loading were varied, as well as the loading of the PBI electrolyte dispersed in the catalyst layer. The different MEAs were tested in terms of their performance by recording polarization curves using pure oxygen and hydrogen. It was found that a high platinum content and a thin catalyst layer on both anode and cathode, gave the overall best performance. This was attributed to the different catalyst surface areas, the location of the catalyst in relation to the electrolyte membrane and particularly the amount of PBI dispersed in the catalyst layer. Scanning electron microscopy (SEM) was used in order to examine the cross-

[*] Corresponding author. Tel.: +4773594040, Fax: +4773594083. *E-mail address*: frodesel@material.ntnu.no (Frode Seland)

section of the MEAs and measure the thickness of the catalyst layers. With this information, it was possible to give an estimate of the porosity of the catalyst layer.

Keywords: PEM, Fuel Cell, Polybenzimidazole, High temperature, CO poisoning, Electrocatalysis

5.1 Introduction

To date, most PEM fuel cells are based on an electrolyte that relies on addition of liquid water to facilitate protonic conduction. Operating these fuel cells at a temperature close to the boiling point of water introduces a dual phase water system that must be controlled carefully. Common problems are the possible drying out of the electrolyte membrane at the anode at high current densities and possible flooding of the gas diffusion electrodes due to water condensation. A lot of work has been focussed on resolving the water-management issues related to these fuel cells, e.g. [1-4].

As PEM fuel cells approach commercialization there is an increased desire to raise the operating temperature to above 100 ºC. In automotive applications a higher operating temperature is desired because it increases the temperature gradient to the environment and hence reduces the radiator size. An operating temperature above 100 ºC simplifies the current water management problem. Hydrogen is the perfect fuel for fuel cells, but it has to be made from a hydrogen containing source, i.e. reforming natural gas or by splitting of water in water electrolysis. The carbon monoxide introduced to the fuel cells by operating them on for example reformed hydrogen or a carbon containing fuel like methanol, is particularly harmful towards platinum catalysts. High-temperature polymer fuel cells based on polybenzimidazole (PBI) electrolyte with an operating temperature up to 200 ºC, exhibit a high tolerance to carbon monoxide, as has previously been shown by Li et al. [5] and Holladay et al. [6]. Li el al. report a CO tolerance of 3% CO in hydrogen at current densities up to 0.8 A cm^{-2} at 200 ºC and 0.1% CO in hydrogen at 125 ºC and current densities lower than 0.3 A cm^{-2}, where CO tolerance is defined by a voltage loss less than 10 mV. The electro-osmotic drag coefficient for water and methanol in phosphoric acid doped PBI membranes has been reported by Weng et al. [7] to be essentially zero under all conditions. This greatly simplifies the material balances and mass transport management and reduces the cross-over of methanol in direct methanol fuel cells. High-temperature PBI fuel cells offer a

viable alternative to low-temperature PEM fuel cells that demand an extensive and expensive pre-treatment of the fuel.

Polybenzimidazole, PBI, is an amorphous basic polymer with a high thermal stability and a reported glass transition temperature of 420 ºC [8]. The conductivity of different PBI membranes in the pure state is very low and about 10^{-12} S cm^{-1} [9,10]. However, there are many ways of substantially increase the conductivity of PBI membranes, and this has been the focus in several recent published works, e.g. [11-16]. Polybenzimidazole reacts easily with acids, and phosphoric acid is the most frequently used dopant. Phosphoric acid undergoes hydrogen bond interaction or proton transfer reactions with basic polymers, and shows remarkable high proton conductivity even in anhydrous form, due to its unique proton conduction mechanism [17-19]. The idea to use PBI membranes doped with phosphoric acid as an electrolyte in fuel cells was first introduced by Wainright et al. [20]. A lot of work has been done by the Case Western Reserve University (CWRU) group and it was recently reviewed [21]. The proton conductivity of phosphoric acid doped PBI is influenced by relative humidity, temperature and acid doping level as reported by Ma et al. [15]. Conductivity increases with increasing temperature following an Arrhenius equation. At high doping levels of phosphoric acid (i.e., 630%) they reported that conductivity increases significantly with relative humidity mainly due to the interaction of water with excess acid. Li et al. [22] reported the presence of strong hydrogen bonds between phosphoric acid and nitrogen atoms of the imidazole rings by infrared and Raman spectroscopy. They found that only two molecules of phosphoric acid are bonded to each repeat unit of PBI. An excessive doping of acid is "free acid" and contributes to the high conductivity. The upper limit of proton transfer is thus given by the conductivity of the H_3PO_4 in liquid state. In a work done by He et al. [14] the conductivity of PBI was found to be as high as 6.8 x 10^{-2} S cm^{-1} at 200 ºC with a H_3PO_4 doping level of 560% and 5% relative humidity.

The development of a high proton-conducting PBI membrane, due to the extensive study by several groups, has notably decreased the voltage loss over the membrane and brought forward the necessity of switching the attention from the membrane to other aspects of the fuel cell. Further research and development of i.e. electrocatalysis and bipolar plates, are important in order to further improve the fuel cell performance. It was found by Barbir et al. [23] that the contact losses that occur at the interface between the bipolar plates and the backside of the gas diffusion electrodes can be as high as 0.150 Ω cm^2. This value corresponds to the resistance through an 80 μm membrane with a

conductivity of 5.33 x 10^{-2} S cm^{-1}, and demonstrates the need of improving the bipolar plates in both materials and channel geometries.

As a lot of effort has been put into the development of new membranes for high-temperature PEM fuel cells, little attention has been paid to the catalyst layer and specific catalyst area. As the catalyst layer has a three-dimensional nature, the voltage losses that occur here are not only reduced to the surface potential, but losses associated with the protonic migration towards the reaction sites exist as well. Subsequently, the thickness of the catalyst layer plays an important role. On the other hand, the overall catalyst loading has to be kept low in order to reduce the fuel cell cost, which shows the need to reduce the catalyst particle size in order to increase the specific surface area.

The focus in our work has been to understand the importance of a carbon support layer, improve single cell performance by varying the composition of the catalyst layer, and manufacturing of single membrane-electrode assemblies by hot-pressing. Instead of describing the multitude of different MEAs manufactured, this paper will focus on the outcome of our study, highlighting the main observations. This is best done by describing the function of each of the electrode layers. It has been found in several studies of PEM fuel cells that the type and composition of the catalyst is crucial for the cell performance. The electrodes were manufactured at our department with varying platinum content in the catalyst (platinum on carbon), varying catalyst loading as well as PBI loading. PBI membranes were provided by the Department of Chemistry, Technical University of Denmark (DTU), which is acknowledged.

5.2 Experimental

The electrodes described in this paper were prepared by manual spraying with an airbrush (Badger No. 100G). This method allowed for the accurate determination of the catalyst loadings as well as for a good reproducibility, and minimized loss of catalyst in the spraying procedure. Carbon fibre paper was purchased from Toray (TGP-H-120) while the carbon black (Vulcan XC-72) used in the carbon support layer was provided by Cabot Corporation. The electrocatalysts, HiSPEC^{TM} 3000 (20% Pt on Vulcan XC-72R), HiSPEC^{TM} 4000 (40% Pt on Vulcan XC-72R) and HiSPEC^{TM} 8000 (50% Pt on Vulcan XC-72R), were purchased from Johnson & Matthey, and the PBI membranes were provided by the Department of Chemistry, DTU, as a partner in the European 5th Framework Programme, contract no. ENK5-CT-2000-00323.

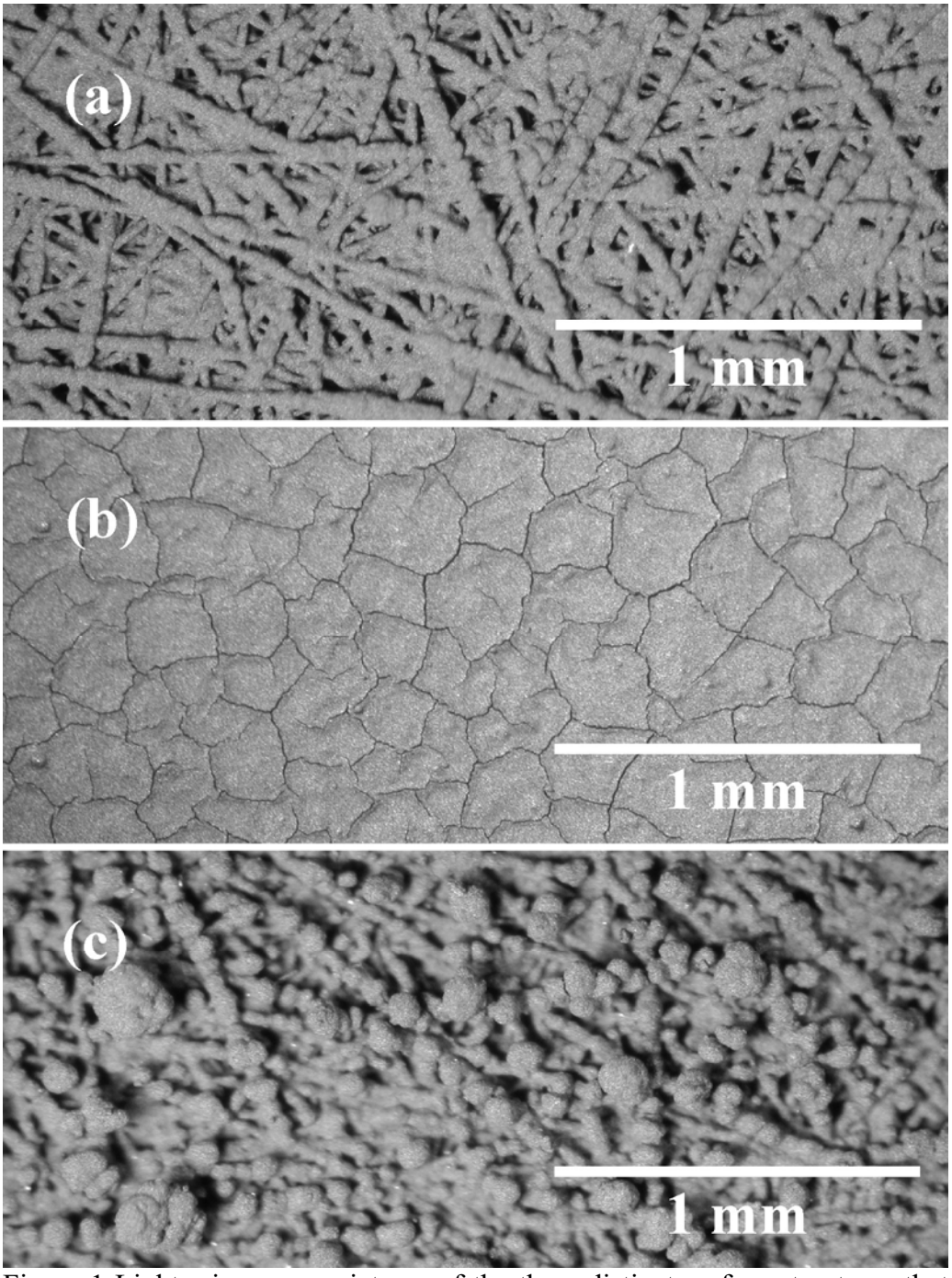

Figure 1 Light microscope pictures of the three distinct surface structures that the support layer obtained in this work, a) fibre structure, b) mud crack structure and c) dendrite structure.

5.2.1 MEA preparation

Due to the poor mechanical strength of the catalyst layers, they are deposited on a rigid backing or substrate. In this work, carbon fibre paper (Toray; TGP-H-120) was wet-proofed by immersing it in a 20% polytetrafluorethylene, PTFE-solution (DU PONT) and hot-baked at 360 ºC for 30 minutes in order to polymerize the PTFE. The weight increase for the wet-proofed paper compared with the non-wet-proofed paper was in the order of 20%. The PTFE was found to accumulate predominantly at the fibre crossings, thus reducing the porosity of the carbon fibre paper. This minor decrease in porosity was verified by testing the flow rate of a specific volume of air through the electrode before and after wet-proofing. The benefit of wet-proofing in this case lies in the prevention of the paper from soaking during the spraying procedure and reduces the penetration of carbon particles into the paper. This actually leads to a higher total porosity for the complete electrode by wet-proofing the carbon paper, most likely due to a lower pore size. Wet-proofing normally helps in terms of water management. It is unlikely, however, that one encounters any liquid water at an operating temperature of 175 ºC. The effect of PTFE on the cell performance in itself was therefore found to be insignificant. When spraying the carbon support layer onto the carbon fibre paper, it was found that the bonding between the carbon support layer and the fibre paper was improved by wet-proofing.

Carbon support layer

Although the carbon fibre paper provides a fairly smooth substrate on which the catalyst layer may be directly deposited, the need of a carbon support layer was found to be of much higher importance than first believed. Reproducible results were first obtained after extensively testing of the different preparation steps. The carbon support layer has several functions: i) to prevent the catalyst from penetrating into the carbon fibre paper, ii) to ensure a good electronic bonding between the carbon fibres and the catalyst layer, iii) to provide a pathway for the supply of reactants and the removal of product water and iv) to obtain a smooth and uniform surface on which the catalyst is deposited.

It is well known that when changing solvents, the properties of the particles dispersed in the solvent and therefore also the surface can be changed considerably. Depending on the spraying conditions (solvent, air flow, nozzle size and temperature) three distinct structures of the carbon support layer can be made, as shown in Figure 1, which shows examples of the different structures, taken with a light microscope. Figure 1a shows the first structure which

possesses a similar texture as the underlying carbon fibre structure, with the carbon powder evenly distributed on top of each fibre. It was a result of spraying with a solvent that rapidly evaporates. Secondly, Figure 1b, demonstrates a mud cracked structure with large islands and thin crevices that provided a smooth and flat surface. This structure was a result of using water as the solvent. A wet film was then formed when spraying the dispersion, and the mud cracked structure was obtained when drying the electrode after spraying. The third structure, Figure 1c, is a carbon dendrite structure with many carbon spikes, and was typically achieved when the nozzle was clogging or a too high air flow was applied during spraying.

To obtain good adhesion of the carbon particles to the fibres in the underlying carbon paper, structure 1 (Figure 1a) was found beneficial and offered a good electronic contact as well. Therefore, after making structure 1 on top of the carbon backing we made the mud crack structure (Figure 1b) on top of this. A total amount of 2 mg cm^{-2} carbon black was found to be sufficient to produce the desired support layer.

Catalyst layer

The catalyst layer is a key element in a fuel cell. It is important that the platinum catalyst is in close contact with the polymer membrane (electrolyte), the reaction gases and the current collector, and at the same time facilitate the transport of depleted reactants and product water out of the catalyst structure without impeding the supply of fresh reactants.

In order to obtain a catalyst layer with PBI dispersed in the layer, PBI was dissolved in concentrated dimethylacetamide (DMAc), and catalyst particles were dispersed in this solution. This dispersion was then sprayed slowly onto the support layer described above. In this work the catalyst type and loading as well as the PBI loading inside the catalyst layer was varied. Table 1 lists the anodes that were used in this study and Table 2 lists the cathode used. Cathode C1 was used as the reference cathode when studying the anodes, while anode A2 was used as the reference anode to the different cathodes.

At the cathode side mass transport limitations probably become more significant than at the anode side. As a result, the local current generation inside the cathodic catalyst layer would shift away from the electrolyte membrane, which leads to a higher IR loss in this layer. Clearly, there must be an optimum catalyst distribution both on the anode and cathode side, as well as an optimum

with respect to the amount of PBI in the mixture. Careful studies have been undertaken in order to find the optimum amount.

From earlier experiments performed at our department, a loading of equal amounts (weight) of platinum and PBI was considered standard. Note, however, that the PBI loading should, in theory, be scaled to the expected surface area of the catalyst, not to the overall amount. A scaling with the specific volume of the catalyst powder should yield similar results.

The reason why the anode side may be critical for this type of fuel cells is that the thickness of the catalyst layer may play an important role. On the other hand, the mass transport limitations for hydrogen are much lower than for oxygen due to the higher diffusivity of hydrogen. This implies that the local current density on the anode remains close to the electrolyte membrane, as long as sufficient catalyst area is provided. As a result, the 50% Pt/C, which provides the highest surface area per unit volume, should intuitively be the catalyst of choice at the anode side.

It should be mentioned that even with the spraying technique it is not possible to obtain exactly the desired loadings, but an effort was made to keep the final amount of platinum within 5% of the desired quantity.

Table 1 Anodes created for this study

Electrode name	Pt loading (mg cm^{-2})	Catalyst type (% Pt/C)	PBI loading (mg cm^{-2})
Anode 1, A1	0.30	20	0.30
Anode 2, A2	0.40	20	0.40
Anode 3, A3	0.40	20	0.60
Anode 4, A4	0.40	50	0.24
Anode 5, A5	0.40	50	0.36
Anode 6, A6	0.40	50	0.48

Table 2 Cathodes created for this study

Electrode name	Pt loading (mg cm^{-2})	Catalyst type (% Pt/C)	PBI loading (mg cm^{-2})
Cathode 1, C1	0.50	20	0.50
Cathode 2, C2	0.60	20	0.60
Cathode 3, C3	0.60	40	0.36
Cathode 4, C4	0.60	50	0.36
Cathode 5, C5	0.60	50	0.60

Acid doping, hot-pressing and testing of MEAs

After spraying the catalyst layer consisting of catalyst and PBI in dimethylacetamide (DMAc), the electrodes were heated for three hrs at 180 ºC in order to evaporate the remaining solvent. Li et al. report that a drying temperature of up to 190 ºC for hours is necessary to remove traces of DMAc [24]. The final step of preparing the electrodes is to dope the PBI in the catalyst layer with phosphoric acid by spraying. In this work we used a constant weight ratio of 6:1 between the phosphoric acid and the PBI. It is believed that the percentage of the acid will be evened out by diffusion with time, and besides, the membrane contains much more acid so that the acid loading is assumed to be less critical.

The membrane electrode assemblies (MEAs) were made by hot-pressing a sandwich of 2 x 2 cm^2 electrodes and a 4 x 4 cm^2 PBI membrane (which were previously doped in 75 wt% phosphoric acid) at 130 °C for 25 minutes with a pressure of 25 kg cm^{-2}. The MEAs were tested in a commercially available single cell fuel cell with one reference electrode probe and 5 cm^2 double serpentine flow field (ElectroChem, Inc), originally designed for low temperature PEM fuel cells. In order to ensure that the PBI in the catalyst layer and the membrane was completely saturated with phosphoric acid, the MEAs were cured for two weeks after the hot-pressing and then tested.

The polarization curves of all our membrane electrode assemblies were recorded at different temperatures, but with focus on 175 ºC as a default temperature. The fuel cells were tested with pure hydrogen and oxygen (instrumental grade 2.0) at a high stoichiometric flow rate in order to reduce the

mass transport limitations by diffusion through the porous medium. Note that at the cathode side, a further limitation arises because of the complete evaporation of two water molecules for each consumed oxygen molecule, which creates a pressure gradient and hence a convective flux, which is directed from the catalyst to the channel.

5.2.2 Theoretical considerations

In this study, the effect of different platinum catalyst types (platinum on carbon, Pt/C) and composition on the fuel cell performance was investigated. The Pt/C catalysts were provided by Johnson & Matthey, and relevant information is listed in Table 3. In heterogeneous catalysis the available active surface area is of major importance, and hence the 20% Pt/C powder seems to offer the best value as the total metal area per gram is by far the largest. This is also demonstrated by the higher roughness factor that this catalyst may obtain.

Table 3 Summary of catalyst and catalyst layer

Catalyst type (nominal)	20% Pt/C	40% Pt/C	50% Pt/C
Catalyst measured[a] [wt% Pt]	0.1996	0.3967	0.4865
Average Pt particle size[a] [nm]	2.6	3.54	3.51
Min. metal surface area[a] [$m^2_{Pt}\ g_{Pt}^{-1}$]	90	60	50
Theoretical roughness[b] [$m^2_{Pt}\ m^{-2}_{geo}$]	540	360	300
Theoretical specific Pt area[c] [$m^2\ cm^{-3}$]	13	25	29
Real catalyst layer thickness[d] [μm]	47	14	6
Estimated porosity[c] [%]	74	65	31

[1] Data as provided by Johnson Matthey Corp.

[b] Assumes that the entire Pt surface area is active and a loading of 0.6 mg cm^{-2}

[c] Based on a loading of 0.6 mg Pt cm^{-2} and assuming a density of 2270 kg m^{-3} of the carbon [26], 21440 kg m^{-3} for the platinum [27] and 5000 kg m^{-3} for the phosphoric acid doped PBI, as measured in our lab

[d] Real catalyst layer thickness as determined from SEM scans

From theoretical considerations there is a disadvantage by using the smallest platinum particles provided by the 20% Pt/C. The overall thickness of the catalyst layer, when using 20% Pt/C, is at least twice the thickness, when either

40% or 50% Pt/C are being used. This leads to a longer diffusion path from the active catalyst site to the proton conducting membrane. Scanning electron microscope (SEM) scans of the cross-section of the respective MEA provides rough estimates of the real catalyst thickness. A loading of 0.6 mg Pt cm^{-2} (cathode side) gave an approximate thickness of 47 μm for 20% Pt/C, 14 μm for 40% Pt/C and 6 μm for 50% Pt/C. This shows an even stronger dependency on platinum content than indicated by theoretical considerations. This huge difference between the expected and actually measured thickness may be due to the different properties the catalyst particles obtain in the DMAc solution due to different catalyst compositions and particle size. This was not further investigated in this work. It was shown by for example Bevers et al. [25] in their work with Nafion® fuel cells, that most of the catalytic activity takes place in areas close to the electrolyte membrane, typically within the first 10 μm. This might be different for PBI fuel cells, because in terms of the permeability to the reactants the PBI exhibits different values, which should affect the current distribution inside the catalyst layer. Due to elevated temperatures, reaction kinetics is also of importance.

A theoretical thickness in the region of 40 μm can roughly be estimated for a cathode with 20% Pt/C catalyst and with porosity of 70%. This value is in the range of the membrane thickness, and this means that the IR losses due to protonic migration inside the catalyst region may be similar or even higher than in the membrane at elevated current densities.

At low current densities, only a small fraction of the available catalyst area is needed, and the current will be generated at the energetically favoured sites. These sites are likely to exist near the electrolyte membrane since it is easier for the reactant gases to diffuse through than for the protons to migrate through the catalyst layer. However, with increased current density, the reactant gases become more and more depleted, and the local current generation shifts away from the membrane interface. This may also be caused by the fact that the energetically favoured sites are occupied. This means that the protons have to migrate further. Because of the fact that the catalyst layer consists only of a small fraction of PBI electrolyte, the losses associated with the protonic migration can be of the same magnitude or even higher than the ohmic losses in the membrane. Thus, it is important to provide a high catalyst area in a region close to the membrane interface without starving the cell of reactants, which occurs when too much electrolyte is needed. This is of particular importance at the cathode side of the PBI fuel cell, because the permeability for oxygen through phosphoric acid doped PBI at 150 ºC is much lower than through

Nafion®-117 at 80 ºC, 10^{-9} and $9 \cdot 10^{-9}$ cm^3 (STP) cm cm^{-2} s cmHg respectively [28,29].

The goal of this study is to agree on whether it is the surface area and porosity of the catalyst layer or the thickness of the catalyst layer and how close the catalyst and PBI particles are to the membrane, which determines the performance. Intuitively, the catalyst close to the electrolyte interface is more valuable than the catalyst far away from the membrane. In the latter case, the IR losses inside the catalyst become a major loss mechanism. Relevant information is listed in Table 3.

5.3 Results and Discussion

5.3.1 Open circuit voltage

The open circuit voltage (OCV) is the maximum voltage that can be achieved in a fuel cell with zero loading, and sometimes referred to as the rest voltage. Normally, the value of the OCV lies close to the thermodynamic equilibrium potential i.e. as is observed in a hydrogen / chlorine fuel cell [30]. In other cases it can be considered as a mixed potential. In this study, the open circuit voltage varied from one MEA to another, but usually in the range 840 to 900 mV depending on the operating temperature and MEA characteristics. The open circuit voltages are given in Table 4.

Table 4 Open circuit voltages for selected cells at 125 ºC and 175 ºC

MEA	A2C1	A2C2	A2C3	A2C4	A2C5	$A5C5_{ii}$
E_{OCV} [mV], 125 ºC	870	850	855	845	860	770
E_{OCV} [mV], 175 ºC	880	880	900	890	885	805

In a H_2/O_2 fuel cell, the measurement of the thermodynamic rest potential on the oxygen reduction is very difficult due to the very low exchange current density of the oxygen electrode on platinum (around 10^{-10} A cm^{-2}) [31]. As a consequence to this, the measurement of the open circuit potential is easily influenced by any other side reactions, i.e. corrosion of platinum. In fact, the rest potential measured rarely exceeds 1.1 V vs. the NHE even on a very active platinum electrode in purified acid or alkaline aqueous solution, with 1

atmosphere of oxygen and ambient temperature [32]. The most frequently reported open circuit potentials for oxygen electrodes in Nafion® based fuel cells are around 1.0 V vs. the NHE.

Extensive research has been done in order to minimize the polarization losses on the cathode by improving the kinetics of the oxygen reduction reaction. A part of the problem is that the complete reduction of oxygen to water involves four successive electron transfer steps that are particularly slow in phosphoric acid environment due to the presence of the bulky phosphate anions adsorbed on the catalyst surface.

The anode operates at a potential just above the reference hydrogen potential and under such highly reducing conditions that carbon has low probability to corrode. On the other hand, when the fuel cell is operated at low current densities, the potential at the cathode can be about 0.7 V above that of the anode and even higher at open circuit. Carbon will oxidize to carbon dioxide at this potential, but only at a very slow rate [33].

$$C + 2H_2O \rightarrow CO_2 + 4H^+ + 4e^- \quad (1)$$

Such anodic back reactions are another reason why fuel cells with carbon supported catalysts do not give the thermodynamic equilibrium voltage for the hydrogen / oxygen reaction at open circuit.

In this work an increase, usually around 30 mV, in the open circuit voltage was observed, as the temperature was increased from 125 ºC to 175 ºC. This is believed to be due to better kinetics as the temperature increases and that the exhaust water in gaseous state will leave with less hindrance at a higher temperature.

Other parameters that can easily influence the value of the open circuit voltage are the thickness of the polymer membrane, holes in the membrane (puncturing), flow rate of the fuel cell feeds, humidity and contamination. It is well known that fuel cross-over, i.e. hydrogen crossover in a H_2/O_2 fuel cell, will decrease the open circuit voltage of that fuel cell, due to an establishment of a mixed potential on the cathode. Using a thin membrane the resistance to cross-over of reaction gases through the membrane is lower and a more pronounced effect of a mixed potential is expected. Thus the electrode potential and the corresponding open circuit voltage of the fuel cell will decrease. This was observed by the low open circuit voltage obtained by using a thin membrane (25 μm) in the MEA denoted $A5C5_{ii}$ compared to the open circuit values for the other MEAs (thickness around 40 μm). One of the most critical

issues when operating a fuel cell is the chance of puncturing the membrane and thus creating an easy path for reaction gases to the opposite electrode. This is the most likely reason why an MEA stops functioning and thus leads to an extremely low open circuit voltage. Puncturing or cracking of the membranes is particularly critical when operating a fuel cell stack.

5.3.2 Anode side

Figure 2 shows the polarization curves at 175 ºC for MEAs where the loading of the platinum catalyst and the amount of PBI in the catalyst layer of the anode is varied. See Table 1 for relevant information. Note again that the electrode composition used at the cathode side was the same in all cases and equal to cathode C1 (Table 2). Inconsistencies in the spraying technique, hot-pressing, membrane thickness or cutting of 2x2 cm^2 electrodes could lead to small changes in performance. However, after continuously improving our testing procedure, we found the performance of the MEAs to be quite reproducible.

As seen from Figure 2; the effect of an increase in catalyst loading on the anode side was found to be relatively strong, as opposed to Nafion® fuel cells, where the effect of the anode side is usually neglected. This is apparently not the case with PBI fuel cells, where the hydrogen oxidation may be more lethargic in the phosphoric acid environment. Figure 2 shows the polarization curves of A1C1, A2C1 and A3C1, and an improvement of current density was found to be around 15-20% at a cell voltage of 500 mV when increasing the platinum loading from 0.3 mg cm^{-2} and up to 0.4 mg cm^{-2}. A further increase in the current density of somewhat less than 10% was previously found when the loading was increased to 0.6 mg cm^{-2} on the anode side. The effect of catalyst loading was found to be even more pronounced at 125 ºC.

Based on this finding we conclude that the hydrogen kinetics and hydrogen solubility and permeability are slow in phosphoric acid doped PBI environment compared to Nafion®, and thus an increased three-phase region (reactant, membrane and catalyst) is desired. PBI exists in the catalyst layer as scattered particles. An increased reaction zone can be achieved by increasing the platinum and PBI loading up to a certain extent, increasing the platinum content or increasing the catalyst layer thickness. However, an increased platinum content would decrease the catalyst layer thickness when equal amount of platinum is to be used, so there will be a compromise between the two.

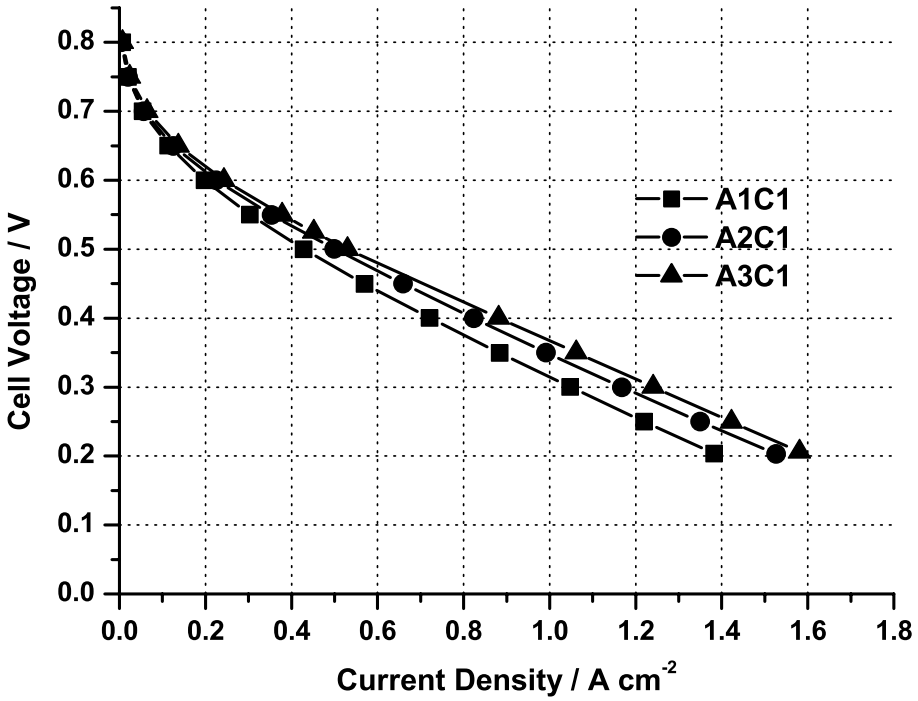

Figure 2 Polarization curves for A1C1 (squares), A2C1 (circles) and A3C1 (triangles) at 175 °C.

By comparing the performance of the cells A2C1 and A3C1 in Figure 2, and A4C1, A5C1 and A6C1 in Figure 3, an effect of increasing the PBI loading in the catalyst layer can be observed. When the PBI loading was increased by 50%, with the same type and same amount of catalyst, there was a noticeable increase in fuel cell performance implying that an increase of the amount of PBI had a beneficial effect on the performance. An increase in the PBI loading obviously enhances the protonic transport inside the catalyst layer and makes the catalyst to be used more effectively. Interestingly, the performance of A6C1 in Figure 3 clearly demonstrates the effect of having too much PBI in the catalyst layer. The performance drops drastically and was related to the isolating and blocking of active catalyst particles by the excessive amount of PBI, thus reducing the overall oxidation rate of hydrogen. Note again that the cathode side is the same in all cases, cathode C1.

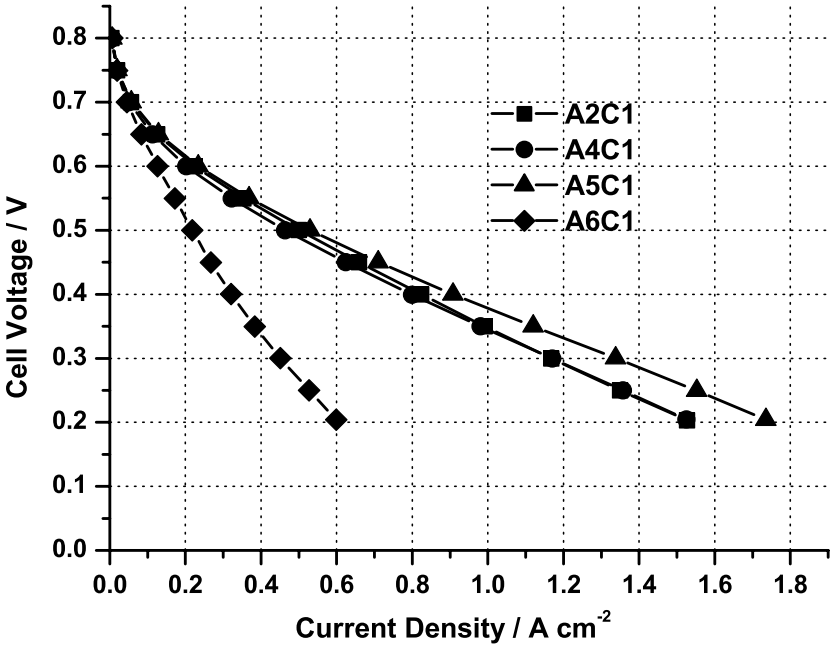

Figure 3 Polarization curves for A2C1 (squares), A4C1 (circles), A5C1 (triangles) and A6C1 (diamonds) at 175 °C

The effect of using a higher platinum concentration on the anode side near the membrane interface could be interpreted by comparing the performance of A2C1 versus A4C1 in Figure 3. Anode A2 and anode A4 are theoretically comparable in the platinum loading and the PBI loading, which was scaled with respect to the catalyst volume. The performance of these cells was found to be similar, although the surface area of the catalyst must be higher for anode A2. Note again that an effort was made to scale the PBI loading with the volume of Pt/C catalyst powder, which means that a PBI loading of 0.24 g cm^{-2} with the 50% Pt/C catalyst about corresponds to a loading of 0.4 mg cm^{-2} using the 20% Pt/C.

Considering the fact that anode A5 was slightly better than anode A3, and taking into account that the price of the 50% Pt/C catalyst is lower based on the amount of platinum, we conclude that using a high platinum content and relative high PBI loading in the catalyst layer yields the best performance and hence decreases the cost in making our MEAs.

5.3.3 Cathode side

Similar to the anode side, the various cathodes made for this study were tested, using the anode A2 given in row 2 in Table 2 for counter electrode. The cathodes prepared varied in the Pt/C catalyst composition and loading, as well as the PBI loading. Polarization curves of the corresponding fuel cells were recorded at different temperatures with 175 ºC as the reference temperature. The performances of the different MEAs tested at 175 ºC are given in Figure 4.

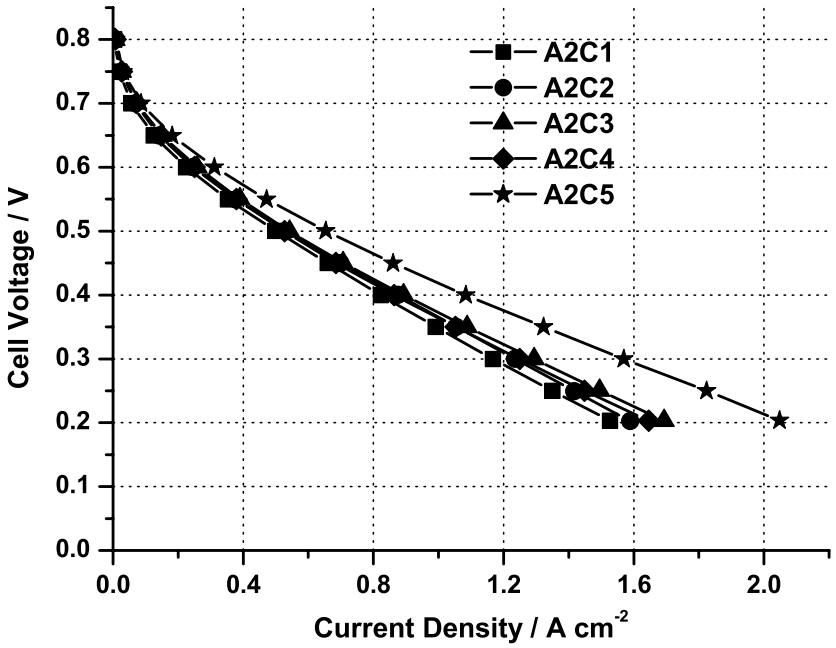

Figure 4 Polarization curves of five MEAs with varying cathodes at 175 ºC, A2C1 (squares), A2C2 (circles), A2C3 (triangles), A2C4 (diamonds) and A2C5 (stars).

The effect of simply increasing the amount of catalyst was observed by noticing the change in performance between A2C1 and A2C2 in Figure 4, where the catalyst loading on the cathode side was changed from 0.5 mg cm^{-2} to 0.6 mg cm^{-2}, respectively. Considering that the increase in catalyst loading is 20%, the effect on the performance is low, resulting in an increased performance of around 5%. In fact, the difference in performance between the other cathodes tested was surprisingly low with the exception of cathode C5. While the nominal catalyst loading was the same in all cases, except cathode C1, it must be stressed again that the surface area for the different cathodes varies.

It was found that when increasing the temperature, the performances of cathodes C2, C3 and C4 became almost identical. However, cathode C5 clearly showed an advantage over the other cathodes at 175 ºC. The performance was superior in all potential regions. Of all the cathodes tested in Figure 4, cathode C5 had the highest PBI loading based on catalyst volume, and we can conclude that a high amount of PBI was advantageous on the cathode side.

The differences between the different cathodes, except cathode C5, were relatively small compared to the differences that occurred when using different anodes. This was an interesting and unexpected finding, which indicates that a lot of the losses in this type of fuel cells are related to the limited permeability of the reactant gases at the catalyst layers and solubility of reactants in the dispersed PBI particles.

5.3.4 Platinum and PBI loading inside the catalyst layer

The catalyst layer is important in many ways and critical when it comes to cell design. It has to be ensured that on one side the reactants (e.g. oxygen) have access to the platinum surface, but on the other hand the protons, which are being conducted through the electrolyte, must be able to reach the reaction site. As a consequence, it is desirable to have a thin film of electrolyte material covering the catalyst to facilitate the transport of protons. Because of the numerous transport phenomena that occur inside the catalyst layer, the exact amount of PBI has to be carefully determined for optimum cell performance.

An important finding here was that it takes a few days for the PBI to absorb the phosphoric acid and hence become a good protonic conductor. This means that during the first days the performance of the cell changes considerably, which complicated the testing procedures. As a remedy for this we decided to let all our MEAs cure for two weeks before testing them. This ensured that the membrane was satisfactorily doped with phosphoric acid and gave reproducible results.

In this study we have found that the amount of PBI is one of the most important parameter in order to improve the fuel cell performance. The function of the PBI inside the catalyst layer is obviously to provide a path for the protons to reach the platinum surface, where the reaction occurs. The oxygen and hydrogen have to dissolve into the PBI and diffuse towards the platinum. This means that the PBI has to be a protonic conductor, and at the same time have a high solubility and diffusivity for the reactants. A high amount of PBI will

improve the protonic transport on one hand, but also it will make it more difficult for the reactants to reach the platinum surface, hence it will cut off the current prematurely as clearly illustrated by the performance of anode A6 in Figure 3. A low amount of PBI means that the reactant gases can easier reach the platinum surface, but at the same time it increases the resistance towards the proton migration, leading to an increased IR loss. It is important that the solubility of oxygen and hydrogen in PBI is high, and work concerning ways of increasing solubility should be of high priority.

It appears logical that the amount of PBI mixed into the catalyst layer should be scaled with the expected surface area of the platinum rather than with the weighed amount of platinum. The amount of PBI was tested in a parametric study and the amount of PBI used in anode A5 and cathode C5, 0.36 mg cm^{-2} and 0.6 mg cm^{-2} respectively, was found to be the optimum among the electrodes tested in this study.

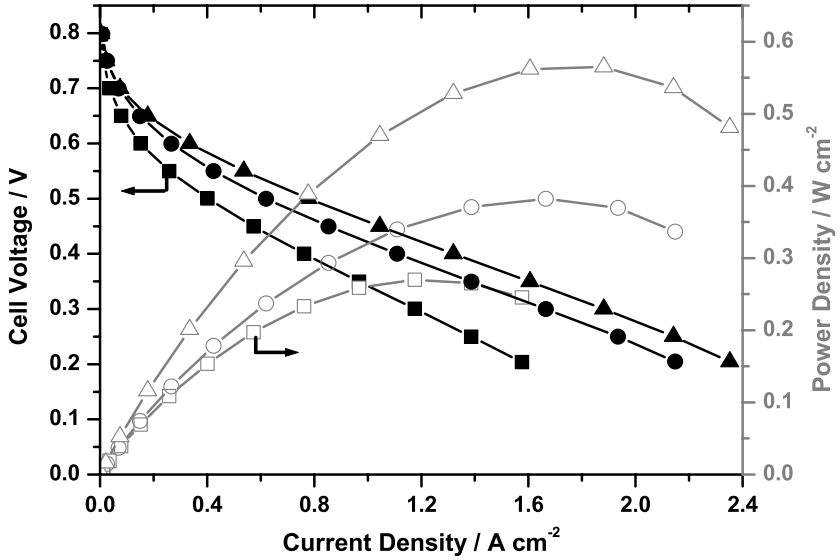

Figure 5 Polarisation curves (closed symbols) and power density curves (open symbols) at 125 °C (squares), 150 °C (circles) and 175 °C (triangles) for the MEA A5C5ii.

The polarization curves obtained with the various electrodes indicate that A5 and C5 are the best anode and cathode compositions, respectively. The overall platinum loading is 1.0 mg cm^{-2} and both electrodes employed the 50% Pt/C catalyst. The resulting cell performance and power density curves when the best anode and the best cathode were combined are given for 125 ºC 150 ºC and 175 ºC in Figure 5. The effect of increasing the temperature is clearly seen. This is mostly due to enhanced reaction kinetics and lower IR losses.

5.3.5 Scanning electron microscopy (SEM)

Several SEM scans were performed in this study. Both surface scans of the various electrodes and cross-sectional scans of the MEAs were conducted. A cross-section of the MEA was examined by SEM after testing it. In order to obtain high quality SEM scans of the cross-section near the membrane, the MEA was dipped in liquid nitrogen prior to breaking.

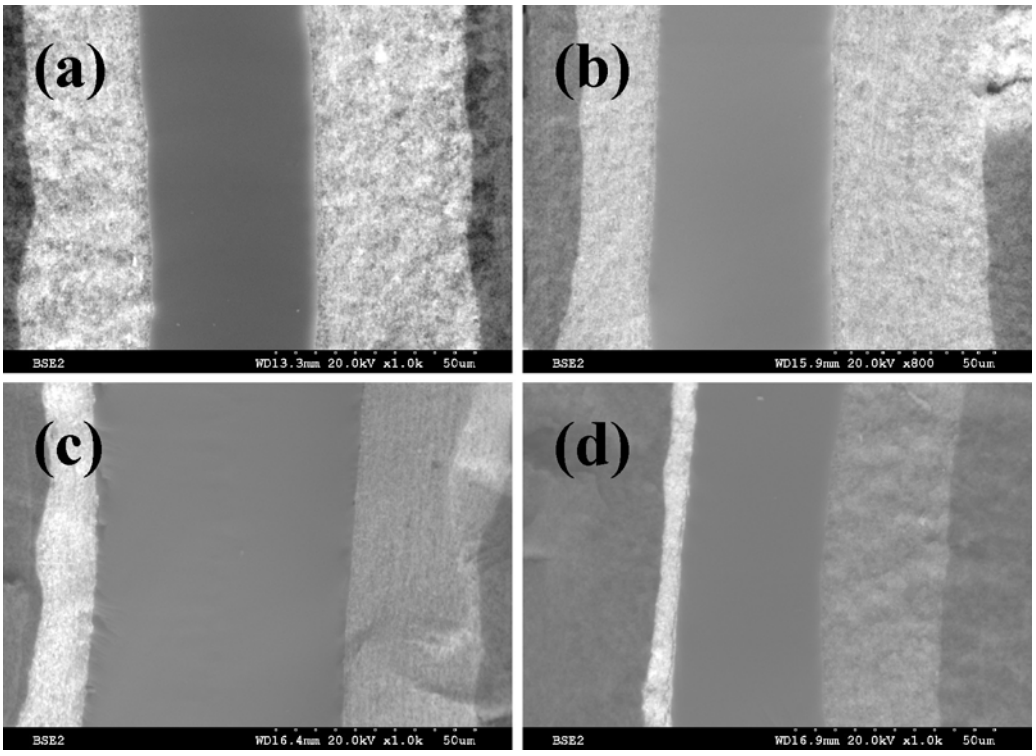

Figure 6 Scanning Electron Microscopy (SEM) scans in backscattered mode of the cross-sections of the MEAs a) A2C1, b) A2C2, c) A2C3 and d) A2C4. The cathode is situated to the right side of the PBI membrane in (a) and (b) while it is situated to the left side of the PBI membrane in image (c) and (d).

Figure 6 shows SEM pictures in backscattered mode of the MEAs A2C1, A2C2, A2C3 and A2C4, which were all used in this work. Backscatter mode was preferred as the catalyst layer can easily be seen since platinum shines up due to its high atomic weight. The catalyst layer can be seen as narrow bright bands on both sides of the membrane. The carbon support layer can also easily be identified as the dark region on the outside of the catalyst layer.

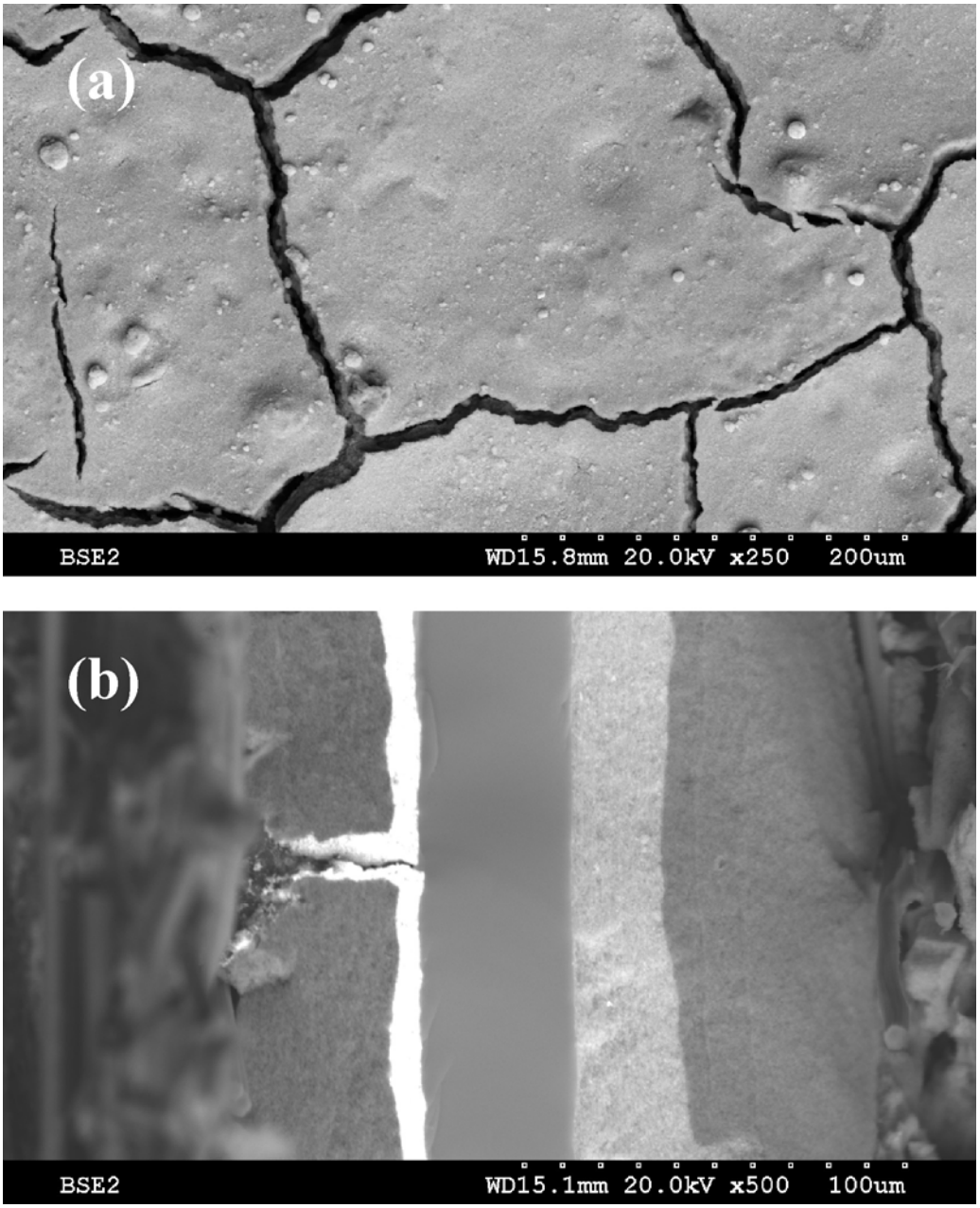

Figure 7 SEM scans in backscattered mode, a) Top-view of cathode C5 showing the mud crack surface structure, b) cross-section of the corresponding MEA, A2C5, with focus on the small crevice on the cathode (left) side.

It is easy to see how marked the difference in catalyst layer thickness appears to be between the different catalyst compositions. The 20% Pt/C catalyst clearly gives a huge thickness of about 50 µm on the cathode side (C2). As the cathode

catalyst composition varies from 20% Pt/C (C1, C2) to 40% Pt/C (C3) and up to 50% Pt/C (C4) the thickness is substantially decreased. SEM scans also show the quality and reproducibility of the spraying technique, which in our case is satisfactorily.

It is important to note that the mud cracked morphology that is obtained after spraying the support layer (Figure 1b) may not be the most optimal one. Due to this mud cracked structure a substantial amount of catalyst is being forced into the crevices when spraying the catalyst layer and this catalyst will not contribute to the cell performance. Figure 7a shows a top-view SEM scan of the complete electrode, cathode C5, used in this study. A SEM picture of the cross section of the corresponding MEA, A2C5, is given in Figure 7b. The last picture focuses on the small crevice on the cathode side, and we can clearly see that the catalyst has been sprayed down into this crevice. This is a major disadvantage of spraying catalyst onto a carbon fibre paper instead of directly onto the polymer membrane. Direct spraying onto the membrane is currently being investigated in our laboratories. When preparing electrodes separate from the membrane we conclude from this that the desired surface consists of very large islands with as small crevices as possible to limit the loss of active catalyst, but not constraining the diffusion of reactants to the reaction sites. Our electrodes have a measured crack width of about 5 - 10 μm (Figure 7).

The overall thickness of the catalyst layer (cathode) was measured from the SEM images. A 20% Pt/C catalyst gave a thickness of 47 μm compared to 14 μm for the 40% Pt/C and as low as 6 μm when 50% Pt/C was used. The corresponding porosity of the catalyst layer was estimated to be 74%, 65% and 31% respectively.

5.3.6 Effect of membrane thickness

The thickness of the PBI membrane is varying from one research group to the other, but generally it is quite low. Case Western Reserve University group and the group at the Danish Technical University (DTU) make membranes about 80 μm thick [20,24,34-36]. Savadogo and Xing used commercially bought (Hoechst Celanese) PBI films of 40 μm thickness [37] and obtained very nice performance of their fuel cells. Staiti et al. measured the thickness of their dried PBI membranes to be in the range of 47 ± 3 μm [38]. The PBI membranes used in this work were provided by DTU with a measured thickness after hot-pressing around 40 μm.

The best anodes and cathodes in this study were put together to make MEAs denoted $A5C5_n$, where n indicates a specific MEA. We wanted to test the influence of different membrane thickness at two distinct temperatures. $A5C5_i$ is around 40 µm thick while $A5C5_{ii}$ is the thinnest one with membrane thickness of only 25 µm.

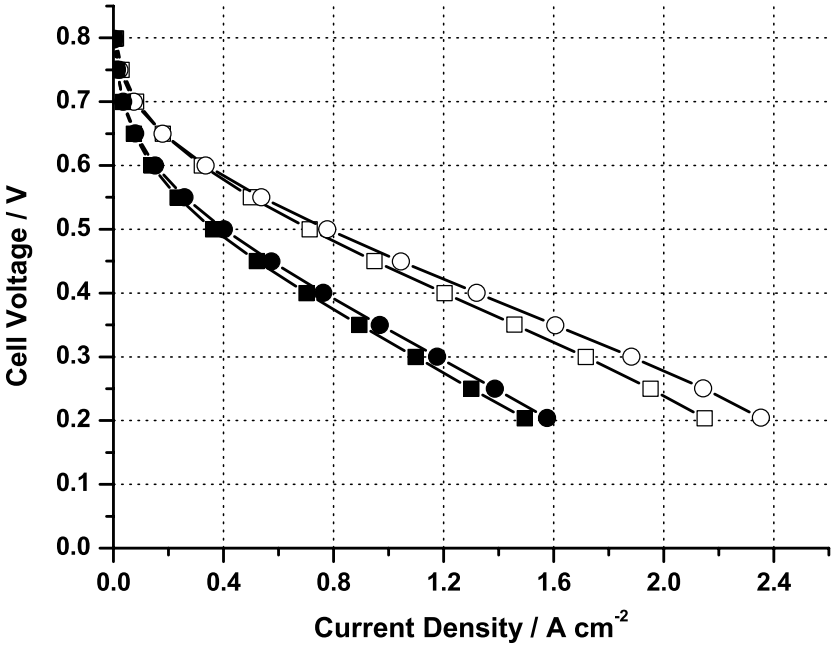

Figure 8 Performance of two MEAs with different membrane thickness, $A5C5_i$ (40 µm, squares) and $A5C5_{ii}$ (25 µm, circles) at 125 ºC (closed symbols) and 175 ºC (open symbols).

From Figure 8 we can see that the membrane thickness is affecting the performance of the fuel cell. A thin membrane clearly enhances the performance at lower potentials while a thick membrane would supposedly show better results at higher potentials where the current density is lower.

One of our largest concerns when testing our MEAs is the high possibility of puncturing the membrane while running. A thin membrane can easily break at the edges of the membrane electrode sandwich due to the stress that occurs when fitting it in our fuel cell hardware and when applying gases on both sides. Taking this into consideration, a slightly thicker membrane would make continuous testing possible and was therefore preferred ($A5C5_i$).

5.4 Conclusions and future work

This paper focuses on the understanding of the gas diffusion electrodes in PBI fuel cells and their effect on the performance. Various electrodes were prepared using the spraying technique. The best performance was obtained using a catalyst of 50% Pt/C and a relative high PBI loading in the catalyst layer on both anode and cathode, anode A5 (0.4 mg cm^{-2} Pt, 0.36 mg cm^{-2} PBI) and cathode C5 (0.6 mg cm^{-2} Pt, 0.6 mg cm^{-2} PBI) respectively. The structure of the support layer was found to be of more importance than first believed. A mixture of dry and wet spraying gave the best characteristics with a good bonding to the carbon fibre paper and a good support for the catalyst layer. In order to further reduce the catalyst loading, different techniques have been proposed, such as sputtering of fine catalyst particles on top of the electrode and spraying of catalyst directly onto the polymer membrane. This will be investigated further at our department.

In addition, it was mentioned that the current tests were all performed using bipolar plates designed for low-temperature Nafion® fuel cells. These fuel cells exhibit a comparatively high amount of mass transport problems, which are in part caused by the existence of liquid water inside the gas diffusion layers (e.g.), and partly due to the low diffusivity of the reactants, which are temperature dependent. These phenomena have caused fuel cell manufacturers to use bipolar plates with long, serpentine channels, where a high pressure drop forces the liquid water out of the channels, or else use interdigitated designs, where a pressure drop is induced between flow channels in order to eliminate mass transport losses. The disadvantage of serpentine channels is clearly the expected uneven current distribution, as the gases will be very rich at the inlet and depleted towards the outlet. In the case of PBI fuel cells operating above up to 200 ºC, the mass transport problems should be significantly reduced. This should allow for the use different bipolar plate designs with a larger shoulder width in order to reduce the contact resistance, and possibly with a higher number of parallel channels, which would result in a more even distribution of the local current densities, provided proper manifolding can be obtained.

5.5 Acknowledgments

The authors thank Dr. Gaute Svenningsen for invaluable help in preparing and performing the SEM scans. This work was funded by the European Commission in the 5th Framework Programme (Contract no. ENK5-CT-2000-00323).

References

[1] D.P. Wilkinson, H.H. Voss, K. Prater, *J. Power Sources*, **49** (1994) 117

[2] R. Mosdale, S. Srinivasan, *Electrochim. Acta*, **40** (1995) 413

[3] H.P.L.H. van Bussel, F.G.H. Koene, R.K.A.M. Mallant, *J. Power Sources*, **71** (1998) 218

[4] T. van Nguyen, M.W. Knobbe, *J. Power Sources*, 114 (2003) 70

[5] Q. Li, R. He, J.-A. Gao, J.O. Jensen, N.J. Bjerrum, *J. Electrochem. Soc.*, **150** (2003) A1599

[6] J.D. Holladay, J.S. Wainright, E.O. Jones, S.R. Gano, *J. Power Sources*, **130** (2004) 111

[7] D. Weng, J.S. Wainright, U. Landau, R.F. Savinell, *J. Electrochem. Soc.*, **143** (1996) 1260

[8] P. Musto, F.E. Karasz, W.J. MacKnight, *Polymer*, **34** (1993) 2934

[9] H.A. Pohl, R.P. Chartoff, *J. Polym. Sci., Part A*, **2** (1964) 2787

[10] S.M. Aharoni, A.J. Signorelli, *J. Appl. Polym. Sci.*, **23** (1979) 2653

[11] R. Bouchet, S. Miller, M. Duclot, J.L. Souquet, *Solid State Ionics*, **145** (2001) 69

[12] A. Schechter, R.F. Savinell, *Solid State Ionics*, **147** (2002) 181

[13] H. Pu, W.H. Meyer, G. Wegner, *J. Polym. Sci., Part B*, **40** (2002) 663

[14] R. He, Q. Li, G. Xiao, N.J. Bjerrum, *J. Membr. Sci.*, **226** (2003) 169

[15] Y.-L. Ma, J.S. Wainright, M.H. Litt, R.F. Savinell, *J. Electrochem. Soc.*, **151** (2004) A8

[16] J.A. Asensio, S. Borrós, P. Gómez-Romero, *J. Electrochem. Soc.*, **151** (2004) A304

[17] R.A. Munson, M.E. Lazarus, *J. Phys. Chem.*, **71** (1967) 3245

[18] T. Dippel, K.D. Kreuer, J.C. Lassègues, D. Rodriguez, *Solid State Ionics*, **61** (1993) 41

[19] M.F.H. Schuster, W.H. Meyer, M. Schuster, K.D. Kreuer, *Chem Mater.*, **16** (2004) 329

[20] J.S. Wainright, J.-T. Wang, D. Weng, R.F. Savinell, M. Litt, *J. Electrochem. Soc.*, **142** (1995) L121

[21] J.S. Wainright, M.H. Litt, R.F. Savinell, in: *Handbook of Fuel Cells - Fundamentals, Technology and Applications*, W. Vielstich, H.A. Gasteiger, A. Lamm (Eds.), Vol. 3: *Fuel Cell Technology and Applications*, John Wiley & Sons, Chichester, 2003, pp. 436-446

[22] Q. Li, R. He, R.W. Berg, H.A. Hjuler, N.J. Bjerrum, *Solid State Ionics*, **168** (2004) 177

[23] F. Barbir, J. Braun, J. Neutzler, *J. New Mat. Electrochem. Systems*, **2** (1999) 197

[24] Q. Li, H.A. Hjuler, N.J. Bjerrum, *J. Appl. Electrochem.*, **31** (2001) 773

[25] D. Bevers, M. Wöhr, K. Yasuda, K. Oguro, *J. Appl. Electrochem.*, **27** (1997) 1254

[26] *CRC Materials Science and Engineering Handbook*, J.F. Shackelford, W. Alexander (Eds.), third ed. [online], Boca Raton, CRC Press LLC, 2001, p. 56

[27] *CRC Materials Science and Engineering Handbook*, J.F. Shackelford, W. Alexander (Eds.), third ed. [online], Boca Raton, CRC Press LLC, 2001, p. 58

[28] J.S. Wainright, J.-T. Wang, R.F. Savinell, M. Litt, H. Moaddel, C. Rogers, in: Proceedings of Electrochemical Society; *Electrode materials and Processes for Energy Storage and Conversion*, S. Srinivasan, D.D. Macdonald, A.C. Khandkar (Eds.), Proceedings volume 94-23 (1994) pp. 255-264

[29] T. Sakai, H. Takenaka, N. Wakabayashi, Y. Kawami, E. Torikai, *J. Electrochem. Soc.*, **132** (1985) 1328

[30] M. Thomassen, B. Børresen, G. Hagen, R. Tunold, *Electrochim. Acta*, **50** (2004) 1157

[31] A. Damjanovic, J.O'M. Bockris, *Electrochim. Acta*, **11** (1966) 376

[32] M.R. Tarasevich, A. Sadkowksi, E. Yeager, in: *Comprehensive Treatise of Electrochemistry*, B.E. Conway, J.O'M. Bockris, E. Yeager, S.U.M. Khan, R.E. White (Eds.), Vol 7: *Kinetics and Mechanisms of Electrode Processes*, Plenum Press, New York, 1983, pp 301-398

[33] D.A. Landsman, F.J. Luczak, in: *Handbook of Fuel Cells - Fundamentals, Technology and Applications*, W. Vielstich, H.A.

Gasteiger, A. Lamm (Eds.), Vol 4: *Fuel Cell Technology and Applications*, John Wiley & Sons, Chichester, 2003, pp. 811-831

[34] J.-T. Wang, R.F. Savinell, J. Wainright, M. Litt, H. Yu, *Electrochim. Acta*, **41** (1996) 193

[35] J.-T. Wang, J.S. Wainright, R.F. Savinell, M. Litt, *J. Appl. Electrochem.*, **26** (1996) 751

[36] Q. Li, H.A. Hjuler, C. Hasiotis, J.K. Kallitsis, C.G. Kontoyannis, N.J. Bjerrum, *Electrochem. Solid-State Lett.*, **5** (2002) A125

[37] O. Savadogo, B. Xing, *J. New Mat. Electrochem. Systems*, **3** (2000) 343

[38] P. Staiti, F. Lufrano, A.S. Aricò, E. Passalacqua, V. Antonucci, *J. Membr. Sci.*, **188** (2001) 71

Chapter 6

Conclusions

More detailed conclusions are given in the papers themselves; here they given in abbreviated point form.

- Methanol dissociates directly from solution in the methanol oxidation peak prior to platinum oxide formation. Charge measurements clearly demonstrate the existence of a parallel path at low potentials and short times without formation of adsorbed CO.

- Significant differences in the nature of the strongly adsorbed species stemming from methanol, formic acid and dissolved CO were observed. This is of essential interest when designing CO-tolerant electrocatalysts for specific organic fuels.

- Regions of negative relaxation times are observed in the methanol oxidation, and these and the inductive behaviour are interpreted in terms of a nucleation-growth-collision mechanism.

- More than one kinetically significant species is required to describe the state of the surface and the kinetics in the formic acid oxidation on platinum at potentials just negative of the voltammetric peak.

- The system time constants show that oscillations do not arise from the chemical mechanism alone, but that the potential plays an essential role. Addition of an external resistor to the working electrode circuit causes current oscillations in the formic acid oxidation on platinum, implying that there is no longer true potentiostatic control at the interface.

- A 50% Pt/C catalyst with a relatively high PBI loading in the catalyst layer gives the best performing anodes and cathodes in a high-temperature hydrogen-oxygen polymer electrolyte membrane fuel cell.

- The structure of the carbon support layer plays a key role in the preparation procedure, and controlling the structure is crucial in order to obtain high-performance electrodes.

Chapter 7

Further Work

A.c. voltammetry allowed for investigation of the partially covered state of the surface, not necessarily the steady-state condition. In this thesis, we show that the methanol oxidation mechanism involves nucleation-growth-collision of islands of molecules on the electrode surface. However, quantifying the details of this model at the level of rate constants requires further theoretical and experimental work. On the theoretical side, there is no adequate theory for impedance of multistep nucleation-growth-collision mechanisms. Experimental studies using the rotating disk electrode, rotating ring-disk electrode and hydrodynamic impedance measurements could be used to quantify the mass-transport parameters and help to clarify the importance of the production of soluble species from a parallel path.

The present work studies only platinum electrodes, but it could be extended further to include alloys of platinum and ruthenium and eventually Pt/Ru catalyst particles supported on carbon, as this is the real catalyst in direct methanol fuel cells. Fundamental study of the electrode processes under true fuel cell operating conditions would give first hand information about the kinetics and mechanisms in real fuel cells and aid in the design of potential catalyst compositions.

A feasibility study of direct organic polybenzimidazole based fuel cells for temperatures up to 200 °C is highly desirable.

A major concern with PBI based fuel cells is the long-term stability. Due to the harsh environment in phosphoric acid fuel cells, only a few materials can withstand these conditions over the time period needed. Carbon nanofibres as catalyst supports, covered with catalyst particles, have shown promising results concerning the long-term stability, and need further development in order to enhance the electrocatalytic activity.

Current PBI fuel cell tests were all performed using bipolar plates designed for low-temperature Nafion® fuel cells. PBI fuel cells operating up to 200 ºC should significantly reduce the mass transport problems occurring in low-temperature PEM fuel cells. This should allow for the use different bipolar plate

designs with a larger shoulder width in order to reduce the contact resistance, and possibly with a higher number of parallel channels, which would result in a more even distribution of the local current densities, provided proper manifolding can be obtained.